



# Journal of Electromagnetic Analysis and Applications

ISSN: 1942-0730

Volume 2, Number 8, August 2010

[www.scirp.org/journal/jemaa](http://www.scirp.org/journal/jemaa)



Scientific  
Research

ISSN: 1942-0730



# JOURNAL EDITORIAL BOARD

ISSN: 1942-0730 (Print) 1942-0749 (Online)

<http://www.scirp.org/journal/jemaa>

---

## Editors-in-Chief

**Prof. James L. Drewniak** Missouri-Rolla University, USA  
**Prof. Yuanzhang Sun** Wuhan University, China

## Editorial Advisory Board

**Prof. Qingquan Chen** University of Hong Kong, China  
**Prof. Ryuichi Yokoyama** Waseda University, Japan  
**Prof. Xiaoxin Zhou** Chinese Society of Electrical Engineering (CSEE), China

## Editorial Board

**Dr. Michail B. Belonenko** Volgograd Institute of Business, Russia  
**Dr. Boguslaw Butrylo** Bialystok Technical University, Poland  
**Dr. Yuchun Guo** Xidian University, China  
**Dr. Xijiang Han** Harbin Institute of Technology, China  
**Dr. Eisuke Hanada** Shimane University Hospital, Japan  
**Dr. Isabel Jesus** Institute of Engineering of Porto, Portugal  
**Dr. Ozlem Ozgun** Middle East Technical University, Turkey  
**Dr. Mazen A. E. Salam** Assiut University, Egypt  
**Dr. Yinbiao Shu** State Grid Corporation, China  
**Prof. Yonghua Song** Tsinghua University, China  
**Prof. Francisco Torrens** Universitat of Valencia, Spain  
**Prof. Ben Young** University of Hong Kong, China  
**Dr. Wenhua Yu** Pennsylvania State University, USA  
**Dr. Jun Zou** Zhejiang University, China

---

## Editorial Assistant

**Anny Yue** Scientific Research Publishing, USA. Email: [jemaa@scirp.org](mailto:jemaa@scirp.org)

## Guest Reviewer

**Xiren Wang**

## TABLE OF CONTENTS

Volume 2 Number 8

August 2010

### A New Formulation of Electrodynamics

A. I. Arbab, F. A. Yassein.....457

### A Preliminary Ray Tracing Approach to Computational Electromagnetics for

#### Reverberation Chambers

F. Nauwelaerts, D. V. Troyen, G. A. E. Vandenbosch.....462

### Voltage Control in Smart Grids: An Approach Based on Sensitivity Theory

M. Brenna, E. D. Berardinis, F. Foiadelli, G. Sapienza, D. Zaninelli.....467

### Impact of Wind Farms of DFIG Type on Power System Transient Stability

L. B. Shi, S. Q. Dai, L. Z. Yao, Y. X. Ni, M. Bazargan.....475

### Induction of Oxidative Stress in Male Rats Subchronically Exposed to Electromagnetic Fields at

#### Non-Thermal Intensities

A. Achudume, B. Onibere, F. Aina, P. Tchokossa.....482

### Focal Region Field of a Two Dimensional Gregorian System Coated with Isotropic Chiral Medium

T. Rahim, J. Mughal, M. Hussnain.....488

### New Consideration of Problems of Gravitational Optics and Dark Matter Based on

#### Crystal Model of Vacuum

E. V. Chensky.....495

# **Journal of Electromagnetic Analysis and Applications (JEMAA)**

## **Journal Information**

### **SUBSCRIPTIONS**

The *Journal of Electromagnetic Analysis and Applications* (Online at Scientific Research Publishing, [www.SciRP.org](http://www.SciRP.org)) is published monthly by Scientific Research Publishing, Inc., USA.

#### **Subscription rates:**

Print: \$50 per issue.

To subscribe, please contact Journals Subscriptions Department, E-mail: [sub@scirp.org](mailto:sub@scirp.org)

### **SERVICES**

#### **Advertisements**

Advertisement Sales Department, E-mail: [service@scirp.org](mailto:service@scirp.org)

#### **Reprints (minimum quantity 100 copies)**

Reprints Co-ordinator, Scientific Research Publishing, Inc., USA.

E-mail: [sub@scirp.org](mailto:sub@scirp.org)

### **COPYRIGHT**

Copyright©2010 Scientific Research Publishing, Inc.

All Rights Reserved. No part of this publication may be reproduced, stored in a retrieval system, or transmitted, in any form or by any means, electronic, mechanical, photocopying, recording, scanning or otherwise, except as described below, without the permission in writing of the Publisher.

Copying of articles is not permitted except for personal and internal use, to the extent permitted by national copyright law, or under the terms of a license issued by the national Reproduction Rights Organization.

Requests for permission for other kinds of copying, such as copying for general distribution, for advertising or promotional purposes, for creating new collective works or for resale, and other enquiries should be addressed to the Publisher.

Statements and opinions expressed in the articles and communications are those of the individual contributors and not the statements and opinion of Scientific Research Publishing, Inc. We assume no responsibility or liability for any damage or injury to persons or property arising out of the use of any materials, instructions, methods or ideas contained herein. We expressly disclaim any implied warranties of merchantability or fitness for a particular purpose. If expert assistance is required, the services of a competent professional person should be sought.

### **PRODUCTION INFORMATION**

For manuscripts that have been accepted for publication, please contact:

E-mail: [jemaa@scirp.org](mailto:jemaa@scirp.org)

# A New Formulation of Electrodynamics

Arbab I. Arbab<sup>1</sup>, Faisal A. Yassein<sup>2</sup>

<sup>1</sup>Department of Physics, Faculty of Science, University of Khartoum, Khartoum, Sudan; <sup>2</sup>Department of Physics, Faculty of Science, Alneelain University, Khartoum, Sudan.

Email: {arbab.ibrahim, f.a.yassein}@gmail.com, aiarbab@uofk.edu

Received December 27<sup>th</sup>, 2009; revised July 22<sup>nd</sup>, 2010; accepted July 30<sup>th</sup>, 2010

## ABSTRACT

A new formulation of electromagnetism based on linear differential commutator brackets is developed. Maxwell equations are derived, using these commutator brackets, from the vector potential  $\vec{A}$ , the scalar potential  $\phi$  and the Lorentz gauge connecting them. With the same formalism, the continuity equation is written in terms of these new differential commutator brackets.

**Keywords:** Mathematical Formulation, Maxwell's Equations

## 1. Introduction

Maxwell equations are first order differential equations in space and time. They are compatible with Lorentz transformation which guarantees its applicability to any inertial frame. A symmetric space-time formulation of any theory will generally guarantee the universality of the theory. With this motivation, we adopt a differential commutator bracket involving first order space and time derivative operators to formulate the Maxwell equations and quantum mechanics. This is in addition to our recent quaternionic formulation of physical laws, where we have shown that many physical equations are found to emerge from a unified view of physical variables [1]. In such a formulation, we have found that Maxwell equations emerge from a single equation. Maxwell equations were originally written in terms of quaternions. They were initially written in twenty equations [a]. However, later on Maxwell equations are then written in terms of vector in the way that we are familiar today. In our present formulation, Maxwell equations are described by a set of two wave equations representing the evolution of the electric and magnetic fields. This is instead of having four equations. We aim in this paper to write down (derive) the physical equations by vanishing differential commutator brackets. We know that second order partial derivatives commute for space-space variables. We don't assume here this property is a priori for space and time. To guarantee this, we eliminate the time derivative of a quantity that is acted by a space ( $\nabla$ ) derivative followed by a time derivative, and vice-versa. In expanding the differential commutator bracket, we don't commute time and space derivative, but rather eliminate the time de-

riivative by the space derivative, and vice versa. This differential commutator bracket may enlighten us to quantize these physical quantities. By employing the differential commutator brackets of the vector  $\vec{A}$  and scalar potential  $\phi$ , we have derived Maxwell equations without invoking any a priori physical law. Maxwell arrives at his theory of electromagnetism by combing the Gauss, Faraday and Ampere laws. For mathematical consistency, he modified Ampere's law. He then came with the known Maxwell equations.

## 2. Relativistic Prelude

From Lorentz transformations one obtain,

$$x' = \gamma(x - vt), \quad y' = y, \quad z' = z, \quad t' = \gamma\left(t - \frac{v}{c^2}x\right). \quad (1)$$

We see that the commutator bracket

$$[\Delta t, \Delta x] = [\Delta t', \Delta x'] \quad (2)$$

where we have taken into account in the order of multiplication of the space and time differences,  $(\Delta x, \Delta t)$ . This shows that the commutator is Lorentz invariant. This is a new invariant quantity in relativity. We, however, already knew that the square interval is Lorentz invariant, i.e.,  $(\Delta S)^2 = (\Delta S')^2$  [2]. It follows from Equation (1) that the differential commutator bracket  $\left[\frac{\partial}{\partial t}, \vec{\nabla}\right] = 0$  is Lorentz invariant too, i.e.,  $\left[\frac{\partial}{\partial t'}, \vec{\nabla}'\right] = \left[\frac{\partial}{\partial t}, \vec{\nabla}\right]$ . We know that the spatial second order derivatives of a function,  $f = f(x, y)$ , is commutative, i.e.,

$\frac{\partial^2 f}{\partial x \partial y} = \frac{\partial^2 f}{\partial y \partial x}$ . We wonder if the commutations of space and time derivatives are equally valid for all physical quantities. Motivated by this hypothesis, we propose the following differential commutator brackets to formulate the physical laws. In particular, we apply these differential commutator brackets, in this work to derive the continuity equation, Maxwell equations.

### 3. Differential Commutators Algebra

Define the three linear differential commutator brackets as follows:

$$\left[ \frac{\partial}{\partial t}, \bar{\nabla} \right] = 0, \quad \left[ \frac{\partial}{\partial t}, \bar{\nabla} \cdot \right] = 0, \quad \left[ \frac{\partial}{\partial t}, \bar{\nabla} \times \right] = 0. \quad (3)$$

Equation (3) is correct, since partial derivatives commute, *i.e.*,  $\frac{\partial^2}{\partial t \partial x} \varphi = \frac{\partial^2}{\partial x \partial t} \varphi$ . For a scalar  $\psi$  and a vector  $\bar{G}$ , one defines the three brackets as follows:<sup>1</sup>

$$\left[ \frac{\partial}{\partial t}, \bar{\nabla} \right] \psi = \frac{\partial}{\partial t} (\bar{\nabla} \psi) - \bar{\nabla} \left( \frac{\partial \psi}{\partial t} \right), \quad (4)$$

$$\left[ \frac{\partial}{\partial t}, \bar{\nabla} \cdot \right] \bar{G} = \frac{\partial}{\partial t} (\bar{\nabla} \cdot \bar{G}) - \bar{\nabla} \cdot \left( \frac{\partial \bar{G}}{\partial t} \right), \quad (5)$$

and

$$\left[ \frac{\partial}{\partial t}, \bar{\nabla} \times \right] \bar{G} = \frac{\partial}{\partial t} (\bar{\nabla} \times \bar{G}) - \bar{\nabla} \times \left( \frac{\partial \bar{G}}{\partial t} \right). \quad (6)$$

It follows that

$$\left[ \frac{\partial}{\partial t}, \bar{\nabla} \cdot \right] (\psi \bar{G}) = \psi \left\{ \left[ \frac{\partial}{\partial t}, \bar{\nabla} \cdot \right] \bar{G} \right\} + \left\{ \left[ \frac{\partial}{\partial t}, \bar{\nabla} \right] \psi \right\} \cdot \bar{G}, \quad (7)$$

$$\left[ \frac{\partial}{\partial t}, \bar{\nabla} \times \right] (\psi \bar{G}) = \psi \left\{ \left[ \frac{\partial}{\partial t}, \bar{\nabla} \times \right] \bar{G} \right\} + \left\{ \left[ \frac{\partial}{\partial t}, \bar{\nabla} \right] \psi \right\} \times \bar{G}, \quad (8)$$

$$\left[ \frac{\partial}{\partial t}, \bar{\nabla} \cdot \right] (\bar{G} \times \bar{F}) = \bar{F} \cdot \left\{ \left[ \frac{\partial}{\partial t}, \bar{\nabla} \times \right] \bar{G} \right\} - \bar{G} \cdot \left\{ \left[ \frac{\partial}{\partial t}, \bar{\nabla} \times \right] \bar{F} \right\}, \quad (9)$$

for any vector  $\bar{F}$ . The differential commutator brackets above satisfy the distribution rule

$$\left[ \hat{A} \hat{B}, \hat{C} \right] = \hat{A} \left[ \hat{B}, \hat{C} \right] + \left[ \hat{A}, \hat{C} \right] \hat{B}, \quad (10)$$

where  $\hat{A}, \hat{B}, \hat{C}$  are  $\bar{\nabla}, \frac{\partial}{\partial t}$ . It is evident that the differential commutator brackets identities follow the same ordinary vector identities. We call the three differential commutator brackets in Equation (3) the grad-commutator bracket,

the dot-commutator bracket and the cross-commutator bracket respectively. The prime idea here is to replace the time derivative of a quantity by the space derivative  $\bar{\nabla}$  of another quantity, and vice-versa, so that the time derivative of a quantity is followed by a time derivative with which it commutes. We assume here that space and time derivatives don't commute. With this minimal assumption, we have shown here that all physical laws are determined by vanishing differential commutator bracket.

### 4. The Continuity Equation

Using quaternionic algebra [3], we have recently found that generalized continuity equations can be written as

$$\bar{\nabla} \cdot \bar{J} + \frac{\partial \rho}{\partial t} = 0, \quad (11)$$

$$\bar{\nabla} (\rho c^2) + \frac{\partial \bar{J}}{\partial t} = 0, \quad (12)$$

and

$$\bar{\nabla} \times \bar{J} = 0. \quad (13)$$

Now consider the dot-commutator of  $\rho \bar{J}$

$$\left[ \frac{\partial}{\partial t}, \bar{\nabla} \cdot \right] (\rho \bar{J}) = \frac{\partial}{\partial t} (\bar{\nabla} \cdot (\rho \bar{J})) - \bar{\nabla} \cdot \left( \frac{\partial (\rho \bar{J})}{\partial t} \right) = 0. \quad (14)$$

Using Equations (11)-(13), one obtains

$$\left[ \frac{\partial}{\partial t}, \bar{\nabla} \cdot \right] (\rho \bar{J}) = c^2 \rho \left( \frac{1}{c^2} \frac{\partial^2 \rho}{\partial t^2} - \nabla^2 \rho \right) + \left( \frac{1}{c^2} \frac{\partial \bar{J}}{\partial t} - \nabla^2 \bar{J} \right) \cdot \bar{J} = 0. \quad (15)$$

For arbitrary  $\rho$  and  $\bar{J}$ , Equation (15) yields the two wave equations

$$\frac{1}{c^2} \frac{\partial^2 \rho}{\partial t^2} - \nabla^2 \rho = 0, \quad (16)$$

and

$$\frac{1}{c^2} \frac{\partial \bar{J}}{\partial t} - \nabla^2 \bar{J} = 0. \quad (17)$$

Equations (16) and (17) show that the charge and current density satisfy a wave equation traveling at speed of light in vacuum. It is remarkable to know that these two equations are already obtained in [3]. Hence, the current-charge density wave equations are equivalent to

$$\left[ \frac{\partial}{\partial t}, \bar{\nabla} \cdot \right] (\rho \bar{J}) = 0. \quad (18)$$

### 5. Maxwell's Equations

Maxwell's equations are first order differential equations in space and time of the electromagnetic field, viz.,

$$\vec{\nabla} \cdot \vec{E} = \frac{\rho}{\epsilon_0}, \tag{19}$$

$$\vec{\nabla} \times \vec{B} = \mu_0 \vec{J} + \frac{1}{c^2} \frac{\partial \vec{E}}{\partial t}, \tag{20}$$

$$\vec{\nabla} \times \vec{E} = -\frac{\partial \vec{B}}{\partial t}, \tag{21}$$

$$\vec{\nabla} \cdot \vec{B} = 0. \tag{22}$$

These equations show that charge ( $\rho$ ) and current ( $\vec{J}$ ) densities are the sources of the electromagnetic field. Differentiating Equation (20) and using Equation (21), one obtains

$$\frac{1}{c^2} \frac{\partial^2 \vec{E}}{\partial t^2} - \nabla^2 \vec{E} = -\mu_0 \left( \vec{\nabla}(\rho c^2) + \frac{\partial \vec{J}}{\partial t} \right). \tag{23}$$

Similarly, differentiating Equation (21) and using Equation (20), one obtains

$$\frac{1}{c^2} \frac{\partial^2 \vec{B}}{\partial t^2} - \nabla^2 \vec{B} = \mu_0 (\vec{\nabla} \times \vec{J}). \tag{24}$$

These two equations state that the electromagnetic field propagates with speed of light in two cases:

- 1) charge and current free medium (vacuum), *i.e.*,  $\rho = 0, \vec{J} = 0$ , or
- 2) if the two equations

$$\vec{\nabla}(\rho c^2) + \frac{\partial \vec{J}}{\partial t} = 0, \tag{25}$$

and

$$(\vec{\nabla} \times \vec{J}) = 0, \tag{26}$$

besides the familiar continuity equation in Equation (11)

$$\vec{\nabla} \cdot \vec{J} + \frac{\partial \rho}{\partial t} = 0, \tag{27}$$

are satisfied. Equation (23) and (24) resemble Einstein's general relativity equation where space-times geometry is induced by the distribution of matter present. We see here that the electromagnetic field is produced by any charge and current densities distribution (in space and time). Now define the electromagnetic vector  $\vec{F}$  as

$$\vec{F} = \vec{B} - \frac{i}{c} \vec{E} \tag{28}$$

Adding Equation (25) and Equation (26) according to Equation (28), one obtains

$$\begin{aligned} & \frac{1}{c^2} \frac{\partial^2}{\partial t^2} (\vec{B} - \frac{i}{c} \vec{E}) - \nabla^2 (\vec{B} - \frac{i}{c} \vec{E}) \\ &= \mu_0 \left[ \frac{i}{c} \left( \vec{\nabla}(\rho c^2) + \frac{\partial \vec{J}}{\partial t} \right) + \vec{\nabla} \times \vec{J} \right]. \end{aligned} \tag{29}$$

Applying Equations(25), (26) (see [3]) in Equation (29) yields

$$\frac{1}{c^2} \frac{\partial^2 \vec{F}}{\partial t^2} - \nabla^2 \vec{F} = 0, \tag{30}$$

This is a wave equation propagating with speed of light in vacuum ( $c$ ). Hence, Maxwell wave equations can be written as a pure single wave equation of an electromagnetic sourceless complex vector field  $\vec{F}$ . We call Equations (25)-(27) the generalized continuity equations. We have recently obtained these generalized continuity equations by adopting quaternionic formalism for fluid mechanics [3]. It is challenging to check whether any real fluid satisfies these equations or not. We have recently shown that Schrodinger, Dirac and Klein-Gordon and diffusion equations are compatible with these generalized continuity equations [3]. Using Equations (19) and (20), the electric field dot-commutator bracket yields

$$\left[ \frac{\partial}{\partial t}, \vec{\nabla} \cdot \right] \vec{E} = \frac{\partial}{\partial t} (\vec{\nabla} \cdot \vec{E}) - \vec{\nabla} \cdot \left( \frac{\partial \vec{E}}{\partial t} \right) = \frac{\partial \rho}{\partial t} + \vec{\nabla} \cdot \vec{J} = 0. \tag{31}$$

This is the familiar continuity equation. Hence, the continuity equation in the commutator bracket form can be written as

$$\left[ \frac{\partial}{\partial t}, \vec{\nabla} \cdot \right] \vec{E} = 0. \tag{32}$$

Similar, using Equations (21) and (22), the magnetic field dot-commutator bracket yields

$$\left[ \frac{\partial}{\partial t}, \vec{\nabla} \cdot \right] \vec{B} = \frac{\partial}{\partial t} (\vec{\nabla} \cdot \vec{B}) - \vec{\nabla} \cdot \left( \frac{\partial \vec{B}}{\partial t} \right) = 0. \tag{33}$$

The electric field cross-commutator bracket gives

$$\left[ \frac{\partial}{\partial t}, \vec{\nabla} \times \right] \vec{E} = \frac{\partial}{\partial t} (\vec{\nabla} \times \vec{E}) - \vec{\nabla} \times \left( \frac{\partial \vec{E}}{\partial t} \right) = 0. \tag{34}$$

Using Equations (20) and (21), this yields

$$\left[ \frac{\partial}{\partial t}, \vec{\nabla} \times \right] \vec{E} = \frac{1}{c^2} \frac{\partial^2 \vec{B}}{\partial t^2} - \nabla^2 \vec{B} - \mu_0 (\vec{\nabla} \times \vec{J}) = 0. \tag{35}$$

This equation is nothing but Equation (24) above. Similarly, the magnetic field cross-commutator bracket gives

$$\left[ \frac{\partial}{\partial t}, \vec{\nabla} \times \right] \vec{B} = \frac{\partial}{\partial t} (\vec{\nabla} \times \vec{B}) - \vec{\nabla} \times \left( \frac{\partial \vec{B}}{\partial t} \right) = 0. \tag{36}$$

Using Equations (20) and (21) this yields,

$$\left[ \frac{\partial}{\partial t}, \bar{\nabla} \times \right] \bar{B} = \frac{1}{c^2} \frac{\partial^2 \bar{E}}{\partial t^2} - \nabla^2 \bar{E} + \mu_0 \left( \bar{\nabla}(\rho c^2) + \frac{\partial \bar{J}}{\partial t} \right) = 0. \quad (37)$$

This equation is nothing but Equation (23) above. Hence, Equations (35) and (37), *i.e.*,

$$\left[ \frac{\partial}{\partial t}, \bar{\nabla} \times \right] \bar{E} = 0, \quad \left[ \frac{\partial}{\partial t}, \bar{\nabla} \times \right] \bar{B} = 0. \quad (38)$$

represent the combined Maxwell equations. In terms of the vector  $\bar{F}$  defined in Equation (33), the wave equation in Equation (35) can be written as

$$\left[ \frac{\partial}{\partial t}, \bar{\nabla} \times \right] \bar{F} = 0, \quad (39)$$

which is also evident from Equation (28).

## 6. Derivation of Maxwell Equations from the Vector and Scalar Potentials, $\bar{A}$ , $\varphi$

The electric and magnetic fields are defined by the vector  $\bar{A}$  and the scalar potential  $\varphi$  as follows

$$\bar{E} = -\bar{\nabla} \varphi - \frac{\partial \bar{A}}{\partial t}, \quad \bar{B} = \bar{\nabla} \times \bar{A}. \quad (40)$$

These are related by the Lorentz gauge as

$$\bar{\nabla} \cdot \bar{A} + \frac{1}{c^2} \frac{\partial \varphi}{\partial t} = 0. \quad (41)$$

Comparing this equation with Equation (11) reveals that the continuity equation is nothing but a gauge condition. This means that a new current density  $\bar{J}'$  can be found so that the equation is still intact. We have recently explored such a possibility which showed that it is true [3]. With this motivation the physicality of the gauge  $\bar{A}$  exhibited by Aharonov–Bohm effect is tantamount to that of the current density  $\bar{J}$  [5]. The grad-commutator bracket of the scalar potential  $\varphi$

$$\left[ \frac{\partial}{\partial t}, \bar{\nabla} \right] \varphi = \frac{\partial}{\partial t} (\bar{\nabla} \varphi) - \bar{\nabla} \left( \frac{\partial \varphi}{\partial t} \right) = 0. \quad (42)$$

Using Equations (40) and (41), one obtains

$$\left[ \frac{\partial}{\partial t}, \bar{\nabla} \right] \varphi = \frac{1}{c^2} \frac{\partial^2 \bar{A}}{\partial t^2} - \nabla^2 \bar{A} - \mu_0 \bar{J} = 0. \quad (43)$$

This yields the wave equation of the vector field  $\bar{A}$  as

$$\frac{1}{c^2} \frac{\partial^2 \bar{A}}{\partial t^2} - \nabla^2 \bar{A} = \mu_0 \bar{J}. \quad (44)$$

Similarly, the dot-commutator bracket of the vector  $\bar{A}$

$$\left[ \frac{\partial}{\partial t}, \bar{\nabla} \cdot \right] \bar{A} = \frac{\partial}{\partial t} (\bar{\nabla} \cdot \bar{A}) - \bar{\nabla} \cdot \left( \frac{\partial \bar{A}}{\partial t} \right) = 0. \quad (45)$$

Using Equations (40) and (41), one obtains

$$\left[ \frac{\partial}{\partial t}, \bar{\nabla} \cdot \right] \bar{A} = \frac{1}{c^2} \frac{\partial^2 \varphi}{\partial t^2} - \nabla^2 \varphi - \frac{\rho}{\epsilon_0} = 0. \quad (46)$$

This yields the wave equation of  $\varphi$

$$\frac{1}{c^2} \frac{\partial^2 \varphi}{\partial t^2} - \nabla^2 \varphi = \frac{\rho}{\epsilon_0}. \quad (47)$$

The cross-commutator bracket of the scalar potential  $\varphi$

$$\left[ \frac{\partial}{\partial t}, \bar{\nabla} \times \right] \bar{A} = \frac{\partial}{\partial t} (\bar{\nabla} \times \bar{A}) - \bar{\nabla} \times \left( \frac{\partial \bar{A}}{\partial t} \right) = 0. \quad (48)$$

Using Equation (40), one finds

$$\left[ \frac{\partial}{\partial t}, \bar{\nabla} \times \right] \bar{A} = \frac{\partial \bar{B}}{\partial t} + \bar{\nabla} \times \bar{E} = 0. \quad (49)$$

This yields the Faraday's equation,

$$\bar{\nabla} \times \bar{E} = -\frac{\partial \bar{B}}{\partial t}. \quad (50)$$

It is interesting to arrive at this result by using the definition in Equation (40) only. Now consider the dot-commutator bracket of  $\varphi \bar{A}$

$$\left[ \frac{\partial}{\partial t}, \bar{\nabla} \cdot \right] (\varphi \bar{A}) = \frac{\partial}{\partial t} (\bar{\nabla} \cdot (\varphi \bar{A})) - \bar{\nabla} \cdot \left( \frac{\partial}{\partial t} (\varphi \bar{A}) \right) = 0. \quad (51)$$

Using Equations (40), (41) and the vector identities

$$\begin{aligned} \bar{\nabla} \cdot (\varphi \bar{G}) &= (\bar{\nabla} \varphi) \cdot \bar{G} + \varphi (\bar{\nabla} \cdot \bar{G}), \\ \bar{\nabla} \times (\bar{\nabla} \times \bar{G}) &= \bar{\nabla} (\bar{\nabla} \cdot \bar{G}) - \nabla^2 \bar{G}, \end{aligned} \quad (52)$$

Equation (51) yields

$$\varphi \left( \bar{\nabla} \cdot \bar{E} - \frac{\rho}{\epsilon_0} \right) - c^2 \left( \bar{\nabla} \times \bar{B} - \frac{1}{c^2} \frac{\partial \bar{E}}{\partial t} - \mu_0 \bar{J} \right) \cdot \bar{A} = 0. \quad (53)$$

For arbitrary  $\varphi$  and  $\bar{A}$ , Equation (53) yields the two equations

$$\bar{\nabla} \cdot \bar{E} = \frac{\rho}{\epsilon_0}, \quad (54)$$

and

$$\bar{\nabla} \times \bar{B} = \mu_0 \bar{J} + \frac{1}{c^2} \frac{\partial \bar{E}}{\partial t}. \quad (55)$$

Equations (54) and (55) are the Gauss and Ampere equations.

Similarly, the cross-commutator bracket of  $\varphi \bar{A}$

$$\left[ \frac{\partial}{\partial t}, \bar{\nabla} \times \right] (\varphi \bar{A}) = \frac{\partial}{\partial t} (\bar{\nabla} \times (\varphi \bar{A})) - \bar{\nabla} \times \left( \frac{\partial}{\partial t} (\varphi \bar{A}) \right) = 0. \quad (56)$$

Using Equations (40), (41) and the vector identity

$$\vec{\nabla} \times (\varphi \vec{G}) = (\vec{\nabla} \varphi) \times \vec{G} + \varphi (\vec{\nabla} \times \vec{G}), \quad (57)$$

Equation (56) yields

$$\varphi \left( \vec{\nabla} \times \vec{E} + \frac{\partial \vec{B}}{\partial t} \right) - c^2 \left( \vec{\nabla} \times \vec{B} - \frac{1}{c^2} \frac{\partial \vec{E}}{\partial t} - \mu_0 \vec{J} \right) \times \vec{A} = 0. \quad (58)$$

For arbitrary  $\varphi$  and  $\vec{A}$ , Equation (58) yields the two equations

$$\vec{\nabla} \times \vec{E} = -\frac{\partial \vec{B}}{\partial t}, \quad (59)$$

and

$$\vec{\nabla} \times \vec{B} = \mu_0 \vec{J} + \frac{1}{c^2} \frac{\partial \vec{E}}{\partial t}. \quad (60)$$

Once again, Equations (59) and (60) are the Faraday and Ampere equations, respectively. Hence, the four Maxwell equations are completed. To sum up, Maxwell equations are the commutator brackets

$$\left[ \frac{\partial}{\partial t}, \vec{\nabla} \cdot \right] (\varphi \vec{A}) = 0, \quad \left[ \frac{\partial}{\partial t}, \vec{\nabla} \times \right] (\varphi \vec{A}) = 0. \quad (61)$$

### 7. Energy Conservation Equation

In electromagnetism, the energy conservation equation for electromagnetic field is written as

$$\frac{\partial u}{\partial t} + \vec{\nabla} \cdot \vec{S} = -\vec{J} \cdot \vec{E}, \quad (62)$$

where

$$u = \frac{1}{2} \epsilon_0 E^2 + \frac{1}{2\mu_0} B^2, \quad \vec{S} = \frac{\vec{E} \times \vec{B}}{\mu_0}. \quad (63)$$

The energy conservation equation of the electromagnetic field can be easily obtain using the following vector identity

$$\vec{\nabla} \cdot (\vec{F} \times \vec{G}) = \vec{G} \cdot (\vec{\nabla} \times \vec{F}) - \vec{F} \cdot (\vec{\nabla} \times \vec{G}). \quad (64)$$

Let now  $\vec{E} = \vec{F}$ ,  $\vec{G} = \vec{B}$ , so that Equation (64) becomes

$$\vec{\nabla} \cdot (\vec{E} \times \vec{B}) = \vec{B} \cdot (\vec{\nabla} \times \vec{E}) - \vec{E} \cdot (\vec{\nabla} \times \vec{B}). \quad (65)$$

Employing Equations (20), (21) and (63), Eq.(65) yields

$$\frac{\partial u}{\partial t} + \vec{\nabla} \cdot \vec{S} = -\vec{J} \cdot \vec{E}, \quad (66)$$

which is the familiar energy conservation equation of the electromagnetic field [5].

### 8. Concluding Remarks

By introducing three vanishing linear differential commutator brackets for scalar and vector fields,  $\varphi$  and  $\vec{A}$  and the Lorentz gauge connecting them, we have derived the Maxwell's equations and the continuity equation without resort to any other physical equation. Using different vector identities, we have found that no any independent equation can be generated from the three differential commutators brackets.

### 9. Acknowledgements

Equations (14) and (15) are in the form of coupled wave equations known as inhomogeneous Helmholtz equations. We see that the current density J enters into these equations in a relatively complicated way, and for this reason these equations and are not readily soluble in general. This work is supported by the university of Khartoum research fund. We are grateful for this support.

### REFERENCES

- [1] A. I. Arbab and Z. Satti, "On the Generalized Maxwell Equations and Their Prediction of ElectroscalarWave," *Progress in Physics*, Vol. 2, 2009, pp. 8-13.
- [2] W. Rindler, "Introduction to Special Relativity," Oxford University Press, USA, 1991.
- [3] A. I. Arbab and H. M. Widatallah, "The Generalized Continuity Equations". <http://arxiv.org/abs/1003.0071>
- [4] J. D. Jackson, "Classical Electrodynamics," 2nd Edition, Wiley, New York, 1975.
- [5] Y. Aharonov and D. Bohm, "Significance of Electromagnetic Potentials in Quantum Theory," *Physical Review*, Vol. 115, No. 3, 1959, pp. 485-491.

### Appendix

$$\left[ \frac{\partial}{\partial t}, \vec{\nabla} \times \right] (\vec{F} \times \vec{G}) = \vec{F} \times \left( \frac{\partial}{\partial t} (\vec{\nabla} \times \vec{G}) - \vec{\nabla} \times \frac{\partial \vec{G}}{\partial t} \right) + \left( \vec{\nabla} \times \frac{\partial \vec{F}}{\partial t} - \frac{\partial}{\partial t} (\vec{\nabla} \times \vec{F}) \right) \times \vec{G} \quad (A1)$$

$$\left[ \frac{\partial}{\partial t}, \vec{\nabla} \cdot \right] (\vec{F} \cdot \vec{G}) = \vec{F} \cdot \left( \frac{\partial}{\partial t} (\vec{\nabla} \cdot \vec{G}) - \vec{\nabla} \cdot \frac{\partial \vec{G}}{\partial t} \right) + \left( \vec{\nabla} \cdot \frac{\partial \vec{F}}{\partial t} - \frac{\partial}{\partial t} (\vec{\nabla} \cdot \vec{F}) \right) \cdot \vec{G} \quad (A2)$$

# A Preliminary Ray Tracing Approach to Computational Electromagnetics for Reverberation Chambers

Filip Nauwelaerts<sup>1</sup>, Dirk Van Troyen<sup>2</sup>, Guy A. E. Vandenbosch<sup>3</sup>

<sup>1</sup>Laboratoria De Nayer v.z.w., J. P. De Nayerlaan, St-Katelijne Waver, Belgium; <sup>2</sup>Department E-ICT, Lessius Hogeschool/ Campus De Nayer ass. K. U. Leuven, J. P. De Nayerlaan, St-Katelijne Waver, Belgium; <sup>3</sup>Department of Electrical Engineering, K. U. Leuven, Leuven, Belgium.

Email: [f.nauwelaerts@labodenayer.be](mailto:f.nauwelaerts@labodenayer.be)

Received January 26<sup>th</sup>, 2010; revised June 2<sup>nd</sup>, 2010; accepted June 10<sup>th</sup>, 2010.

## ABSTRACT

*This paper summarizes a theoretical design analysis for the implementation of an electromagnetic modeling tool, focusing on the simulation of electromagnetic field propagation inside reverberation chambers. The simulation algorithms which have been developed rely on a ray tracing technique, adapted in such a way as to maximize compatibility with the specific requirements and parameters, as applicable for reverberation chambers. The most significant example of a typical parameter is the high rate of wave reflections inside the chambers' cavity. An implementation of the algorithms was used for simulation of several theoretically predictable cases. Study of the results of these test cases showed that some of the design decisions and algorithms used need to be reviewed in order to optimize the computational aspects of the application, such as resource management (memory, CPU time). Results of typical sample cases are reviewed in this paper as well, in order to identify possible pitfalls and objectives for future research.*

**Keywords:** *Electromagnetic Modeling, Computational Electromagnetics, Ray Tracing*

## 1. Introduction

Depending on its intended domain of application, electromagnetic immunity of an electronic device towards radiated electromagnetic fields can be demonstrated by using a reverberation chamber [1,2]. Typically, the internal chamber cavity consists of highly conductive material, which leads to a high degree of electromagnetic wave reflections. In combination with a tunable mode stirrer, standing wave patterns are created, resulting in high field strengths on a broad frequency spectrum.

Looking at radiated immunity assessments according to IEC61000-4-21, usage of a reverberation chamber is not allowed unless certain criteria are met. For example, during an immunity assessment, the device under test needs to be placed inside a rectangular virtual volume, where it is required that a field homogeneity is guaranteed within this volume, with the device put in place. This field homogeneity criterion states that the field strength amplitude, measured at the eight corner points of the virtual volume (and for each polarization respectively), lies within a specified standard deviation from

the normalized mean value of the normalized maximum values obtained at each of these eight locations, during one rotation of the mode stirrer.

This preliminary validation, referred to as a chamber loading verification, consumes a significant amount of measurement time. Results from a ray tracing simulation allow calculation of the electric field vector (amplitude and polarisation at a specified moment in time) at each of the eight corners of the virtual volume. This in turn allows prediction of the influence of a specific device on the chamber loading, without having to cope with the aforementioned time loss.

Moreover, the number of locations for which the resulting field vector is calculated by the adapted ray tracing technique does not have to be limited to the eight corner points. This number can be expanded to cover a specified volume, consisting of a large set of distinct locations. In the obtained simulation model, each of these locations will have a resulting field vector associated with it. This allows representation of the electromagnetic field distribution inside the reverberation chamber as a 3D vector field.

## 2. Conceptual Description

Initially, identification and definition of all relevant parameters is required, such as chamber dimensions, source antenna position and orientation with respect to the chamber origin, transmit antenna radiation pattern, conductivity of each enclosure and locations for which a resultant field vector is desired.

These parameters are translated into a set of equations, which allow interpretation by the adapted ray tracing algorithm. The algorithm decomposes the propagated electromagnetic wave front into a finite set of distinct rays. Based on the initial equations, the algorithm calculates how each ray propagates through the defined medium and evaluates possible reflection on obstacle surfaces.

The contribution of each individual ray to the resulting 3D vector field is quantified by implementation of appropriate equations, which allow calculation of the electric field strength amplitude, phase and its polarization for each position on an arbitrary ray at a specified distance from the source.

## 3. Basic Ray Tracing Process

Each individual straight ray path segment has a ray Equation (1) associated with it, which allows calculation of the Cartesian coordinates of an arbitrary point  $p$ , with  $p$  and  $p_0$  elements of the ray path and  $\vec{u}$  the unit direction vector.

$$p = p_0 + s \cdot \vec{u} \quad (1)$$

Secondly, it is assumed that each enclosure can be represented by a grouping of one or more rectangular surfaces. For each of these surfaces, plane Equation (2) holds for normal vector and the Cartesian coordinates of an arbitrary point  $p$  on the surface. This equation represents the plane (with infinite length and width) which the surface is part of, where  $D$  is a constant that determines part of the position of the plane.

$$\vec{N} \cdot p = -D \quad (2)$$

These equations can be used for each enclosure surface and ray, given the initial parameters according to a Cartesian coordinate system. Substitution of Equations (1) and (2) results in Equation (3), which allows evaluation of ray surface intersection.

$$\vec{N} \cdot (p_0 + s \cdot \vec{u}) = -D \quad (3)$$

Should this equation hold, then intersection occurs and variable  $s$  represents the distance between  $p_0$  and the point of intersection, quantifiable by applying Equation (4).

$$s = \frac{-D - \vec{N} \cdot p_0}{\vec{N} \cdot \vec{u}} \quad (4)$$

Finally, it is verified whether the point of intersection lies within the surfaces boundaries by an inside-outside

verification.

Depending on the intersected surface's conductivity, reflection could occur [3], which is considered to be specular. A reflected wave front is in its turn represented by a finite set of reflected rays, for which each ray equation can be calculated based on the law of specular reflection (5), with incident ray direction  $\vec{I}$  and reflected ray direction  $\vec{R}$ .

$$\vec{R} = \vec{I} - (2 \cdot \vec{I} \cdot \vec{N}) \cdot \vec{N} \quad (5)$$

This process of reflection continues iteratively for a defined finite number of reflections.

## 4. An Adapted Ray Tracing Process

### 4.1 Interference

With the basic ray tracing process, detection of interference and therefore modeling of standing wave patterns is not possible, since phase is not taken into account. This aspect is adapted by implementation of appropriate equations for electromagnetic propagation. This is elaborated into more detail further on.

### 4.2 Multiple Viewpoints

The basic algorithm focuses on representing a 3D scene on a 2D pixel screen, as observed from one single viewpoint (e.g. the human eye). The viewpoint is used as the starting point for each initial ray, thus the basic process is backtracking the trail through the 3D scene in order to determine each ray's contribution to a pixel on the 2D screen [4].

Here, a 3D vector field is desired, consisting of a set of field vectors, where each vector is the resultant of contributions from all intersecting rays at one of the specified locations of interest. For this reason it is decided to use the source antenna location as the origin of each initial ray, instead of the location of a viewpoint. This is referred to as the alternative backtracking algorithm further on.

### 4.3 Spatial Subdivision and Ray Contribution

Combination of the alternative backtracking and of the assumption of specular reflection could lead to the situation where a certain location of interest will never be reached by a ray. This is due to the fact that an initial angle step is applicable between each successive ray. This angle step inherently introduces inaccuracy with an incremental behavior, linearly proportional to the distance from the source. As a solution, each location of interest is represented as a cubic cell (**Figure 1**). This way, the area of reception of each location of interest is no longer a single coordinate in the Cartesian system, but has now been enlarged in such a way that it is represented by a cubic volume instead. The edges of each individual cube have to be smaller with respect to the applicable

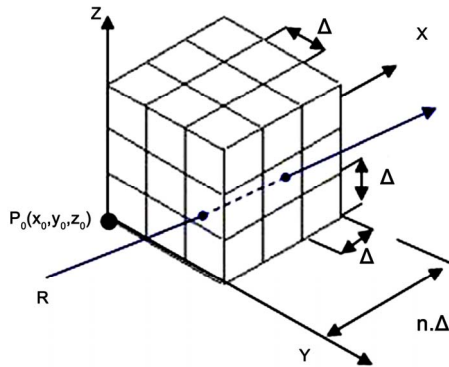


Figure 1. Spatial subdivision

wavelength, otherwise phase information would be lost by this introduced inaccuracy.

The algorithm performs detection of intersection between a ray and a cell facet, based on a set of plane equations for each group of cell facets which are part of the same plane. Identification of the exact cell facet of that group is the result of an inside or outside verification.

To minimize the risk of missing cells, it can be shown that a rule of thumb (Equation (6)) expresses the minimal angular difference  $\alpha$  in terms of the number of reflections  $n$ , the longest chamber dimension  $L$  and the cell size  $i$ .

$$\alpha = 2 \cdot \arcsin\left(\frac{i/2}{n \cdot L}\right) \quad (6)$$

As mentioned earlier, modeling at high frequencies requires small cell sizes in turn. This has as a consequence that very small angle steps have to be chosen, which leads to an increasing number of initial rays  $r$  and therefore algorithm iterations, since  $r \sim 1/\alpha^2$ . This has a negative effect on the required processing time

## 5. Quantification of Electromagnetic Propagation

### 5.1 Correlation with Antenna Radiation Pattern

Each initial ray originates at the location of the transmit antenna. A 3D antenna radiation pattern allows determination of the initial intensity of the radiated EM field through interpolation, by matching ray direction and azimuth/elevation angle of the radiation pattern. A combination of the radiation pattern of a tuned dipole with a sample initial ray is given in Figure 2.

### 5.2 Free Space Field Equations

For computational convenience, the spherical-polar coordinate system is used to set up equations for the electric field component's amplitude and phase (Figure 3) [5]. Under far field conditions, component  $\vec{E}_r$  can be neglected.

Using a half wave dipole and assuming free space pro-

pagation, Equation (7) is applied to calculate the electric field component  $|\vec{E}_\theta|$  at distance  $r$  from the transmit antenna.

$$|\vec{E}_\theta| = j \cdot \frac{Z_0 \cdot I_m}{2\pi r} \cdot e^{-j \cdot k \cdot r} \cdot \left[ \frac{\cos(k \cdot L/2 \cdot \cos \theta) - \cos(k \cdot L/2)}{\sin \theta} \right] \quad (7)$$

### 5.3 Reflection and Polarization

Each enclosure inside the cavity of the reverberation chamber acts as a discontinuity in the propagation medium. Associating each discontinuity with a reflection coefficient allows calculation of the amount field that is reflected, relative to the incident field.

Reflections will occur differently however for EM waves polarized in parallel or perpendicular to the plane of incidence, leading to two reflection coefficients:  $\Gamma_H$  and  $\Gamma_V$ . This has as a consequence that each incident wave needs decomposition into a parallel and a perpendicular component. Their contributions to the total reflected field vector is calculated separately, according to Equation (8).

$$\vec{E}_R = |\vec{E}_H| \cdot \Gamma_H \cdot \vec{h} + |\vec{E}_V| \cdot \Gamma_V \cdot \vec{v}_R \quad (8)$$

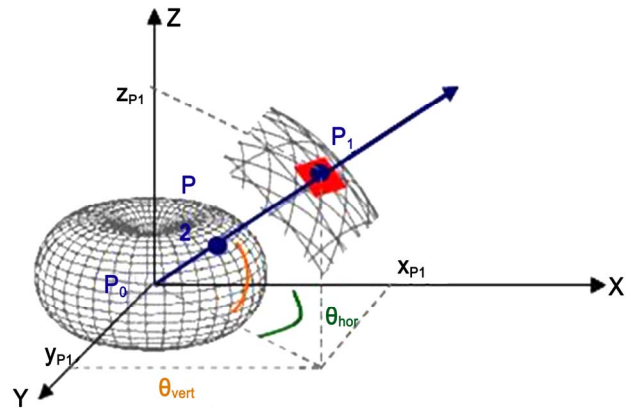


Figure 2. Antenna radiation pattern and ray generation

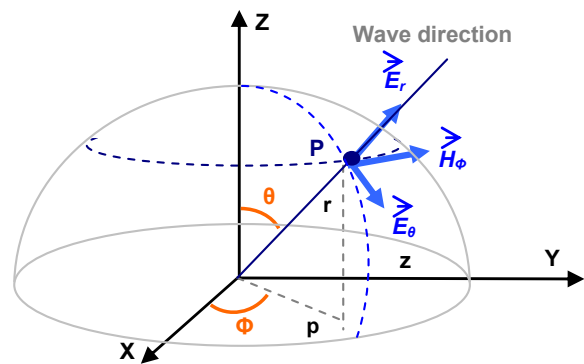


Figure 3. Spherical-polar coordinate system

$\vec{E}_H$  and  $\vec{E}_V$  represent the parallel, respectively perpendicular components of the incident electric field vector.  $\vec{v}_R$  is the resultant tangential unit vector after reflection. Equation (9) and **Figure 4** show how this new unit vector is calculated.

### 6. Validation of Typical cases

Combination of the adapted ray tracing process design with the equations for EM propagation and reflection, allows implementation of modeling algorithms. A preliminary implementation was used to model several typical cases. A limited number of examples is shown.

#### 6.1 Fundamental TE<sub>10</sub> Mode inside Rectangular Waveguide

**Figure 5** shows the resulting model after simulation of a TE<sub>10</sub> mode inside a rectangular waveguide (frequency = 1 GHz, width =  $\lambda/2$ , height  $\ll$  width, monopole at  $\lambda/4$  from reflecting front panel). While a 3D vector field is calculated, only the vertical components' magnitudes are shown for the sake of clarity.

A standing wave pattern can be distinguished along the longitudinal axis, which corresponds to the theoretically expected behavior [6]. The initial part, near the transmitting monopole, shows abrupt changes. These phenomena are considered to be caused by the far field approximations.

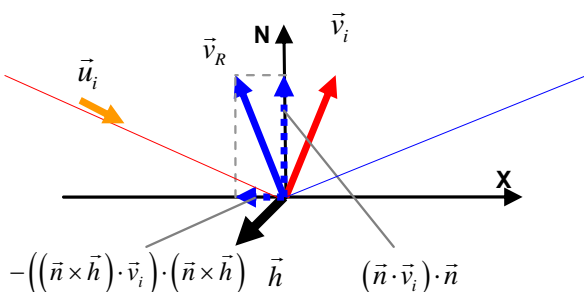


**Figure 4. Antenna radiation pattern and ray generation**

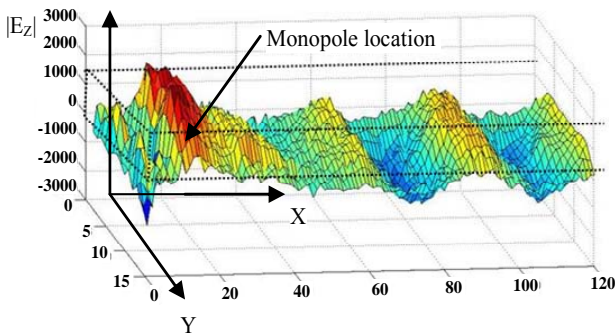


**Figure 5. TE<sub>10</sub> waveguide model**

#### 6.2 Effect of an Aperture inside a Rectangular Waveguide

**Figure 6** shows the resulting model of an identical waveguide setup, where an additional panel is inserted. This panel is provided with a narrow aperture, where the aperture is dimensioned in such a way that in theory transmission through the waveguide is blocked. The model indeed shows how the standing wave pattern is disrupted by the aperture, where a negligible amount of energy finds its way beyond the discontinuity. **Figure 7** shows a top view along the XY-plane.

#### 6.3 Field Evaluation inside Large Reverberation Chamber

The effect of chamber loading was modeled. To allow validation, a measurement was performed with a single field probe located at a specified distance from the transmit antenna (setup 1). By adding cascading absorbers on the floor surface (setup 2), the measured field strength amplitude decreased by 4.77 dB (**Figure 8**).

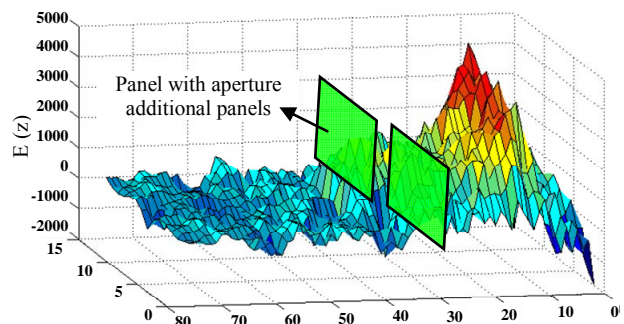


**Figure 6. Aperture inside waveguide**

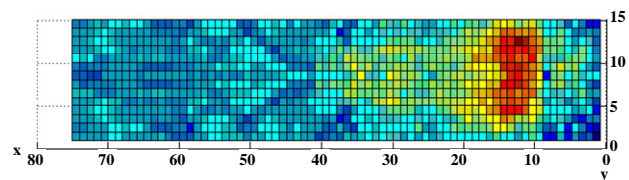


**Figure 7. Aperture inside waveguide - top view**

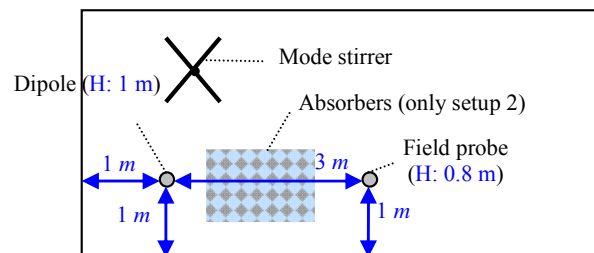


**Figure 8. Reverberation chamber (L: 9m, W: 5m, H: 4m) – setup 1 and 2**

A correct model should allow derivation of a comparable damping value of 4.77 dB. Both setups were modeled for a set of locations of interest ( $15 \times 15 \times 15 = 3375$  locations in total), taking a maximum of 10 reflections into account. The resulting vector fields of both setups are given in **Figures 9(a)** and **9(b)**, where each small, colored line represents a single field vector. Each single field vector corresponds to the resultant field vector for a specific location of interest, as calculated by the designed algorithm.

In order to allow numerical analysis of the resulting amplitudes, the values of both models are mapped on a histogram (**Figure 10**). This histogram shows how many of the calculated field vectors for each setup have an amplitude for which the absolute value lies within one of the specified intervals. Although the values for setup 1 have the tendency to be slightly higher than the values for setup 2, it can't be stated that the differences shown are in correlation with the measurements.

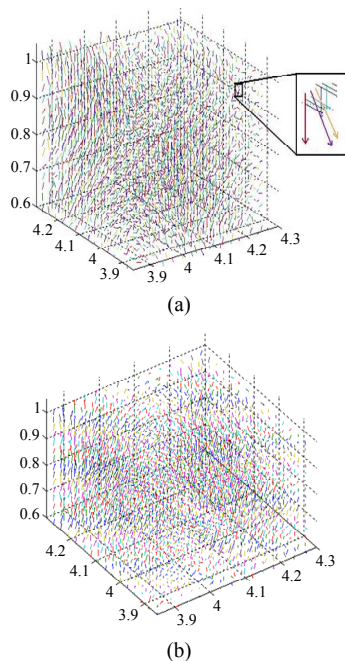


**Figure 9.** (a) 3D vector field model of  $\vec{E}$  without; (b) 3D vector field model of  $\vec{E}$  with absorbers

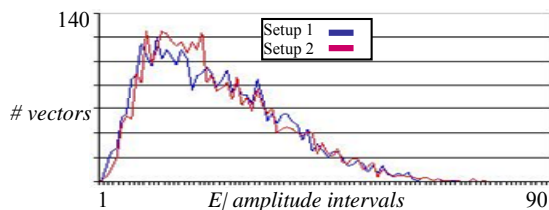


**Figure 10.** Histogram of field vector amplitudes

## 7. Conclusions and Outline for Future Research

Validation through sample cases show that the current design delivers acceptable results for smaller cavities (e.g. waveguides), but accuracy for larger environments with high reflection rates still remains insufficient (validation of the chamber loading inside a large reverberation chamber showed that a measured attenuation of 4.77 dB could not be reproduced by interpretation of simulation models).

One of the aspects in the designed algorithm which is highly related to this accuracy is the angular difference between initial rays. Equation (6) already indicated the dependencies between frequency, cell size and their effect on required processing time.

In terms of processing time, it can also be noticed that the current design often relies on goniometric functions. Replacement by matrix transformations for example would improve the resource requirements. A second improvement could be implemented by grouping the surfaces into larger sets during intersection evaluation, and to perform intersection evaluation on these sets first. This should lead to an  $O(\log n)$  search algorithm instead of the current  $O(n)$  version.

For each ray, the total number of reflections was chosen to be 10 for most aforementioned cases, where this number should be related to the remaining field power after attenuation and absorption.

The current design relies on the law of specular reflection. The diffusion is not taken into account, which also leads to less accurate models [7].

These aforementioned conclusions present the outline of further study in the context of a Ph.D. research, where a possible scenario could be the combination of different simulation techniques, such as ray tracing, FEM, BEM, FDM, FDTD, etc.

## REFERENCES

- [1] EUROCAE – “Environmental conditions and test procedures for airborne equipment,” RTCA DO-160D, RTCA, Washington, DC, 1997.
- [2] IEC 61000-4-21, IEC Central Office, Switzerland, 2000.
- [3] B. de Greve, “Reflections and Refractions in Ray Tracing,” 2007. [http://www.bramz.net/data/writings/reflection\\_transmission.pdf](http://www.bramz.net/data/writings/reflection_transmission.pdf)
- [4] D. Heam and P. Baker, Computer Graphics with OpenGL. Pearson Prentice Hall, New Jersey, 2003.
- [5] J. R. Wait, “Introduction to Antennas & Propagation,” Short Run Press Ltd, England, 1986.
- [6] A. W. Cross, “Experimental Microwaves,” Sanders, Stevenage, 1965.
- [7] C. M. Goral, K. E. Torrance, D. P. Greenberg and B. Bataille, “Modeling the Interaction of Light Between Diffuse Surfaces,” *ACM SIGGRAPH Computer Graphics*, Vol. 18, No. 3, pp. 213-222, 1984.

# Voltage Control in Smart Grids: An Approach Based on Sensitivity Theory

Morris Brenna<sup>1</sup>, Ettore De Berardinis<sup>2</sup>, Federica Foiadelli<sup>1</sup>, Gianluca Sapienza<sup>3</sup>, Dario Zaninelli<sup>1</sup>

<sup>1</sup>Politecnico di Milano – Department of Energy, Milan, Italy; <sup>2</sup>CESI S.p.A., Milan, Italy; <sup>3</sup>Politecnico di Milano – Department of Energy in Collaboration with ENEL Distribuzione S.p.A., Milan, Italy.  
Email: gianluca.sapienza@mail.polimi.it

Received March 30<sup>th</sup>, 2010; revised May 25<sup>th</sup>, 2010; accepted May 31<sup>st</sup>, 2010

## ABSTRACT

*Due to the development of Distributed Generation (DG), which is installed in Medium-Voltage Distribution Networks (MVDNs) such as generators based on renewable energy (e.g., wind energy or solar energy), voltage control is currently a very important issue. The voltage is now regulated at the MV busbars acting on the On-Load Tap Changer of the HV/MV transformer. This method does not guarantee the correct voltage value in the network nodes when the distributed generators deliver their power. In this paper an approach based on Sensitivity Theory is shown, in order to control the node voltages regulating the reactive power exchanged between the network and the dispersed generators. The automatic distributed voltage regulation is a particular topic of the Smart Grids.*

**Keywords:** Voltage Regulation, Reactive Power Injection, Distributed Generation, Smart Grids, Sensitivity Theory, Renewable Energy

## 1. Introduction

Due to the development of Distributed Generation (DG), which is installed in Medium-Voltage Distribution Networks (MVDNs) such as generators based on renewable energy (e.g., wind energy or solar energy), voltage control is currently a very important issue.

The voltage of MVDNs is now regulated acting only on the On-Load Tap Changer (OLTC) of the HV/MV transformer [1]. The OLTC control is typically based on the compound technique, and this method does not guarantee the correct voltage value in the network nodes when the generators deliver their power [2,3].

When a generator injects power in the network, the voltage tends to rise. In HV networks this phenomenon happens mainly when reactive power is injected, because the resistance is negligible if compared with the inductive reactance [4]. Instead in MVDNs the resistance is not negligible and the result is that an injection of active power also increases the voltage.

In other words the so-called  $Pq - QV$  decoupling [5], which is a typical of HV networks, is inexistent in MVDNs. The  $P$  variations are “coupled” with the voltage variations.

If no precautions are taken, in particular network conditions the overcome of the maximum admissible voltage can happen in any nodes.

When a generator injects power, the voltage rises in all network nodes, but some nodes are mainly influenced than others by the power injection. This influence can be obtained using a Sensitivity method.

In this paper an approach based on Sensitivity Theory is shown, in order to control the network voltage using the reactive power exchanged between network and the distributed generators. This approach allows to control the voltage in the long term period. Besides, fast-dynamic voltage disturbances are not taken into account [6].

After the theoretical analysis, a numerical example is shown, in order to validate the proposed theory.

The proposed method differs from the others used in HV networks analysis, based on the Jacobian Matrix [1,2-4] and its application is easy.

The topological proprieties that results from the theoretical analysis imply that the proposed sensitivity method can be easily implemented in automatic voltage control devices, in order to obtain the distributed voltage regulation.

The automatic voltage regulation in a distributed manner is a typical topic of the Smart Grids context.

The paper is structured in the following way. In Section 1, the proposed voltage control method is shown, and an overview on the voltage profiles with DG, are given. In Section 3, the proposed Sensitivity approach is

studied, referring to a MV test network, composed by four nodes. Finally, in Section 4, a numerical application is presented, in order to validate the proposed theory.

## 2. The Proposed Criteria to Control the Network Voltage with Distributed Generation

Many methods can be used to control the voltage in network nodes (network voltages). The proposed method varies the reactive power exchanged between the generators and the network while maintaining the OL-TC in a fixed position for a particular load condition.

Let us suppose that the Automatic Voltage Regulator (AVR) that controls the OLTC maintains the MV bus-bar voltage at the rated value (1 p.u.), assuming that the transformer taps are adequate.

For passive grids, when no generators are connected to the MVDN, the voltage profile (VP; *i.e.*, the voltage values along a line) decreases monotonically (see profile a in **Figure 1**) due to the load absorptions. When the generators are connected and inject power into the MVDN, the nodal voltages increase and the VP is no longer monotonic, as shown in profile b in **Figure 1** (profile b). This phenomenon also occurs if generators work at unitary power factor (*i.e.*, only active power is injected due to the non-negligible network resistance) [7].

It is important to note that, in steady-state, the condition maintained at the MV busbar by the AVR decouples the MV feeders, and the result is that each feeder works without the influence of the other lines. In other words, the loads and generators connected to other feeders do not influence the VP of the considered line.

Typically, the generators installed in Smart Grids are based on renewable energy; therefore, their power-time profiles are unknown. Due to the high generated power and a possibly low load condition, the voltage in some nodes can thus exceed the maximum admissible value ( $V_{max}$ ; *i.e.*, the voltage threshold [8]) defined by the standards.

Of course the voltage threshold is strictly related with the settings of the voltage relays installed in the network, *e.g.* at the generator nodes [9].

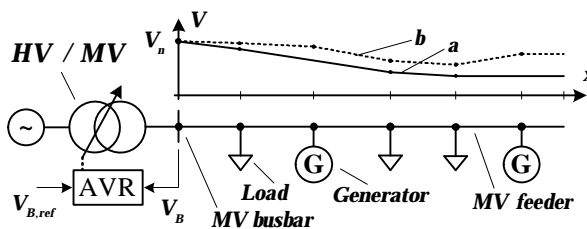


Figure 1. Voltage profiles in a MV feeder with and without Distributed Generators

If the generators are able to control the injected or absorbed reactive power, the network voltage profiles can be modified by acting on the reactive powers. It is clear that each controllable generator needs a Generator Remote Terminal Unit (GRTU) that is connected to a central control system to set the generator reactive power, (*i.e.*, to control the exciter of the synchronous generators [1] or act on the inverter control if the generator is inverter-based) [10,11]. In this work, the central control is called the Generator Control Centre (GCC). In addition, we use a hierarchical control structure [12,13].

Let us suppose that the voltage is measured only in the generator nodes by the GRTUs. This assumption does not affect the generality of the proposed method because a Measuring Remote Terminal Unit connected to the GCC can be installed in each node that must be controlled.

When the voltage in the  $i^{th}$  node exceeds  $V_{max}$ , the GRTU installed in the same node sends the signal “Voltage Threshold Overall” (VTO) to the GCC using a communication channel. The GCC then selects the generator in the  $j^{th}$  node that has the maximum influence on the voltage of the  $i^{th}$  node, the “Best Generator” (BG), and switches it to the reactive power absorption (RPA) mode. Therefore, the voltage in the  $i^{th}$  node tends to decrease.

The problem is thus to determine the best generator and ensure that the GCC chooses it. In this work, a sensitivity-based method is proposed to select the BG.

Moreover, we suppose that the generators can only be switched in the RPA mode by the GCC by a constant power factor. Therefore, if  $P_j$  is the active power injected by the generator connected to the  $j^{th}$  node, then it absorbs the reactive power  $Q_j = P_j \tan \phi_j$  (where  $\cos \phi_j$  is the minimum power factor of the generator) when it is switched during RPA. In other words, we assume that no continuous reactive power modulation is possible.

An example of the procedure described above is shown in **Figure 2**. Let us suppose that load  $L_d$  suddenly decreases its power (for example, due to a trip) and  $V_2$  exceed  $V_{max}$ .

The GRTUs of  $G_2$  send the signal VTO to the GCC that must choose the BG using the sensitivity method. Assuming that the BG is  $G_1$ , it will be switched by the

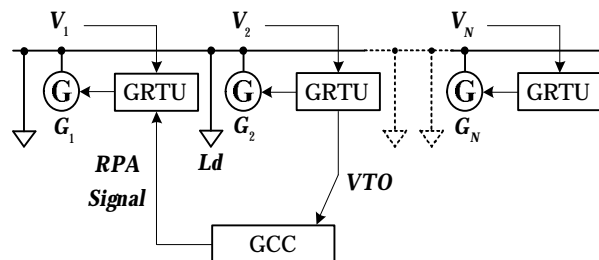


Figure 2. Voltage control using GRTU and GCC

GCC in the RPA mode; therefore, the reactive power absorbed by G1 becomes  $Q_1 = P_1 \tan \phi_1$ .

As explained in the following, the GCC must know the reactive power that each controllable generator can absorb in order to choose the BG. We suppose that this information is acquired by the GCC using a polling technique on each GRTU.

### 3. The Proposed Sensitivity Approach

#### 3.1 Classical Sensitivity Theory Overview

The classical sensitivity theory used in HV network analysis to perform primary and secondary voltage regulation [14] is based on the Jacobian Matrix and reveals the relationships between the nodal voltages (magnitude and phase) and the nodal power injections (active and reactive). The relationships mentioned above are represented by the following matrix expression [2]:

$$\begin{bmatrix} [\Delta E] \\ [\Delta J] \end{bmatrix} = \begin{bmatrix} \left[ \frac{\partial P}{\partial V} \right] & \left[ \frac{\partial P}{\partial J} \right] \\ \left[ \frac{\partial Q}{\partial V} \right] & \left[ \frac{\partial Q}{\partial J} \right] \end{bmatrix}^{-1} \begin{bmatrix} [1] & [0] \\ [0] & [1] \end{bmatrix} \begin{bmatrix} [\Delta P^*] \\ [\Delta Q^*] \end{bmatrix} \quad (1)$$

where  $[\Delta E]$  and  $[\Delta J]$  are, respectively, the nodal voltage magnitudes (rms) and phase variations corresponding to the nodal active or reactive power injections  $[\Delta P^*]$  and  $[\Delta Q^*]$  ( $[1]$  is the identity matrix).

Equation (1) can be rewritten in the following compact form:

$$\begin{bmatrix} [\Delta E] \\ [\Delta J] \end{bmatrix} = [s] \begin{bmatrix} [\Delta P^*] \\ [\Delta Q^*] \end{bmatrix} \quad (2)$$

where:

$$[s] @ \begin{bmatrix} \left[ \frac{\partial P}{\partial V} \right] & \left[ \frac{\partial P}{\partial J} \right] \\ \left[ \frac{\partial Q}{\partial V} \right] & \left[ \frac{\partial Q}{\partial J} \right] \end{bmatrix}^{-1} \begin{bmatrix} [1] & [0] \\ [0] & [1] \end{bmatrix} \quad (3)$$

is the (injection) sensitivity matrix. The method describes above is generally valid, but its computational complexity is too high for practical voltage analysis in MVDNs. For radial networks, only the voltage magnitude is needed to control the nodal voltages. The proposed theory is easier than classical theory, and it is suitable for radial MVDNs.

#### 3.2 The Proposed Theory

In this section, the proposed theory for choosing the BG is outlined. The method is first described in general and considers the possibility of reactive power regulation for all nodes.

After the general treatment, the analysis focuses on a realistic network in which the reactive power can only be controlled in some nodes (generator nodes).

Let us consider the network depicted in **Figure 3**, which is a four-node test MVDN.

The general loads  $Ld_1 \dots Ld_4$  are represented using constant PQ models. Positive  $P$  (or  $Q$ ) corresponds to the absorbed power by the load. Negative  $P$  (or  $Q$ ) corresponds to the injected power in the network (*i.e.*, the general load is really a generator). The per-phase equivalent circuit is shown in **Figure 4**.

The lines  $L_{01} \dots L_{24}$  are modeled using the RL-direct sequence equivalent circuit [15], but the shunt admittances are neglected. The node 0 represents the MV busbar, which is regulated at a constant voltage value  $E_0$  by the AVR of the OLTC. This reference voltage coincides with the rated value  $E_0 = V_n / \sqrt{3}$ .

Because the busbar is regulated at  $E_0$ , we can characterize the generic node  $i$  using the difference  $V_{oi}$  between the magnitude of the busbar voltage and the node voltage  $E_i$ . In other words, we can write:

$$V_{oi} = E_0 - E_i \quad (4)$$

In radial networks, (4) can be calculated as the sum of the voltage differences between adjacent nodes from the  $i$ th node toward the MV busbar. For example, if  $i = 3$  (see **Figure 4**), (4) becomes:

$$V_{o3} = E_0 - E_3 \quad (5)$$

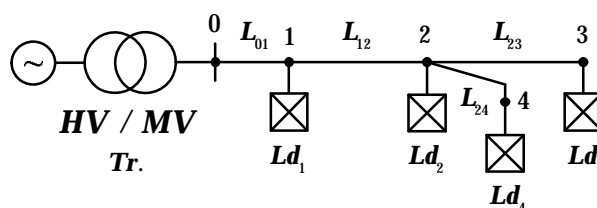


Figure 3. The considered four nodes test MVDN

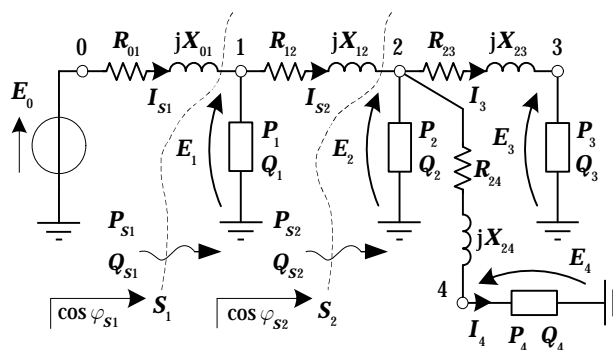


Figure 4. The per-phase equivalent circuit

By adding and subtracting  $E_1$  and  $E_2$  in (5), we obtain:

$$\begin{aligned} V_{03} &= (E_0 - E_1) + (E_1 - E_2) + (E_2 - E_3) \\ &= V_{01} + V_{12} + V_{23} \end{aligned} \quad (6)$$

where  $V_{03}$  is the sum of the voltage differences  $V_{01}$ ,  $V_{12}$  and  $V_{23}$ .

$V_{23}$  can be calculated considering the network parameters and the line power flows as follows:

$$\begin{aligned} V_{23} &= E_2 - E_3 \\ &= R_{23}I_3 \cos j_3 + X_{23}I_3 \sin j_3 \\ &= \frac{R_{23}E_3I_3 \cos j_3 + X_{23}E_3I_3 \sin j_3}{E_3} \\ &= \frac{R_{23}P_3 + X_{23}Q_3}{E_3} \end{aligned} \quad (7)$$

where  $\cos j_3$ ,  $P_3$  and  $Q_3$  are the power factor and the active and reactive (per-phase) powers of the load  $Ld_3$ , respectively.  $I_3$ ,  $R_{23}$  and  $X_{23}$  are the current, resistance and reactance of the line  $L_3$ .

Normally, the nodal voltages are close to the rated voltage  $E_n$ . Applying this assumption to (7) leads to:

$$V_{23} \cong \frac{R_{23}P_3 + X_{23}Q_3}{E_n} \quad (8)$$

Similarly, considering nodes 1 and 2, we can write:

$$\begin{aligned} V_{12} &= E_1 - E_2 \\ &= R_{12}I_2 \cos j_{s2} + X_{12}I_2 \sin j_{s2} \\ &= \frac{R_{12}E_2I_2 \cos j_{s2} + X_{12}E_2I_2 \sin j_{s2}}{E_2} \\ &\cong \frac{R_{12}P_{S2} + X_{12}Q_{S2}}{E_n} \end{aligned} \quad (9)$$

where  $P_{S2}$  and  $Q_{S2}$  are the active and reactive powers through the section  $S_2$  and  $\cos j_{s2}$  is the power factor for the same section. For  $P_{S2}$  and  $Q_{S2}$ , we can write:

$$P_{S2} = P_2 + P_3 + P_4 + P_{R23} + P_{R24} \quad (10)$$

$$Q_{S2} = Q_2 + Q_3 + Q_4 + Q_{X23} + Q_{X24} \quad (11)$$

where  $P_{R23}$  and  $P_{R24}$  are the power losses in  $R_{23}$  and  $R_{24}$ , while  $Q_{X23}$  and  $Q_{X24}$  are the reactive powers absorbed by  $X_{23}$  and  $X_{24}$ . These active and reactive losses are negligible compared to the load powers. Applying this assumption to (9), (10) and (11) leads to:

$$P_{S2} \cong P_2 + P_3 + P_4 \quad (12)$$

$$Q_{S2} \cong Q_2 + Q_3 + Q_4 \quad (13)$$

and:

$$V_{12} \cong \frac{R_{12}(P_2 + P_3 + P_4) + X_{12}(Q_2 + Q_3 + Q_4)}{E_n} \quad (14)$$

Finally, the voltage difference  $V_{01}$  is:

$$V_{01} = E_0 - E_1 \cong \frac{R_{01}P_{S1} + X_{01}Q_{S1}}{E_n} \quad (15)$$

where:

$$P_{S1} \cong P_1 + P_2 + P_3 + P_4 \quad (16)$$

$$Q_{S1} \cong Q_1 + Q_2 + Q_3 + Q_4 \quad (17)$$

are the powers through section  $S_1$ .

Using (6) with (15), (9) and (8), we can say that  $V_{03}$  is a function of all loads and active and reactive powers, *i.e.*,  $P_1 \dots P_4$  and  $Q_1 \dots Q_4$ . The same observation is valid for  $E_3$ :

$$E_3 = E_0 - V_{03} = E_0 - (V_{01} + V_{12} + V_{23}) \quad (18)$$

because  $E_0$  is constant. In other words, we can write:

$$E_3 = f(P_1, \dots, P_4, Q_1, \dots, Q_4) \quad (19)$$

Equation (19) shows that an active/reactive power variation (in the general  $j$  node) that is defined as:

$$\Delta P_j = P_j^f - P_j^0 \quad (20)$$

$$\Delta Q_j = Q_j^f - Q_j^0 \quad (21)$$

where  $P_j^f$  ( $Q_j^f$ ) and  $P_j^0$  ( $Q_j^0$ ) are the final and initial power values, respectively, produces a voltage variation in node 3 that is defined as:

$$\Delta E_3 = E_3^f - E_3^0 \quad (22)$$

In this treatment, we only consider the reactive power variations (*i.e.*,  $\Delta P_j = 0$ ) because we assume that only the reactive power can be used to control the node voltages.

The variation  $\Delta E_3$  can be calculated by linearizing (19) and considering only the reactive power variations. In particular, we can write:

$$\begin{aligned} \Delta E_3 &= \frac{\partial E_3}{\partial Q_1} \Delta Q_1 + \frac{\partial E_3}{\partial Q_2} \Delta Q_2 + \\ &+ \frac{\partial E_3}{\partial Q_3} \Delta Q_3 + \frac{\partial E_3}{\partial Q_4} \Delta Q_4 \end{aligned} \quad (23)$$

The terms  $\partial E_i / \partial Q_j$  in (23) indicate the "gain" from the voltage variation  $\Delta E_i$  in node  $i$  when a reactive power variation  $\Delta Q_j$  occurs in node  $j$ . In other words, they are sensitivity terms.

According to (18), we can obtain:

$$\begin{aligned}\frac{\partial E_3}{\partial Q_2} &= -\frac{X_{01} + X_{12}}{E_n} \\ \frac{\partial E_3}{\partial Q_3} &= -\frac{X_{01} + X_{12} + X_{23}}{E_n} \\ \frac{\partial E_3}{\partial Q_4} &= -\frac{X_{01} + X_{12}}{E_n}\end{aligned}\quad (24)$$

Substituting equation group (24) into (23) has important implications. If we have a reactive injection in any node, *i.e.*,  $\Delta Q_j < 0$  (in this case  $j=1\dots 4$ ), then  $\Delta E_3 > 0$  in node 3 (*i.e.*, the voltage increases). Then, if we were to reduce the voltage in any node, we must absorb reactive power from the network (*i.e.*,  $\Delta Q_j > 0$ ) by using, for example, the distributed generators.

If the above analysis that focuses on node 3 is extended to all network nodes, (23) has a general matrix relationship:

$$\begin{bmatrix} \Delta E_1 \\ \Delta E_2 \\ \Delta E_3 \\ \Delta E_4 \end{bmatrix} = \begin{bmatrix} \frac{\partial E_1}{\partial Q_1} & \frac{\partial E_1}{\partial Q_2} & \frac{\partial E_1}{\partial Q_3} & \frac{\partial E_1}{\partial Q_4} \\ \frac{\partial E_2}{\partial Q_1} & \frac{\partial E_2}{\partial Q_2} & \frac{\partial E_2}{\partial Q_3} & \frac{\partial E_2}{\partial Q_4} \\ \frac{\partial E_3}{\partial Q_1} & \frac{\partial E_3}{\partial Q_2} & \frac{\partial E_3}{\partial Q_3} & \frac{\partial E_3}{\partial Q_4} \\ \frac{\partial E_4}{\partial Q_1} & \frac{\partial E_4}{\partial Q_2} & \frac{\partial E_4}{\partial Q_3} & \frac{\partial E_4}{\partial Q_4} \end{bmatrix} \begin{bmatrix} \Delta Q_1 \\ \Delta Q_2 \\ \Delta Q_3 \\ \Delta Q_4 \end{bmatrix}\quad (25)$$

which in a compact form yields:

$$[\Delta E] = [s_Q][\Delta Q]\quad (26)$$

where  $[s_Q]$  is the reactive sensitivity matrix,  $[\Delta Q]$  is the reactive power-variations vector and  $[\Delta E]$  is the nodal voltages vector.

Calculating the partial derivatives contained in  $[s_Q]$ , we have Equation (27).

After analyzing this form of (27), we can say that this matrix can be built using the following inspection rule:

“The element  $i, j$  is the arithmetic sum of the reactance of the branches in which both the powers absorbed by node  $i$  and node  $j$  flow multiplied by  $-1/E_n$ ”.

For example, in (27), the element 2, 4 is

$$[s_Q] = -\frac{1}{E_n} \begin{bmatrix} X_{01} & X_{01} & X_{01} & X_{01} \\ X_{01} & X_{01} + X_{12} & X_{01} + X_{12} & X_{01} + X_{12} \\ X_{01} & X_{01} + X_{12} & X_{01} + X_{12} + X_{23} & X_{01} + X_{12} \\ X_{01} & X_{01} + X_{12} & X_{01} + X_{12} & X_{01} + X_{12} + X_{24} \end{bmatrix}\quad (27)$$

$$-(X_{01} + X_{12})/E_n$$

because the powers delivered by node 2 and node 4 flow in branches 01 and 12.

### 3.3 The Choice of the Best Generator

The BG is the generator that has the greatest influence on node  $i$ , which is the node where the voltage exceeds the threshold.

Thus, after analyzing (25), we can say that the BG is the generator that maximizes the following product, which we call the “sensitivity product”:

$$\frac{\partial E_i}{\partial Q_j} \Delta Q_j\quad (28)$$

For example, if the node with a voltage that exceeds  $V_{max}$  is  $i=2$  and the BG is connected to node  $j=4$ , the sensitivity product  $(\partial E_2/\partial Q_4)\Delta Q_4$  is the highest compared to the other products contained in row 2 of the sensitivity matrix. In addition, in order to choose the BG, it is necessary to evaluate the single products (28) of the row that represents node  $i$ . Thus, the value  $\Delta Q_j$  is needed and is acquired as the GCC polls the GRTUs, as stated previously.

The procedure described above suggests a way of defining the “sensitivity table”  $[T_s]$  that contains the single sensitivity products. For the MVDN represented in **Figure 4**,  $[T_s]$  takes the following form

$$\begin{bmatrix} \frac{\partial E_1}{\partial Q_1} \Delta Q_1 & \frac{\partial E_1}{\partial Q_2} \Delta Q_2 & \frac{\partial E_1}{\partial Q_3} \Delta Q_3 & \frac{\partial E_1}{\partial Q_4} \Delta Q_4 \\ \frac{\partial E_2}{\partial Q_1} \Delta Q_1 & \frac{\partial E_2}{\partial Q_2} \Delta Q_2 & \frac{\partial E_2}{\partial Q_3} \Delta Q_3 & \frac{\partial E_2}{\partial Q_4} \Delta Q_4 \\ \frac{\partial E_3}{\partial Q_1} \Delta Q_1 & \frac{\partial E_3}{\partial Q_2} \Delta Q_2 & \frac{\partial E_3}{\partial Q_3} \Delta Q_3 & \frac{\partial E_3}{\partial Q_4} \Delta Q_4 \\ \frac{\partial E_4}{\partial Q_1} \Delta Q_1 & \frac{\partial E_4}{\partial Q_2} \Delta Q_2 & \frac{\partial E_4}{\partial Q_3} \Delta Q_3 & \frac{\partial E_4}{\partial Q_4} \Delta Q_4 \end{bmatrix}\quad (29)$$

Row  $i$  represents the node in which we want to control the voltage, and column  $j$  represents the nodes in which we can control the reactive power. The BG is the generator connected to node  $j$  that has the maximum absolute value of the sensitivity product in position  $i, j$ . By finding the maximum sensitivity product in row  $i$ ,



last poll are those summarized in **Table 4**, which also contains the corresponding power factors  $\cos\phi$ . To calculate the sensitivity table, we need the single-phase powers. Therefore, the reactive powers shown in **Table 4** have to be divided by three. It is important to note that the reactive powers calculated this way correspond to  $\Delta Q_j$  because  $Q_j^0$  is zero (see (21)). The  $\Delta Q_j$  values are shown in **Table 5**.

The voltage exceeds the threshold in node 5. Thus, we only consider the fifth row of the sensitivity table. According to the inspection rule mentioned above, this row is as follows:

$$\begin{bmatrix} 0 & 0 & 0 & t_{S5,4} & t_{S5,5} & t_{S5,6} & t_{S5,7} & 0 \end{bmatrix} \quad (31)$$

where the single sensitivity products  $t_{S_{i,j}}$  are:

$$t_{S5,4} = -\frac{1}{E_n}(X_a + X_e)\Delta Q_4 = -164.53 \text{ V} \quad (32)$$

$$t_{S5,5} = -\frac{1}{E_n}(X_a + X_e + X_h)\Delta Q_5 = 0 \text{ V} \quad (33)$$

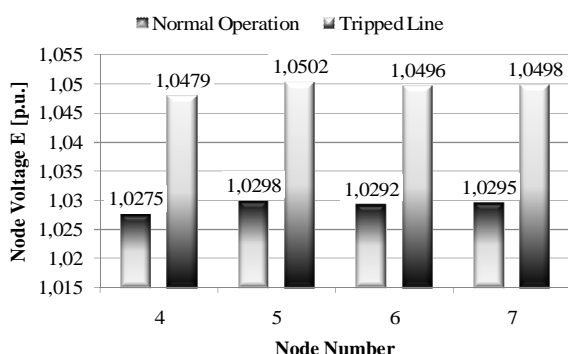


**Figure 6.** Load-Flow results with the Network Normal Operation

**Table 4.** Reactive powers absorbable by the generators

Generator	$Q$ [MVAR]	$\cos\phi$
$G_4$	1.97	0.95
$G_5$	0.00	1
$G_6$	0.91	0.98
$G_7$	1.23	0.95

**Table 5.** Reactive Power Variations in the Generator Nodes

Generator	$\Delta Q_j$ [MVAR]
$G_4$	0.66
$G_5$	0.00
$G_6$	0.30
$G_7$	0.41

$$t_{S5,6} = -\frac{1}{E_n}(X_a + X_e + X_h)\Delta Q_6 = -98.65 \text{ V} \quad (34)$$

$$t_{S5,7} = -\frac{1}{E_n}(X_a + X_e + X_h)\Delta Q_7 = -133.07 \text{ V} \quad (35)$$

The maximum sensitivity product (in absolute value) corresponds to generator 4, (*i.e.*,  $j = 4$ ). Thus, the BG is  $G_4$ .

Equation (32) provides important information. If  $G_4$  performs the considered reactive power variation, the line-to-ground voltage variation in node 5 is:

$$\Delta E_5 = -164.53 \text{ V} \rightarrow -0.0142 \text{ p.u.} \quad (36)$$

Then, considering (22) (rewritten for node 5), and  $E_5^0 = 1.0502 \text{ p.u.}$  from **Figure 6**, we can say that the voltage value after the reactive power variation is:

$$E_5^f = E_5^0 + \Delta E_5 = 1.036 \text{ p.u.} \quad (37)$$

which is less than the voltage threshold  $V_{max}$ .

Equation (37) shows the theoretical result obtained using the proposed method. We checked this value using load-flow software:

$$E_5^f \text{ load flow} = 1.034 \text{ p.u.} \quad (38)$$

The percentage error between (38) and (37) is:

$$\varepsilon_{\%} = \frac{E_5^f \text{ load flow} - E_5^f}{E_5^f \text{ load flow}} \cdot 100 = -0.19 \% \quad (39)$$

which is negligible and demonstrates the validity of the proposed approach.

## 5. Conclusions

The proposed sensitivity method allows the voltage within network acting on single generators to be regulated by choosing the most effective generator on the controlled node (*i.e.*, the Best Generator). This is a very important feature in grids that have distributed generation (*e.g.*, in a Smart Grid context).

The proposed method uses a topological approach. Moreover, the sensitivity table can be constructed automatically.

In addition to the BG choice, the proposed method also evaluates the voltage in all network nodes after a reactive power variation.

After choosing the BG, but before its commutation during RPA, it is possible to verify that the voltage variation in the other nodes is tolerable for the connected loads. Moreover, it is necessary to verify that the threshold settings of the voltage relay installed in the same nodes.

When a generator is switched during RPA, it works with a non-unitary power factor; the reactive power flow increases along the lines and increases the power loss [16].

This phenomenon is negligible in HV networks because the line resistance is typically smaller than the line reactance, but is important to consider in MV networks.

Therefore, if network analysis reveals that the RPA-switching produces high losses, voltage control using the reactive power variation must only be used for temporary voltage variation mitigation (*i.e.*, during emergency conditions).

The possible future develops of this work could be focused on the optimization of the forecasted power-time profiles of the loads and generators applying both the sensitivity approach and distributed voltage measurement.

## REFERENCES

- [1] R. Marconato, "Electric Power Systems," Vol. 2, CEL, Milano, 2008.
- [2] P. Kundur, "Power System Stability and Control," McGraw-Hill, New York, 1994.
- [3] Y. Rosales Hernandez and T. Hiyama, "Distance Measure Based Rules for Voltage Regulation with Loss Reduction", *Journal of Electromagnetic Analysis and Applications (JEMAA)*, Vol. 1, No. 2, June 2009, pp. 85-91.
- [4] F. Saccomanno, "Electric Power Systems" Wiley-Interscience IEEE Press, Piscataway, 2003.
- [5] G. Andersson, "Modeling and Analysis of Electric Power Systems" *Lecture 227-0526-00, ITET ETH Zürich, Zürich*, 2008.
- [6] Y. Abdel-Rady, I. Mohamed and E. F. El-Saadany "A Control Scheme for PWM Voltage-Source Distributed-Generation Inverters for Fast Load-Voltage Regulation and Effective Mitigation of Unbalanced Voltage Disturbances" *IEEE Transactions on Industrial Electronics*, Vol. 55, No. 5, May 2008, pp. 2072-2084.
- [7] P. M. S. Carvalho, P. F. Correia and L. A. F. M. Ferreira, "Distributed Reactive Power Generation Control for Voltage Rise Mitigation in Distribution Networks," *IEEE Transactions on Power Systems*, Vol. 23, No. 2, 2008, pp. 766-772.
- [8] P. N. Vovos, A. E. Kiprakis, A. R. Wallace and G. P. Harrison, "Centralized and Distributed Voltage Control: Impact on Distributed Generation Penetration," *IEEE Transactions on Power Systems*, Vol. 22, No. 1, 2007, pp. 476-483.
- [9] P. M. Anderson, "Power System Protection," IEEE Press, Piscataway, 1999.
- [10] N. Mohan, T. M. Undeland and W. P. Robbins, "Power Electronics: Converters, Applications, and Design", Wiley, 1995.
- [11] M. H. Rashid, "Power Electronics Handbook", Academic Press-Elsevier, 2007.
- [12] L. L. Grigsby, "Electric Power Generation, Transmission and Distribution," CRC Press-Taylor & Francis Group, Boca Raton, 2006.
- [13] F. A. Viawan and D. Karlsson, "Coordinated Voltage and Reactive Power Control in the Presence of Distributed Generation," *PES General Meeting - Conversion and Delivery of Electrical Energy in the 21st Century*, IEEE, Pittsburgh, 2008, pp. 1-6.
- [14] S. Corsi, "Wide Area Voltage Regulation & Protection" *2009 IEEE Bucharest Power Tech Conference*, Bucharest, June 28 -July 2, Bucharest, pp. 1-7.
- [15] A. Gandelli, S. Leva and A. P. Morando, "Topological Considerations on the Symmetrical Components Transformation", *IEEE Transactions on Circuits and Systems I: Fundamental Theory and Applications*, Vol. 47, No. 8, August 2000, pp. 1202-1211.
- [16] H. M. Ayres, L. C. P. da Silva, W. Freitas, M. C. de Almeida and V. F. da Costa, "Evaluation of the Impact of Distributed Generation on Power Losses by Using a Sensitivity-Based Method," *IEEE Power & Energy Society General Meeting*, Calgary, 2009, pp. 1-6.
- [17] A. Kishore and E. F. Hill, "Static optimization of Reactive Power Sources by use of Sensitivity Parameters", *IEEE Transactions on Power Apparatus and Systems*, Vol. PAS-90, No. 3, 1971, pp. 1166-1173.

# Impact of Wind Farms of DFIG Type on Power System Transient Stability\*

Libao Shi<sup>1</sup>, Shiqiang Dai<sup>1</sup>, Liangzhong Yao<sup>2</sup>, Yixin Ni<sup>1</sup>, Masoud Bazargan<sup>2</sup>

<sup>1</sup>National Key Laboratory of Power System in Shenzhen, Graduate school at Shenzhen, Tsinghua University, Shenzhen, China;  
<sup>2</sup>AREVA T&D Technology Centre, Stafford, UK.

Email: shilb@sz.tsinghua.edu.cn, liangzhong.yao@areva-td.com

Received May 23<sup>rd</sup>, 2010; revised June 22<sup>nd</sup>, 2010; accepted July 2<sup>nd</sup>, 2010

## ABSTRACT

*The impact of large-scale grid-connected wind farms of Doubly-fed Induction Generator (DFIG) type on power system transient stability is elaborately discussed in this paper. In accordance with an equivalent generator/converter model, the comprehensive numerical simulations with multiple wind farms of DFIG type involved are carried out to reveal the impact of wind farm on dynamic behavior of existing interconnected power system. Different load models involving nonlinear load model and induction motor model are considered during simulations. Finally, some preliminary conclusions are summarized and discussed.*

**Keywords:** Transient Stability, DFIG, Multiple Wind Farms, Wind Farm Integration, Load Model

## 1. Introduction

In recent years, the increasing concerns to the environmental issues and the limited availability of conventional fossil fuels lead to rapid research and development for more sustainable and alternative electrical sources. Wind energy, as one of the most prominent renewable energy sources, is gaining increasing significance throughout the world. The currently worldwide installed capacity of grid-connected wind generators grows rapidly, and particularly in China, the installed capacity doubles every year since 2004. The vast majority of presently installed wind turbines are based on the following three main types of electromechanical conversion systems. The 1<sup>st</sup> type is normally referred to as a constant-speed or fixed-speed turbine. The 2<sup>nd</sup> type uses a DFIG instead of a SCIG as a variable-speed wind turbine. The 3<sup>rd</sup> type is called a direct-drive synchronous generator different from the DFIG. The fixed-speed wind turbines equipped with an induction generator (squirrel cage or wound rotor) have ever been widely used because of the advantage of being simple, robust, reliable and well-proven. Also the cost of its electrical parts is low. However, the disadvantages of uncontrollable reactive power consumption, mechanical stress and limited power quality control lead to little con-

tributions on improving system dynamic behavior. Especially, owing to its fixed speed operation, all fluctuations in the wind speed are further transmitted as fluctuations in the mechanical torque and then as fluctuations in the electrical power on the grid. With rapid development in power electronic converters recently, an alternative, the variable-speed wind turbine, has appeared during the past few years and has become the dominant type among the new installed wind turbines. It should be pointed out that the Doubly-fed Induction Generator (DFIG) equipped wind turbine is currently the most popular one due to its capability of controlling reactive power, high energy efficiency, and the fact that the converter rating of appropriately 20%-30% of the total machine power is needed [1,2]. Accordingly, modeling of wind turbine with DFIG will be the highlight to be issued in this paper.

It is known that the electrical characteristics of DFIG determined by the converter are quite different from the conventional synchronous generators. Power system engineers will have to confront a series of challenges imposed by integration of large wind power with the existing power systems. One of important issues engineers have to face is the impact of wind power penetration on the dynamic behavior, e.g. the transient stability, of an existing interconnected large-scale power system.

So far, much literature related to transient stability analysis of power system with high penetration of grid-connected wind farms of DFIG type have been studied

\*This work has also been supported in part by the National Natural Science Foundation of China (50977051), the Research Project of Science and Technology from Shenzhen Government of China (JC200903 180528A)

in [3-9]. Vicatos, Tegopoulos [3] and Senjyu *et al.* [4] discussed the transient characteristics of wind farm during the three-phase short circuit condition. Jenkins *et al.* [5] and Shi *et al.* [6] studied dynamic mathematical model of DFIG suitable for transient stability analysis. Muyeen *et al.* [7] presented detailed analysis of windmill mechanical drive train models for transient stability analysis of wind power generation system. They pointed out that at least two-mass shaft model was needed in the transient stability analysis of wind turbine generation system. Gautam *et al.* [8] and Weise *et al.* [9] examined the impact of high wind generation penetration on transient stability and small signal stability of an existing power system. Shi *et al.* [10] studied the influence of DFIG type wind farms on transient stability of the power system, while comparing with the synchronous generators connected to the power system at the same point.

In the published literature, some of them mainly focused on the electromagnetic transient models [3,4] unsuitable for transient stability analysis of large-scale power system. As for the applications of the electromechanical transient model of DFIG in an existing power system [8-10], some studied test systems were too simple and the impact of dynamic load model was neglected during simulations. Besides, only single wind farm [8,10] was introduced to conduct the transient stability analysis. In a nutshell, the transient stability analysis of power system with high penetration of wind farms of DFIG type needs to be elaborately explored and exploited further.

In this paper, the detail numerical simulations on the IEEE 10-generator-39-bus New England test system as benchmark are carried out to discuss the influence and interaction of DFIG type wind farms on power system transient stability. Multiple wind farms are introduced into the existing test system during analysis by replacing the existing synchronous generators and integrating into the nonlinear and dynamic motor models are also considered. Finally, some meaningful and preliminary conclusions are given in this paper.

The rest of this paper is organized as follows. Section 2 briefly introduces the mathematical models of DFIG and converters. In Section 3, the detail case studies focusing on the impacts of grid-connected wind farms on an existing test system are carried out. Finally the conclusions and discussions are summarized in Section 4.

## 2. Modeling of DFIG and Converters

In the following discussions, the whole wind farm is modeled as an aggregated wind park model by one equivalent wind generator [1,2]. A general scheme of a DFIG including the static converters and controllers is depicted in **Figure 1**. Two converters are connected be-

tween the rotor and grid, following a back-to-back scheme with a dc intermediate link.

In the modeling of turbine rotor, there are a lot of different ways to represent the wind turbine [1]. In our studies, a kind of functions approximation method [11] is used to simulate the wind turbine aerodynamic model. Furthermore, we assume that the wind speed can be kept as constant during the transient stability simulation. The pitch angle control strategy is also considered, which is implemented by a kind of PI controller [11], to limit the aerodynamic efficiency of the rotor.

For the modeling of DFIG, a two-mass shaft model [10,11] is employed to represent the drive train. The interface between the wind turbine generator and the network is simplified as an algebraic, controlled-current source [10,11] which computes the required injected current into the network in response to the flux and active current commands from the converter model. For a given time step, the model holds the in-phase (active power) component of current constant and holds constant q-axis voltage behind the sub-transient reactance ( $X''$ ).

The model of the frequency converter system is generally represented with the rotor-side converter, grid-side converter, the dc link and the corresponding converter control. The modeling of rotor-side converter from [11] is employed to implement the decoupled control for stator active and reactive powers. The corresponding control block diagrams are shown in **Figure 2** and **Figure 3**.

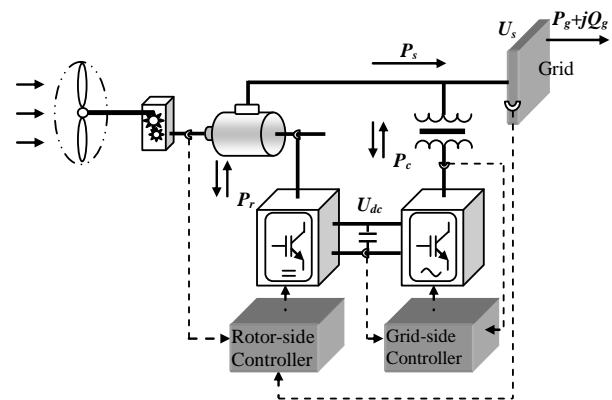


**Figure 1. General scheme of a DFIG including converters and controllers**

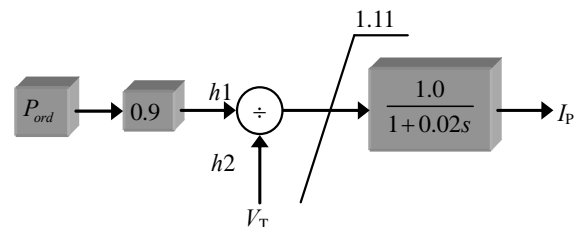


**Figure 2. Block diagram for active power control**

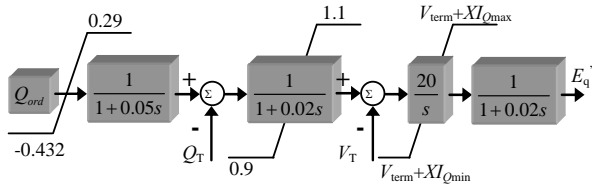


Figure 3. Block diagram for reactive power control

Where,  $P_{ord}$  is the active power demand determined by wind turbine;  $V_T$  is terminal voltage considering measurement block;  $Q_{ord}$  is reactive power demand determined by the supervisory VAR controller;  $E_q''$  and  $I_p$  are the flux and active current commands from the converter model [11]. In our studies, the grid-side converter is assumed to be ideal, and the dc link voltage between the converters is kept as constant.

### 3. Case Study

#### 3.1 Transient Stability Evaluation Index

In our work, the following two indices [12,13] are used to evaluate the impact of grid-connected wind farms of DFIG type on the transient stability of the test system.

1) Power angle based stability index [13]

This index is defined as follows for each island in the system:

$$\eta = \frac{360 - \delta_{\max}}{360 + \delta_{\max}} \times 100 \quad -100 < \eta < 100 \quad (3)$$

where  $\delta_{\max}$  is the maximum angle separation of any two generators in the island at the same time in the post-fault response. The transient stability index for the system is taken from the smallest index among all islands. Thus,  $\eta > 0$  and  $\eta \leq 0$  correspond to stable and unstable conditions respectively. This index is directly proportional to system angle separation. Hence it provides a good indication of how severe a test system is following a contingency.

2) Critical clearance time (CCT) of faults [13]

The critical clearance time of a fault is generally considered as the best measurement of severity of a contingency and thus widely used for ranking contingencies in accordance with their severity. In our studies, the CCT is employed as a transient stability index to evaluate the test system. CCT is defined as the longest allowed fault clearance time without losing stability. This is obtained, using a binary search method [13], within a specified fault clearance range with a set threshold. If the change of the system operation can increase CCT, it is considered that such change is favorable to improve power system transient stability.

#### 3.2 Application Example

The IEEE 10-generator-39-bus New England test system

shown in **Figure 4** is employed to conduct the transient stability simulation. Detailed parameters of this system can be found in [14]. All simulations are implemented on the DSA-TSAT/UDM™ [12] simulation environment, developed by Powertech Labs Inc., Canada.

#### 3.2.1 Multiple Wind Farms Replacing Synchronous Generators

In order to make more sense to replace the synchronous generators with wind farms for the power system transient stability analysis, we made a comprehensive transient stability analysis with three-phase temporary fault on each bus (excluding the generators' terminal buses) in advance. We found that the worst transient stability index (with the most negative value of  $\eta$ ) corresponds to a three-phase fault condition occurred at Bus29. In this condition, the maximum angle separation happens between generator SG38 and generator SG39. Thus, in the following simulations, the generators SG38 and SG39 will be replaced by the wind farms equipped with GE 3.6MW [11] DFIGs with three-phase fault condition at Bus29 as benchmark to analyze the impacts of wind farm integration on the dynamic behavior of the test power system. We designed the following experimental scenarios: 1) In scenario 1, the synchronous generators SG38 and SG39 at Bus38 and Bus39 are equipped with exciters and power system stabilizers. The 4th order practical generator model is applied to the remaining synchronous generators. 2) In scenario 2, the synchronous generators SG38 at Bus38 is replaced by a wind farm DFIG38 with the same power output. The synchronous generator SG39 at Bus39 is equipped with exciters and power system stabilizers. The remaining synchronous generators are modeled as the 4th order practical model. 3) In scenario 3, the synchron-

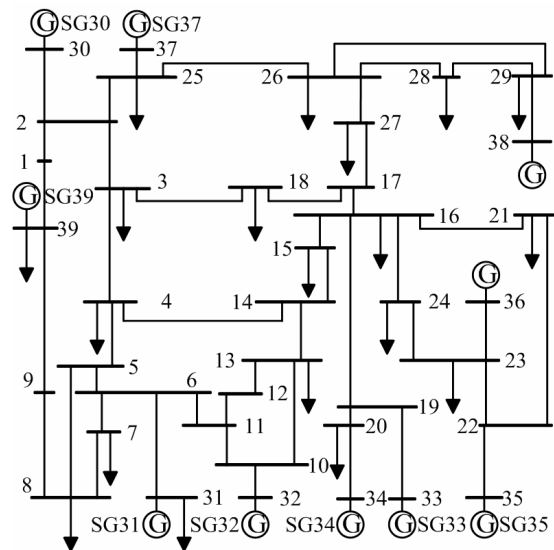


Figure 4. IEEE standard 10-generator-39-bus New England system

ous generators SG38 and SG39 are replaced by wind farms DFIG38 and DFIG39 with the same power outputs, respectively. Similarly, the 4th order practical generator model is applied to the remaining synchronous generators. The corresponding experimental scenarios are summarized in **Table 1**.

As mentioned before, different load models involving the nonlinear load model and dynamic load model will be considered during the simulation comparisons. The applied load models are given in **Table 2**.

A three-phase temporary fault occurs at Bus29 at time  $t = 0.5$  s, and it is cleared at time  $t = 0.55$  s. The corresponding calculated transient stability indices considering different load models are given in **Table 3** and **Figures 5-6**.

**Table 1. Designed experimental scenario**

Scenario	Synchronous Generators Replaced by Wind Farms
1	N/A
2	SG38
3	SG38 and SG39

**Table 2. Load model considerations**

Load Model	Description
Z	Constant impedance
ZIP	Combination of 30% constant impedance (Z), 40% constant current (I) and 30% constant power (P)
ZIP + Dyn	Combination of 30% ZIP and 70% induction motor

**Table 3. Transient stability evaluation indices considering different load models**

Scenario \ Load Model	1		2		3	
	$\eta$	CCT(s)	$\eta$	CCT(s)	$\eta$	CCT(s)
Z	60.70	0.1379	66.60	0.5399	69.85	1.4712
ZIP	59.58	0.1238	67.14	0.4402	70.17	0.9987
ZIP+Dyn	Insecure(-57.95)	0.0421	67.58	0.0746	68.50	0.0676

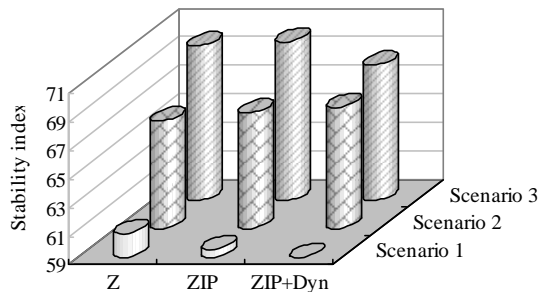


**Figure 5. Power angle based stability indices with different scenarios and load models**

From **Table 3** and **Figures 5-6**, it can be seen that the system transient stability can be improved to some extent when the specific synchronous generator is replaced by a wind farm of DFIG type under current fault condition and with the consideration of different load models. It should be noticed that when considering the ‘ZIP + Dyn’ load models the power system consisting of all conventional synchronous generators (*i.e.* scenario 1) becomes unstable.

The maximum angle separation changes in different scenarios considering the ‘ZIP + Dyn’ load models. The corresponding maximum angle separations are given in **Table 4**.

From **Table 4**, it can be seen that the oscillation modes related to the transient stability index will change when some synchronous generators are replaced by wind farms of DFIG type.

**Figures 7(a), 7(b), 7(c) and 7(d)** show the active power output, rotor speed, reactive power output and terminal voltage curves of the wind farm DFIG38 and the replaced synchronous generator SG38 considering the ‘ZIP + Dyn’ load model, respectively. The solid line corresponds to the DFIG38 and the dotted line corresponds to the synchronous generator SG38. These figures show that the dynamic behavior of test system resulted in great changes after the introduction of wind farm of DFIG type. Under current condition, the synchronous generators cannot keep stable with great penetration of induction motor loads, which may lead to more reactive power requirements and more complicated oscillations. With the control strategies of DFIG converter and due to the soft connection between the mechanical and the electrical side of DFIG, the active and reactive power oscillations of DFIG during fault is relatively smooth, which is helpful for keeping the power system stable.

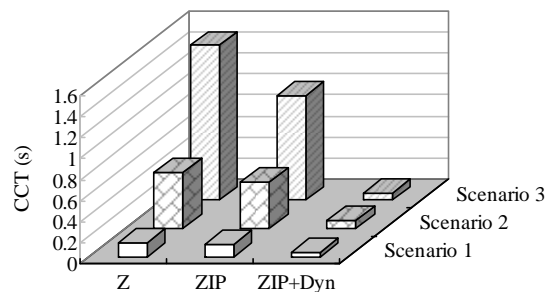


**Figure 6. CCT with different scenarios and load models**

**Table 4. Maximum angle separations in different scenarios**

Scenario	Load Model	Maximum Angle Separation
1		<SG34, SG39>
2	ZIP+Dyn	<SG31, SG39>
3		<SG30, SG31>

Similarly, **Figures 8(a), 8(b), 8(c) and 8(d)** give the active power output, rotor speed, reactive power output and terminal voltage curves of the wind farm DFIG39 and the replaced synchronous generator SG39 considering the ‘ZIP + Dyn’ load model, respectively. The dotted line corresponds to synchronous generator SG39 based on scenario 1; the dash-dot line corresponds to the synchronous generator SG39 based on scenario 2 and the solid line corresponds to the DFIG39 based on scenario 3.

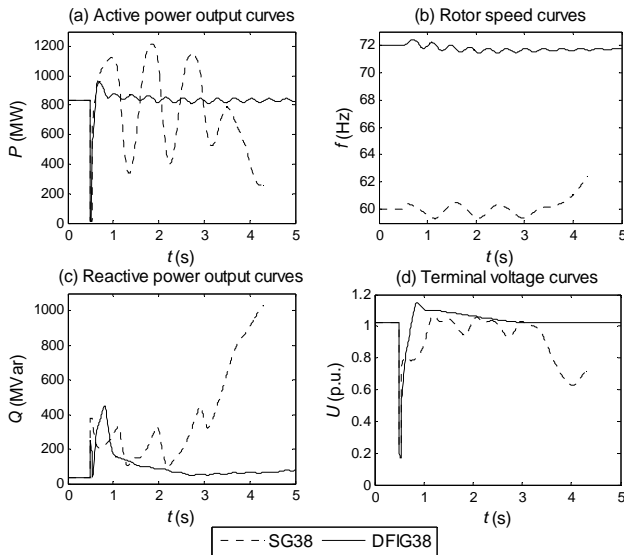


**Figure 7. Transient behavior curves of the wind farm DFIG38 and the replaced synchronous generator SG38**

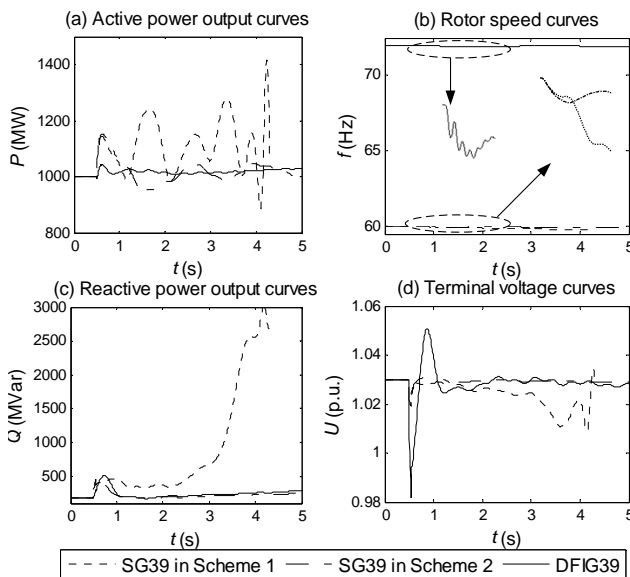


**Figure 8. Transient behavior curves of the wind farm DFIG39 in scenario 3 and the replaced synchronous generator SG39 in scenario 1 and scenario 2**

It can be seen from **Figure 8** that wind farms of DFIG type replacing synchronous generators actually leads to great influence on the transient stability of the existing power system. Particularly, when the second wind farm DFIG39 is introduced into the test system, the transient stability of the test system is significantly improved.

### 3.2.2 Wind Farms Connected to Existing Power Grid

In our previous analysis of impact of grid-connected wind farm of DFIG type on transient stability, the wind farms are introduced into the power grid via replacing existing synchronous generators. Actually, it is unpractical to replace the existing synchronous generators with wind farms during application. When the wind farm is directly connected to the transmission system, the corresponding network topology and system operating condition will change. Therefore, it is necessary and imperative to explore and exploit the impact on the power system transient stability in this situation.

In following simulations, the wind farm equipped with GE 3.6MW DFIGs will be connected to each bus excluding generator buses to carry out the corresponding analysis. The synchronous generators are modeled as the 4<sup>th</sup> order practical model. The load model which is a combination of 30% ZIP and 70% induction motor (‘ZIP + Dyn’) is considered as well. A three-phase temporary fault occurs at Bus29 at time  $t = 0.5s$ , and it is cleared at time  $t = 0.55s$ . Consider that the load demands do not change before and after the integration of wind farm, the power outputs of each synchronous generator are decreased by 10 percent of wind farm rated capacity to meet load requirements. And in our studies, the wind farms at all grid connection points have to be able to operate at power factor between 0.975 lagging and 0.975 leading to provide reactive power. The corresponding calculated transient stability indices and maximum angle separations are given in **Table 5**.

From **Table 5**, it can be seen that when the wind farm is connected to most buses, the system transient stability can be increased under the specific fault condition with the consideration of the ‘ZIP + Dyn’ load models. Furthermore, the CCT is different with the different connection point of wind farm. The maximum CCT value is 0.0816 calculated at Bus26 with wind farm connected. The minimum CCT value is 0.0421 calculated at Bus1. Regarding the oscillation mode which may make the system transient stability unstable, we found that the maximum angle separation happens between synchronous generators SG38 and SG39 for almost all connection points of wind farm. When the wind farm is connected to bus20, the maximum angle separation is between SG34 and SG39.

**Figures 9(a), 9(b), 9(c) and 9(d)** show the active power output, rotor speed, reactive power output and terminal voltage curves of the wind farm of DFIG type connected to Bus 26 and Bus 1 considering the ‘ZIP + Dyn’ load model, respectively. The solid line corresponds to the

**Table 5. Transient stability indices and corresponding maximum angle separations**

Bus Number Connected Wind Farm	Transient Stability Indices		Maximum Angle Separation
	$\eta$	CCT(s)	
1	Insecure(-58.32)	0.0421	<SG38,SG39>
2	60.69	0.0676	<SG38,SG39>
3	59.74	0.0676	<SG38,SG39>
4	60.22	0.0605	<SG38,SG39>
5	60.78	0.0605	<SG38,SG39>
6	60.79	0.0605	<SG38,SG39>
7	61.06	0.0605	<SG38,SG39>
8	61.21	0.0605	<SG38,SG39>
9	Insecure(-57.26)	0.0474	<SG38,SG39>
10	60.47	0.0605	<SG38,SG39>
11	60.57	0.0605	<SG38,SG39>
12	60.34	0.0535	<SG38,SG39>
13	60.38	0.0605	<SG38,SG39>
14	60.10	0.0605	<SG38,SG39>
15	59.32	0.0605	<SG38,SG39>
16	59.04	0.0676	<SG38,SG39>
17	59.13	0.0676	<SG38,SG39>
18	59.43	0.0676	<SG38,SG39>
19	59.19	0.0605	<SG38,SG39>
20	58.34	0.0605	<SG34,SG39>
21	59.13	0.0605	<SG38,SG39>
22	59.15	0.0605	<SG38,SG39>
23	59.10	0.0605	<SG38,SG39>
24	59.30	0.0676	<SG38,SG39>
25	60.50	0.0746	<SG38,SG39>
26	58.70	0.0816	<SG38,SG39>
27	58.75	0.0746	<SG38,SG39>
28	53.94	0.0676	<SG38,SG39>
No wind farm connected	Insecure(-78.30)	0.0159	<SG38,SG39>

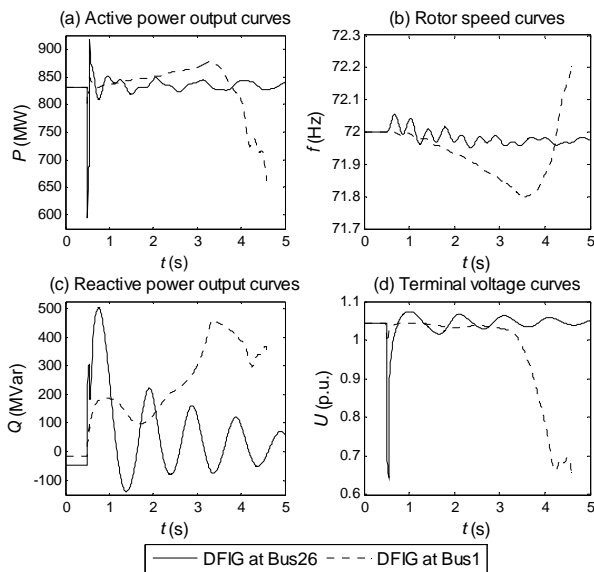


**Figure 9. Transient behavior curves of the wind farms connected at Bus26 and Bus1**

wind farm of DFIG type connected to Bus26 and the dotted line corresponds to the wind farm connected to Bus 1.

### 4. Conclusions

The transient stability simulation of power system with consideration of large-scale grid-connected wind farms of DFIG type are elaborately studied in this paper. The multiple wind farm integration with replacing synchronous generators is studied first. Furthermore, the impact on the power system transient stability with direct connection of wind farm of DFIG type is explored and exploited as well. According to the simulation results, some preliminary conclusions and comments are summarized and discussed. It should be pointed out that these conclusions and comments can provide useful information for power system planning and design when considering integrations of large wind farms with the existing power system. However, they are still preliminary and very limited. The impact of wind power on the transient stability of power systems involving the more actual factors needs to be elaborately studied further in the near future.

### REFERENCES

- [1] T. Ackermann, "Wind Power in Power Systems," Wiley, Chichester, 2005.
- [2] E. Denny and M. O'Malley, "Wind Generation, Power System Operation, and Emissions Reduction," *IEEE Transaction on Power Systems*, Vol. 21, February 2006, pp. 341-347.
- [3] M. S. Vicatos and J. A. Tegopoulos, "Transient State Analysis of a Doubly-Fed Induction Generator under Three Phase Short Circuit," *IEEE Transaction on Energy Conversion*, Vol. 6, March 2003, pp. 62-68.
- [4] T. Senjyu, N. Sueyoshi, K. Uezato, H. Fujita and T. Funabashi, "Transient Stability Analysis of Induction Generator Using Torque-time Characteristic," *The 5th International Conference on Power Electronics and Drive Systems*, Vol. 1, Singapore, 2003, pp. 760-765.
- [5] J. B. Ekanayake, L. Holdsworth, X. Wu and N. Jenkins, "Dynamic Modeling of Doubly Fed Induction Generator Wind Turbines," *IEEE Transaction on Power Systems*, Vol. 18, May 2003, pp. 803-809.
- [6] L. B. Shi, Z. Xu, J. Hao and Y.X. Ni, "Modeling Analysis of Transient Stability Simulation with High Penetration of Grid-connected Wind Farms of DFIG Type," *Wind Energy*, Vol. 10, March 2007, pp. 303-320.
- [7] S. M. Mueeen, H. A. Mohd, R. Takahashi, T. Tamura, Y. Tomaki, A. Sakahara and E. Sasano, "Transient Stability Analysis of Wind Generator System with the Consideration of Multi-mass Shaft Model," *International Conference on Power Electronics and Drives Systems*, Vol. 1, 2005, pp. 511-516.
- [8] D. Gautam, V. Vittal and T. Harbour, "Impact of In-

- creased Penetration of DFIG-based Wind Turbine Generators on Transient and Small Signal Stability of Power Systems,” *IEEE Transaction on Power Systems*, Vol. 24, August 2009, pp. 1426-1434.
- [9] B. Weise and M. Pöller, “Impact of High Wind Penetration on Transient and Oscillatory Stability Analysis,” *IEEE Power & Energy Society General Meeting*, Calgary, October 2009, pp. 16-22.
- [10] L. B. Shi, S. Q. Dai, Y. X. Ni, Y. D. Zhao and M. Bazaragan, “Transient Stability of Power System with High Penetration of DFIG based Wind Farms,” *IEEE Power & Energy Society General Meeting*, Calgary, October 2009, pp. 1-6.
- [11] N. W. Miller, J. J. Sanchez-Gasca, W. W. Price and R. W. Delmerico, “Dynamic Modeling of GE 1.5 and 3.6 MW Wind Turbine-generators for Stability Simulations,” *IEEE Power Engineering Society General Meeting*, Toronto, 2003, pp. 1977-1983.
- [12] <http://www.powertech.bc.ca>; <http://www.dsapowertools.com/>
- [13] Powertech Labs Inc. TSA user manual (version 6.0), Canada, April 2006.
- [14] M. A. Pai, “Energy Function Analysis for Power System Stability,” Kluwer Academic Publishers, Boston, 1989.

# Induction of Oxidative Stress in Male Rats Subchronically Exposed to Electromagnetic Fields at Non-Thermal Intensities

Albert Achudume<sup>1</sup>, Bill Onibere<sup>1</sup>, Funso Aina<sup>1</sup>, Paschal Tchokossa<sup>2</sup>

<sup>1</sup>Institute of Ecology and Environmental Studies, Obafemi Awolowo University, Ile-Ife, Nigeria; <sup>2</sup>Department of Physic and Radiation, Obafemi Awolowo University, Ile-Ife, Nigeria.  
Email: {aachudume, jedii2000, funsoaina2002, ptchoko}@yahoo.com

Received February 16<sup>th</sup>, 2010; revised May 14<sup>th</sup>, 2010; accepted May 21<sup>st</sup>, 2010.

## ABSTRACT

*To investigate the oxidative stress-inducing potential of non-thermal electromagnetic fields in rats. Male Wister rats were exposed to electrical field intensity of  $2.3 \pm 0.82 \mu\text{V/m}$ . Exposure was in three forms: continuous waves, or modulated at 900 MHz or modulated GSM-nonDTX. The radio frequency radiation (RFR) was 1800 MHz, specific absorption radiation (SAR) (0.95-3.9 W/kg) for 40 and/or 60 days continuously. Control animals were located > 300 m from base station, while sham control animals were located in a similar environmental conditions, but in the vicinity of a non-functional base station. The rats were assessed for thiobarbituric and reactive species (TBARS), reduced glutathione (GSH) content, catalase activity, glutathione reductase (GR) and glucose residue after 40 and 60 days of exposure. At 40 days, electromagnetic radiation failed to induce any significant alterations. However, at 60 days of exposure various attributes evaluated decreased. The respective decreases in both nicotinamide adenine dinucleotide phosphate (NADPH) and Ascorbate-linked lipid peroxidation (LPO) with concomitant diminution in enzymatic antioxidative defense systems resulted in decreased glucose residue. The present studies showed some biochemical changes that may be associated with a prolong exposure to electromagnetic fields and its relationship to the activity of antioxidant system in rat Regular assessment and early detection of antioxidative defense system among people working around the base stations are recommended.*

**Keywords:** Electromagnetic Field, Telecommunication Base Station, Oxidative Stress, Antioxidant System

## 1. Introduction

Human and animals exposure to environmental hazards from low energy electromagnetic fields (EMF) in several countries showed some compelling evidence of DNA damages of cells in in-vitro cultures when exposed EMF [1-3]. These cells are exposed concurrently or sequentially to multiple electromagnetic fields from variety of sources, including mobile phone base stations [3]. Technological advancement in telecommunication network from point or nonpoint sources is an environmental reality in rural and urban areas [4]. The radiation exposure from these antennas is continuous. Some authors [5] believe that chronic, low-level radiation exposure may, over time be as harmful as higher level radiation. Such effects include Fatigue, headache, sleep disruption and loss of memory [4]. Mobile handsets naturally contribute to athermal influences in living organisms [5], implying a

causal relationship in several unspecific symptoms during and after its use [6].

Assessment of potential health risks of EMF are manifested after certain duration of irradiation which indicates long-term cumulative effects. Though, epidemiological studies suggest the existence of weak links between exposure of EMF and human diseases [7] at molecular [8] and cellular levels [9], on immune processes [10], in DNA [11], on the nervous [12], cardiac [13], endocrine [14] reproductive [15] and neurobehavioral effects [16].

Free radical-catalyzed peroxidative damage to membrane lipids may impair the formed elements deformability membrane,  $\text{Na}^+/\text{K}^+$  gradient and metabolic machinery resulting in decreased ATP level and enzyme activity [17]. Several ill healths are due to an imbalance between the activities of an oxidant agent and the antioxidant system within the cell. Cytotoxicity is re-

lated to reactive oxygen species (ROS), viz., superoxide radical ( $\text{O}_2^-$ ), hydrogen peroxide ( $\text{H}_2\text{O}_2$ ), and hydroxyl radical ( $\text{OH}^*$ ), which are produced by various factors. This link causes oxidative damage to cell membrane, increases in oxygen radical's production and ultimately permits leakage of enzymes, leading to organ damage [18]. The consequences of damage to serum are potentially life-threatening and clinically may manifest as hypoxia and several health disorders. To our knowledge, the effects of repeated exposure to electromagnetic fields at non-thermal intensities level on the oxidative stress in serum are not known.

The aim of the current investigation was to evaluate whether concurrent subchronic exposure to electromagnetic fields at non-thermal intensities at environmentally realistic background concentrations and at a concentration equal to World Health Organization (WHO) maximum permissible limit (MPL)[19] can cause oxidative stress in serum of rats and whether oxidative stress is associated with the concomitant diminution in both enzymatic and nonenzymatic lipid peroxidation as well as antioxidant defense systems.

## 2. Materials and Methods

Male Wistar rats weighing between 75-100 g were procured from the Animal Resource Section, Faculty of Pharmacy, Obafemi Awolowo University, Ile-Ife, Nigeria. They were caged in groups of five in clean plastic container with saw-dust chips for bedding. Animals were maintained under standard management conditions and handled following the guidelines of the Federal Environmental Protection Agency (FEPA). All animals were fed everyday given a standard pellet diet (Ladoke feed, Nigeria Ltd.) and deionized water ad libitum. The animals were kept in the vicinity of the base station ground zero consists of three telecommunication antennas and three shelters which contain electric power generators (electrical field intensity of  $2.3 \pm 0.82 \mu\text{V/m}$ ) and radio-frequencies of 900 or 1800 MHz. A model Rados RDS-120 Universal Survey Meter, range 0.05-10  $\mu\text{V/m}$  (Rados Tech, Finland) with automatic selection of measuring range was used to measure radiofrequency and microwaves. The specific absorption rate (SAR) in the animals range from 0.6  $\mu\text{V/m}$ . Comfort 30s Reliable Digital Thermometer (REF 0T11-121c, 070502) was used to measure the temperature around the base stations. The dose-response relationships (non-thermal) are nonlinear [7].

Ten exposed animals were separately kept in the vicinity of base station in non-thermal intensities environment, while ten controlled groups were kept in a similar environment and conditions as the experimental but in nonoperating base station thus served as sham control and ten were housed at a location approximately greater than 300 m from the nearest designated mobile phone base station.

All animals completed the study. The average exposure time for EMF was 24 h for forty and/or sixty days.

At 40<sup>th</sup> day, five exposed five controls and five shams, blood was collected via the tail vein in heparinized tubes and the blood obtained was used for estimation of thiobarbituric acid reactive species (TBARS), reduced glutathione (GSH), catalase activity, glutathione reductase (GR) and residual glucose. At the end of 60<sup>th</sup> day, animals were treated as previously described.

## 3. Measurement of Lipid Peroxidation (LPO)

Enzymatic and non-enzymatic lipid peroxidation was assessed by measuring malondialdehyde (MDA) levels based on the reaction of MDA with thiobarbituric acid [20]. In brief, 200  $\mu\text{l}$  of 30% blood was incubated at  $30 \pm 0.5^\circ\text{C}$  for 30 min. The sample was mixed with 1ml of 10% w/v phosphate buffer solution (PBS), and 1ml of 0.67% thiobarbiturate in boiling water bath for 10min. Reaction was initiated by addition of 1 $\mu\text{l}$  of NADPH (1 mM) and/or ascorbate. After cooling, it was diluted with 1ml distilled water and absorbance was read at 535 nm. Results have been expressed as nmol MDA/ml. NADPH dependent—and ascorbate—linked lipid peroxidation were determined to test the reliability of results (Figure 1).

## 4. Assay for GSH Level

Glutathione content in was estimated following the standard procedure [21]. Briefly, blood (200  $\mu\text{l}$ ) was mixed with 2.5 ml phosphate buffer (0.05M) pH 7 and 200  $\mu\text{l}$  of 5,5' - dithiobis-2-nitro-benzoic acid reagent. Within minutes, absorbance was read at 412 nm. The levels of GSH have been expressed as nmol GSH/ml serum.

## 5. Determination of Catalase

Catalase activity in blood was assayed by the spectrophotometer method [22]. Two hundred microliters were

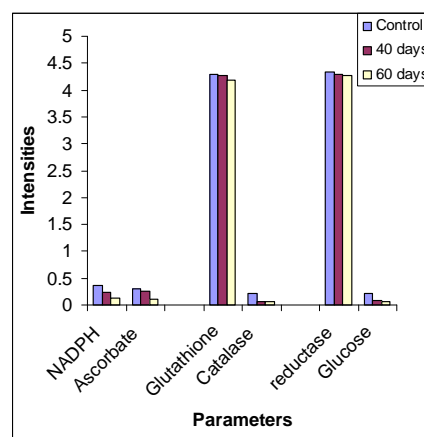


Figure 1. Variations in lipids peroxidation, antioxidative stress and glucose residue

mixed with phosphate buffer (50 mM, pH7) in a curvette. Reaction was started by adding 1ml H<sub>2</sub>O<sub>2</sub> (10 mM) and absorbance was recorded at every 10 sec, for 1min. at 240 nm against water blank. The activity of catalase has been expressed as mmol H<sub>2</sub>O<sub>2</sub> utilized/min/ml.

## 6. Determination of Glutathione Reductase (GR)

Glutathione activity was measured following the standard procedure [23]. The 3 ml reaction mixture contained 2.5 ml PBS (0.12 M, pH 7.2), 0.1 ml EDTA (15 mM), and 0.1 oxidized glutathione (GSSG) (65.3 mM). To this, 100 µl of blood was added and the volume was made up with 0.15 ml distilled water. After incubation at room temperature for 5 min., 0.05ml NADPH (9.6 mM) was added. Decrease in absorbance/min was recorded immediately at 340 nm for 3 min. Control was run without GSSG. The activity of GR has been expressed as unit/ml. One unit is µmol NADPH utilized/min/ml.

## 7. Determination of Residual Glucose

Residual glucose was determined photometrically [24]. Two hundred microliters of blood mixed with 1ml of 5% phenol. Reaction was started by adding 2.5 ml concentrated H<sub>2</sub>SO<sub>4</sub> and absorbance was recorded at 470 nm after thorough mixing at room temperature for 20 min.

The residual glucose has been expressed as nmol glucose/ml.

## 8. Statistics

Statistical analysis: Data were subjected to Barlett's test for homogeneity, followed by analysis of variance (AN-OVA). For post hoc comparison Student Newman Keul's test was employed.

## 9. Results

The temperature at the base stations and the power density at the four corners of the base stations are presented in **Table 1**. Influence of sub chronic exposure to electromagnetic field on various oxidative stress-related parameters in rat whole blood is shown in **Table 2**. Though they have many and varied outputs, at a distance of 50 m (C<sub>1</sub>) the power density is 0.13 µV/m while at distances of 100m at ground level measures 0.69 µV/m (C<sub>2</sub>), between 150 m (C<sub>3</sub>) and 300m, the power density range from 0.69 to 0.74 µV/m (**Table 1**). Results presented demonstrate that the low intensities of electromagnetic fields to rats exposed for forty days failed to induce any significant alterations in any of the oxidative stress-related endpoints in rat. However, at 60 days, exposure duration on the different attributes evaluated for assessing the oxidative stress-inducing potential of electromagnetic field in rat decreased.

**Table 1. In-Situ Measurement of Temperature and Radiation emanating from the GSM Base Stations**

Point	Distance (m)	Temperature (°C)	Dose Rate (µSv/hr)	Dose (µSv)	
Base Station 1 (BS 1)	Corner 1 (C <sub>1</sub> )	0	37	0.17	0.69
	Corner 2 (C <sub>2</sub> )	0	33.8	0.13	0.68
	Corner 3 (C <sub>3</sub> )	0	33.8	0.17	0.68
	Corner 4 (C <sub>4</sub> )	0	37	0.17	0.68
Base Station 2 (BS 2)	Corner 1 (C <sub>1</sub> )	0	37	0.14	0.64
	Corner 2 (C <sub>2</sub> )	0	37	0.13	0.65
	Corner 3 (C <sub>3</sub> )	0	37	0.15	0.64
	Corner 4 (C <sub>4</sub> )	0	37	0.11	0.64
Base Station 3 (BS 3)	Corner 1 (C <sub>1</sub> )	0	37	0.13	0.67
	Corner 2 (C <sub>2</sub> )	0	37	0.16	0.66
	Corner 3 (C <sub>3</sub> )	0	37	0.15	0.66
	Corner 4 (C <sub>4</sub> )	0	37	0.14	0.66
BS 1	50	37	0.13	0.69	
	150	37	0.12	0.70	
	200	37	0.13	0.71	
	300	37	0.13	0.71	
BS 2	50	37	0.15	0.72	
	150	37	0.25	0.72	
	200	37	0.20	0.73	
	300	37	0.19	0.73	
BS 3	50	37	0.14	0.74	
	150	37	0.09	0.73	
	200	32 *	0.10	0.74	
	300	37	0.10	0.74	

\*Significantly different (P > 0.05), all rotations are anti-clockwise

**Table 2. Lipid peroxidation, antioxidative systems and glucose residue in male rats exposed to low level electromagnetic fields**

Treatment	Lipid Peroxidation		Reduced Glutathione	Catalase	Glutathione reductase	Residual Glucose
	NADPH	Ascorbate				
Control	0.373 ± 0.04	0.300 ± 0.03	4.30 ± 0.19	0.209 ± 0.01	4.34 ± 0.07	0.209 ± 0.01
40 days	0.244 ± 0.01	0.255 ± 0.05	4.28 ± 0.17	0.068 ± 0.01	4.29 ± 0.00	0.091 ± 0.01
60 days	0.121 ± 0.05*	0.098 ± 0.020*	4.19 ± 0.02	0.055 ± 0.50*	4.27 ± 0.18	0.060 ± 0.12*

\*Significant (P < 0.05)

Errors indicate the standard error of the mean (SEM), N = 3

After 40 days of exposure, there were minor decreases in lipid peroxidations and other parameters except the activity of glutathione reductase which was less marked in comparison to control. At 60 days, the decrease activity of glutathione reductase was 11% of control, catalase activity decreased by 15% in comparison to control activity. The energy level showed a significant (P < 0.05) decreased when compared to the control.

After 60 days of exposure of rats to low intensities electromagnetic fields there were decreases in LPO compare to the control group (P < 0.05). **Figure 1** shows variations in lipid peroxidation, antioxidative stress and glucose residue. The respective decreases in NADPH dependent and ascorbate linked lipid peroxidation were 25% and 20% of the control groups. The ascorbic acid linked lipid peroxidation evidenced by malondialdehyde production was similar to that observed for NADPH-linked lipid peroxidation. The values obtained for NADPH-linked lipid peroxidation were higher than those for ascorbic acid lipid peroxidation.

## 10. Discussion

The present study shows that subchronic exposure to low intensities EMF induced oxidative stress in rat. More importantly, exposure duration further decreased in LPO and other antioxidative defense systems (**Table 2**). This indicates that prolonged exposure to non-thermal electromagnetic fields may induce several unspecific symptoms as reported by Abdel-Rassoul *et al.*, 2007 and Santini *et al.*, 2003 [16,25]. It is interesting to note that, in quantitative terms (% change) the duration of exposure to EMF on all antioxidative attributes was almost similar to control/sham. At 40 and 60 days of exposure, EMF decreased LPO, as well as enzymatic and non-enzymatic antioxidants. The significant decrease in temperature at point C<sub>3</sub> (200 m) from the base station was due to low elevation at water front. Some workers found a variety of self-reported health effects for people living within 1,000ft (325 m) of cell towers in rural areas; or within 300 ft (100m) of base stations in urban areas [6,16,26]. Long-term exposure may imply the development of oxidative stress that commensurate with the advancement of

idiopathic symptoms.

Erythrocytes are more vulnerable to LPO [27]. LPO has been shown to cause profound alterations in the structure and functions of the cell membrane, including decreased membrane fluidity, increased membrane-bound enzymes, and loss of essential fatty acids [28]. Several studies in animals and occupationally exposed human subjects indicate that exposure to electromagnetic fields induced mostly sleep disturbance, irritability, depression and headache among others [1,29,30]. The steady decrease in LPO in the present study (**Table 1**) may be attributed to induction of oxidative stress caused by exposure to EMF with diminution in enzymatic antioxidative defense mechanism.

Consistent with these results, reduction in enzymes activities is related to consumptions of enzymes in oxidative stress. Inhibition of GR leads to accumulation of the prooxidant GSSG by preventing reduction of GSSG to GSH, suggesting that the depletion of GSH might not have been compensated by GR. Thus, reduced supply of GSH could activate energy utilization, resulting in reduced glucose (**Figure 1**) [17]. Decreased activity of catalase implies that H<sub>2</sub>O<sub>2</sub> remains accumulated in the blood. It is known that O<sub>2</sub> can spontaneously be converted to H<sub>2</sub>O<sub>2</sub>, therefore, the oxidative stress caused by low intensity electromagnetic fields may be mediated by the conversion of accumulated H<sub>2</sub>O<sub>2</sub> to OH, which is the ultimate toxicant for conversion to form O<sub>2</sub> [31].

The present study of the environmental hazards from low energy EMF exposure demonstrates induction of oxidative stress in rat. Results of this study are associated with concomitant reduction in antioxidant defense systems. The relationship between the levels of exposure in the current study and the actual levels to which the general populations are exposed is relevant to public health. For this reason, the telecommunication industries could take advantage of the complexity of the biological and physical processes to standardize guidelines (exposure distance) to base stations in rural and urban areas. Regular assessment and early detection of antioxidative defense system among people working around the base stations are recommended.

## REFERENCES

- [1] W. R. Adey, "Tissue Interactions with Non-Ionizing Electromagnetic Fields," *Physiological Review* Vol. 61, No. 2, 1981, pp. 435-514.
- [2] N. Nikolaevich, A. Igoirevna and G. Vasil, "Influence of High-Frequency Electromagnetic Radiation at Non-Thermal Intensities on the Human Body," *No Place to Hide*, Vol. 3, No. 1, 2001, pp. 607-613
- [3] A. Balmori, "Possible Effects of Electromagnetic Fields from Phone Masts on a Population of White Stork," *Electromagnetic Biology and Medicine*, Vol. 24, No. 2, 2005, pp. 109-119.
- [4] R. Santini, P. Santini, P. Ruz, J. M. Danze and M. Seigne, "Survey Study of People Living in the Vicinity of Cellular Phone Base," *Journal of Electromagnetic Biology and Medicine*, Vol. 22, No. 1, 2002, pp. 41-49.
- [5] J. Schüz, E. Böhler, G. Berg, B. Schlehofer, I. Hettinger, K. Schlaefer, J. Wahrendorf, K. Kunna-Grass and M. Blettner, "Cellular Phones, Cordless Phones and the Risks of Glioma and Meningioma," (Interphone study Group, Germany). *American Journal of Epidemiology*, Vol. 163, No. 6, 2006, pp. 512-520.
- [6] A. Auvinen, K. G. Blaasaas, E. Cardis, H. C. Christensen, M. Feychting, S. J. Hepworth, C. Johansen, L. Klæboe, S. Lonn, P. A. McKinney, K. Muir, J. Ra-tanen, T. Salminen, J. Thomsen and T. Tynes, "Mobile Phone Use and Risk of Acoustic Neuroma; Results of the Interphone Case-Control Study in 5 North European Countries," *British Journal of Cancer* 3, Vol. 93, No. 7, 2005, pp. 842-848.
- [7] A. A. Marino, E. Nilsen and C. Frilot, "Non-Linear Changes in Brain Electrical Activity Due to Cell Phone Radiation," *Bioelectromagnetics*, Vol. 24, No. 5, 2003, pp. 339-346.
- [8] C. Daniells, I. Duce, D. Thomas, P. Sewell, J. Tattersall and D. De Pomerai, "Transgenic Nematodes as Biomonitoring of Microwave-Induced Stress," *Mutation Research*, Vol. 399, No. 1, 1998, pp. 55-64.
- [9] S. K. Dutta, B. Ghosh and C. F. Blackman, "Radiofrequency Radiation-Induced Calcium Ion Efflux Enhancement from Human and Other Neuroblastoma Cells in Culture," *Bioelectromagnetics*, Vol. 10, No. 2, 1989, pp. 197-202.
- [10] K. I. Obukhan, "The Effects of Ultrahigh-Frequency Radiation on Adaptation Thresholds and the Damages to Blood System Cells," *Lik Sprava*, Vol. 2, No. 7, 1998, pp. 71-73
- [11] S. Sarkar, S. Ali and J. Behari, "Effect of Low Power Microwave on the Mouse Genome: A Direct DNA Analysis," *Mutation Research*, Vol. 320, No. 1-2, 1994, pp. 141-147.
- [12] S. Lönn, A. Ahlbom, P. Hall and M. Feychting, "Long-Term Mobile Phone Use and Brain Tumor Risk," *American Journal of Epidemiology*, Vol. 161 No. 6, 2005, pp. 526-535.
- [13] T. E. Belousova and R. A. Karginat-Terent'eva, "Adrenergic Nerve Plexuses of Heart and Adrenal and Myocardial Catecholamines of Spontaneously Hypertensive Rats Under the Influence of Electro-Magnetic Irradiation in the Millimeter Range," *Morfologia*, Vol. 115, No. 1, 1999, pp. 16-18.
- [14] M. Petrides, "Exposure to Electromagnetic Fields by Using Cellular Telephones and its Influence on the Brain," *Neuro Report*, Vol. 11, No. 15, 2000, p. F15.
- [15] K. J. Fernie, D. M. Bird, R. D. Dawson and P. C. Lague, "Effects of Electromagnetic Fields on the Reproductive Success of American Kestrels," *Journal of Physiology, Biochemical and Zoology*, Vol. 73, No. 1, 2000, pp. 60-65.
- [16] G. Abdel-Rassoul, O. Abou EL-Fateh, M. Abou Salam, A. Michael, F. Farahat, M. EL-Batanouny and E. Salem, "Neurobehavioral Effects among Inhabitants around Mobile Phone Base Stations," *Neuro Toxicology*, Vol. 28, No. 2, 2007, pp. 434-440.
- [17] B. Tavazzi, D. Pierro, A. M. Amorini, et al, "Energy Metabolism and Lipid Peroxidation of Human Erythrocytes as a Function of Increased Oxidative Stress," *European Journal of Biochemistry*, Vol. 267, No. 3, 2000, pp. 684-689.
- [18] J. Everse and N. Hsia, "The Toxicities of Native and Modified Hemoglobins," *Free Radiological Biology and Medicine*, Vol. 22, No. 6, 1997, pp. 1075-1099.
- [19] M. Havas, "Dirty Electricity Elevates Blood Sugar among Electrically Sensitive Diabetics and May Explain Brittle Diabetes," *Electromagnetic Biology and Medicine*, Vol. 27, No. 2, 2008, pp. 135-146.
- [20] M. Younnes and C. P. Siegers, "Lipid Peroxidation as a Consequence of Glutathione Depletion in Rat and Mouse Liver," *Research of Common Chemical Pathology and Pharmacology*, Vol. 27, No. 1, 1980, pp. 119-128.
- [21] H. K. Prins and J. A. Loos "Glutathione," In: J. G. Yunis, Ed., *Biochemical Methods in Red Cell Genetics*, Academic Press, New York, 1969, pp. 127-129.
- [22] H. E. Aebi, "Catalase," In: H. U. Bergmeyer, J. Bergmeyer, and M. GraBL, Ed., *Methods of Enzymatic Analysis*, Verlag Chemie, Weinheim, 1983, pp. 273-286.
- [23] D. M. Goldberg and R. J. Spooner, "Glutathione Reductase," In: H. U. Bergmeyer, J. Bergmeyer and M. GraBL, Eds., *Methods of Enzymatic Analysis*, Verlag Chemie, Weinham, 1983, pp. 258-265.
- [24] N. A. Nelson, "Photometric Adaptation of Somogy Method for the Determination of Glucose," *Journal of Biological Chemistry*, Vol. 153, No. 1, 1944, pp. 375-380.
- [25] R. Santini, P. Santini, J. M. Danze, P. Le Ruz and M. Seigne, "Symptoms Experienced By People in Vicinity of Base Stations: II/Incidences of Age, Duration of Exposure, Location of Subjects in Relation to the Antennas and Other Electromagnet Factors," *Journal of Pathology and Biology*, Vol. 51, No. 7, 2003, pp. 412-415.
- [26] R. Santini, P. Santini, J. M. Danze, P. Le Ruz and M. Seigne, "Study of the Health of People Living in the Vicinity of Mobile Phone Base Stations: 1. Influence of Distance and Sex," *Journal of Pathology and Biology*, Vol. 50, No. 4, 2005, pp. 369-373.

- [27] J. Eritsland, "Safety Considerations of Polyunsaturated Fatty Acids," *American Journal of Clinical Nutrition*, Vol. 71, No. 1, 2000, pp. 1975-1980.
- [28] G. Van Ginkel and A. Sevanian, "Lipid Peroxidation-Induced Membrane Structural Alterations," *Methods Enzymol*, Vol. 233, No. 2, 1994, pp. 273-288.
- [29] G. Hyland, "Physics and Biology of Mobile Telephony," *Lancet*, Vol. 356, No. 12, 2005, pp. 1833-1836.
- [30] M. Rôdsli, M. Moser, Y. Baldinini, M. Meier and C. B. Fahrlander, "Symptoms of Ill Health Ascribed to Electromagnetic Field Exposure—A Questionnaire Survey International," *Journal of Hygiene and Environmental Health*, Vol. 207, No. 2, 2004, pp. 141-159.
- [31] Z. Gregus and C. D. Klaassen, "Mechanism of Toxicity," In: C. D. Klaassen, Ed., *Casarett and Doull's Toxicology: The Basic Science of Poisons*, McGraw-Hill, New York, 2001, pp. 35-81.

# Focal Region Field of a Two Dimensional Gregorian System Coated with Isotropic Chiral Medium

Tariq Rahim, Junaid Mughal, Mazhar Hussain

Faculty of Electronic Engineering, GIK Institute of Engineering Sciences and Technology, Topi, Swabi, N.W.F.P., Pakistan.  
Email: rahim372@gmail.com, junaid@giki.edu.pk, mazhar\_hussain@yahoo.com

Received March 3<sup>rd</sup>, 2010; revised May 5<sup>th</sup>, 2010; accepted May 10<sup>th</sup>, 2010.

## ABSTRACT

*Focal region field of a two dimensional Gregorian system coated with chiral medium is analyzed at high frequency. Maslov's method is used because the Geometrical Optics approximation fails at focal points. Maslov's method combines the simplicity of ray theory and the generality of Fourier transform. Fields patterns are calculated numerically and the results are plotted. The effects of thickness of chiral layer, chirality parameter of the chiral medium and permittivity of the medium are analyzed. The problem of simple dielectric layer is discussed as a special case of this problem.*

**Keywords:** Chiral Medium, Maslov's method, Gregorian System, Focal Region Field

## 1. Introduction

The knowledge of focal region field of focusing systems is useful for synthesizing feed arrays in imaging and design of multiple beam antennas in communication systems. The focusing of electromagnetic waves into material media is also a subject of considerable current interest due to applications in hyperthermia, microscopy, and optical data storage. Geometrical optics (GO) approximation is one of the well known method for evaluating high frequency field. It has been widely used to study various kinds of problems in different areas of electromagnetics, acoustics and seismology [1-3]. GO approximation for wave solution is important in electromagnetics because it provide insight into the behavior of wave front. GO is used only for high frequency approximation of a wave, provided the ray tube does not vanish. However, at caustic regions the ray tube shrinks to zero and GO show singularity at these regions. These regions are of great importance in all practical problems e.g. parabolic, paraboloidal and circular reflectors etc. To avoid these singularities Maslov proposed a method based on Maslov's theory [4,5]. Maslov's method has been used to find the field at caustic regions [6-20]. The idea in Maslov's method provides a systematic procedure for predicting the field in the caustic region by combining the simplicity of ray theory and generality of the transform method. High frequency field expressions has been

derived around feed point of a two dimensional Gregorian system using the Maslov's method in [19]. The same focussing system has been coated with isotropic and homogeneous chiral medium and field expressions are obtained. In Section 2 the plane wave reflection from a chiral slab backed by perfect electric conducting (PEC) plane is considered. In Section 3 high frequency expression for the field of a chiral coated Gregorian system excited by plane wave is derived. Numerical results and discussion are presented in Section 4 and the paper is concluded in Section 5.

## 2. Reflection of Plane Waves From a Chiral Slab Backed by Conductor

In this paper we want to find the reflected field around the focal region of a two dimensional Gregorian's main parabolic reflector coated with chiral medium. To achieve this the reflection of plane waves from a chiral slab backed by perfect electric conducting (PEC) plane is discussed as in [15,21]. As shown in **Figure 1** the region  $z \leq 0$  is occupied by free space defined by following equations

$$D = \epsilon_0 E$$

$$B = \mu_0 H$$

and the region  $0 \leq z \leq d$  is occupied by the chiral medium defined by Drude-Born-Fedorov (DBF) constitutive



The general form of the geometrical optics solution for the wave is given by [19]

$$E(r) = E_0 \left\{ \frac{D(\tau)}{D(0)} \right\}^{\frac{-1}{2}} \exp\{-jk_0(S_0 + \tau)\} \quad (7)$$

The Jacobian associated with the wave reflected by the parabolic reflector is given by [19]

$$J(\tau) = \frac{D(\tau)}{D(0)} = 1 - \frac{\cos^2 \alpha}{f} \tau \quad (8)$$

The Cartesian coordinates of the ray reflected by the hyperbolic surface is given by

$$x = \xi_2 + p_{x2}\tau = \xi_1 + p_{x1}\tau_1 + p_{x2}\tau \quad (9)$$

$$z = \zeta_2 + p_{z2}\tau = \zeta_1 + p_{z1}\tau_1 + p_{z2}\tau \quad (10)$$

where,  $\tau_1 = \sqrt{(\xi_1 - \xi_2)^2 + (\zeta_1 - \zeta_2)^2}$ . In the above equation  $(p_{x1}, p_{z1})$  and  $(p_{x2}, p_{z2})$  are the rectangular components of reflected wave vectors  $p_1^r$  and  $p_2^r$ , respectively. Now we consider the field after the reflection from the hyperbolic cylinder. The transformation from the Cartesian coordinates  $(x, z)$  to the ray coordinates  $(\xi_1, \tau)$  is given by [19]

$$D(\tau) = \frac{\cos^2 \alpha}{f} R_2 \left[ 1 - \frac{\tau}{R_1} \right] \quad (11)$$

Thus the geometrical ray expression of each component of the reflected wave is

$$E_x^r = -\cos(2\alpha - 2\psi) B_{\parallel} \left[ 1 - \frac{\tau}{R_1} \right]^{\frac{1}{2}} \exp[-jk(S_0 + \tau_1 + \tau)] \quad (12)$$

$$E_y^r = B_{\perp} \left[ 1 - \frac{\tau}{R_1} \right]^{\frac{1}{2}} \exp[-jk(S_0 + \tau_1 + \tau)] \quad (13)$$

$$E_z^r = -\sin(2\alpha - 2\psi) B_{\parallel} \left[ 1 - \frac{\tau}{R_1} \right]^{\frac{1}{2}} \exp[-jk(S_0 + \tau_1 + \tau)] \quad (14)$$

where,  $E_0^r$  is the amplitude of the incident wave at the reflection point on the parabolic surface and

$$S_0 = -\zeta_1 = 2f \frac{\cos 2\alpha}{1 + \cos 2\alpha} - c \quad (15)$$

$$\tau_1 = \sqrt{(\xi_2 - \xi_1)^2 + (\zeta_2 - \zeta_1)^2} \quad (16)$$

$$\tau = \sqrt{(x - \xi_2)^2 + (z - \zeta_2)^2} \quad (17)$$

As indicated by (7),  $E(r)$  will become infinite for

$\frac{D(\tau)}{D(0)} = 0$  i.e. at the caustic points. The expression

which is valid at the focal point according to Maslov's method is given by [19]

$$E(r) = \sqrt{\frac{k_0}{j2\pi}} \int_{-\infty}^{\infty} A_0(\xi) \left[ J(\tau) \frac{\partial p_z}{\partial z} \right] \times \exp\{-jk_0[S_0 + \tau - (x, p_z)p_z + zp_z]\} \quad (18)$$

The amplitude term  $\left[ J(\tau) \frac{\partial p_{z2}}{\partial z} \right]^{\frac{1}{2}}$  in the above equation is given by [19]

$$\left[ J(\tau) \frac{\partial p_{z2}}{\partial z} \right]^{\frac{1}{2}} = \frac{\sqrt{R_1}}{\sin(2\alpha - 2\psi)} \quad (19)$$

The phase function is given by

$$S = S_0 + \tau_1 + \tau - z(x, p_{z2})p_{z2} + p_{z2}z \quad (20)$$

where,  $S_0 + \tau_1$  is given by (15). The extra term is given by

$$\begin{aligned} S_{ex} &= \tau - z(x, p_{z2})p_{z2} + p_{z2}z \\ &= \tau - (\zeta_2 + p_{z2}\tau)p_{z2} + p_{z2}z \\ &= (p_{z2})^2 \tau + (z - \zeta_2)p_{z2} \\ &= p_{z2}(x - \xi_2) + (z - \zeta_2)p_{z2} \\ &= -\rho \cos(2\alpha - 2\psi - \phi) \\ &\quad + [\sin(2\alpha - 2\psi)\xi_2 + \cos(2\alpha - 2\psi)\zeta_2] \end{aligned}$$

We substitute (19)-(20) into (18) and taking  $A_0(\xi) = 1$ , we can find the finite field around the caustic as given below

$$E_x^r = \sqrt{\frac{k}{j2\pi}} \left[ \int_{A_1}^{A_2} + \int_{-A_2}^{-A_1} \right] \cos(2\alpha - 2\psi) B_{\parallel} \sqrt{R_1} \times \exp[-jk(S_0 + \tau_1 + S_{ex})] d(2\alpha) \quad (21)$$

$$E_y^r = \sqrt{\frac{k}{j2\pi}} \left[ \int_{A_1}^{A_2} + \int_{-A_2}^{-A_1} \right] B_{\perp} \sqrt{R_1} \times \exp[-jk(S_0 + \tau_1 + S_{ex})] d(2\alpha) \quad (22)$$

$$E_z^r = \sqrt{\frac{k}{j2\pi}} \left[ \int_{A_1}^{A_2} + \int_{-A_2}^{-A_1} \right] \sin(2\alpha - 2\psi) B_{\parallel} \sqrt{R_1} \times \exp[-jk(S_0 + \tau_1 + S_{ex})] d(2\alpha) \quad (23)$$

In the above equation,  $R_1$ ,  $S_0$ ,  $\tau_1$  and  $S_{ex}$  are expressed in terms of  $\alpha$  and  $A_1$  and  $A_2$  are the subtention angles  $2\alpha$  at the edges of the parabolic and hyperbolic surfaces. The limit of integration are calculated by the expression

$$A_1 = 2 \arctan\left(\frac{D}{2f}\right), A_2 = \arctan\left(\frac{L}{2c}\right)$$

### 4. Result and Discussion

Field pattern around the caustic region of a Gregorian system are determined using (21-23) by performing the integration numerically. The line plots of the field around the focal region located between the two reflectors, that point  $F_2$  in **Figure 2**. Simulation were done for  $A_1 = \pi/4.1$ ,  $A_2 = \pi/6.5$ ,  $k_0 = 1$ ,  $f = 100$ ,  $\mu = \mu_0$  and different values of  $\varepsilon = \varepsilon/\varepsilon_0$ ,  $d$ , and  $\beta$ . We have considered two types of polarization for incident wave. One is  $(A_x = 0, A_y = 1)$  and the other is  $(A_x = 1, A_y = 0)$ . The results are plotted in **Figures 3-20**. In all figures horizontal axis is  $z$ -axis and vertical axis corresponds to the absolute value of reflected field component. All plots are taken at  $x = 0$ . We have studied the effects of thickness of the the coated layer ( $d$ ), the chirality parameter ( $\beta$ ) and the relative permittivity of the me-

dium ( $\varepsilon$ ) on the focal region field. **Figures 3-5** show the effect of increase in the value of  $d$  keeping  $\beta = 0$  and  $\varepsilon = 3$ , that is ordinary dielectric case. We have shown in **Figure 3** and 5 the  $|E_x^r|$  and  $|E_z^r|$  for  $(A_x = 1, A_y = 0)$ . These figures show that increase in thickness of the coated layer ( $d$ ) results an increase in  $|E_x^r|$  and  $|E_z^r|$ . **Figure 4** shows the plot of  $|E_x^r|$  for  $(A_x = 0, A_y = 1)$ . This figure shows decrease in field strength as  $d$  increases. **Figures 6-11** show the effect of  $d$  while keeping  $\beta = 0.5$  and  $\varepsilon = 1$  for both types of polarization. **Figures 7** and **11** show increase in the field strength of  $|E_x^r|$  and  $|E_z^r|$  for  $(A_x = 1, A_y = 0)$ , respectively. **Figure 6** and **10** show the cross polarization effect due to chiral medium for polarization  $(A_x = 0, A_y = 1)$ , which also increases with increase in  $d$ . For  $d = 0$ , cross polarization effect vanishes and field strength increases with increase in  $d$ . **Figure 8** shows the plot of  $|E_y^r|$  for  $(A_x = 0, A_y = 1)$ , which decreases with increase in  $d$ , and **Figure 9**

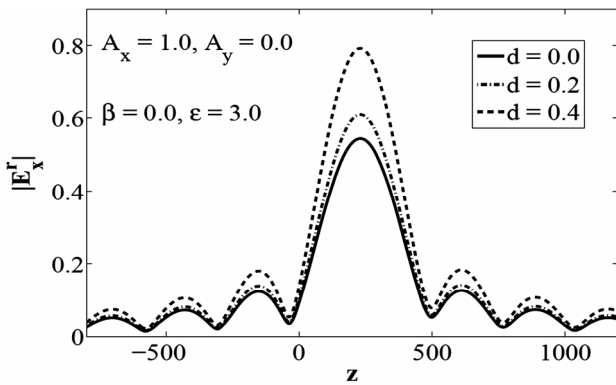


Figure 3. Plot of  $|E_x^r|$ , when parabolic reflector is coated with dielectric layer of varying thickness  $d$

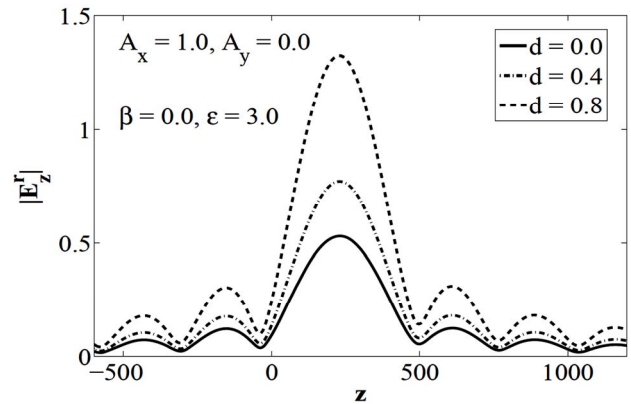


Figure 5. Plot of  $|E_z^r|$ , when parabolic reflector is coated with dielectric layer of varying thickness  $d$

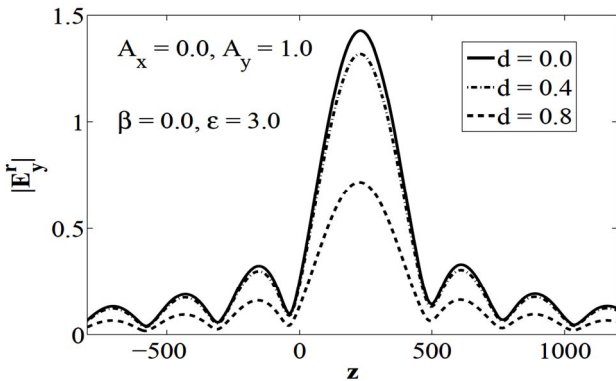


Figure 4. Plot of  $|E_x^r|$ , when parabolic reflector is coated with dielectric layer of varying thickness  $d$

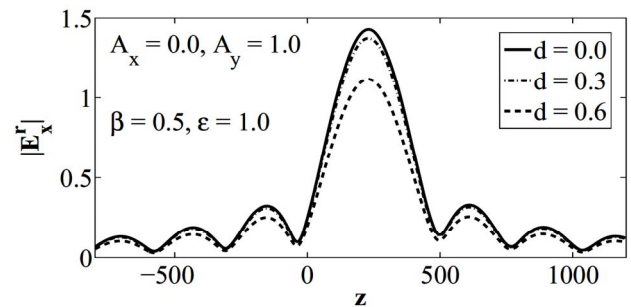


Figure 6. Plot of  $|E_x^r|$ , when the thickness of the coated layer  $d$  is varying. The impedance of chiral medium is equal to that of free space

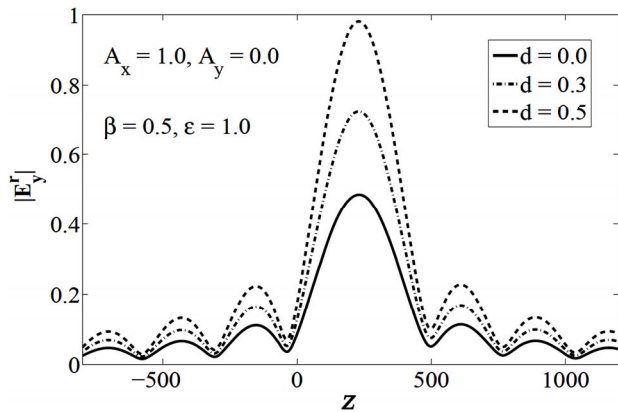


Figure 7. Plot of  $|E_x^r|$ , when the thickness of the coated layer  $d$  is varying. The impedance of chiral medium is equal to that of free space

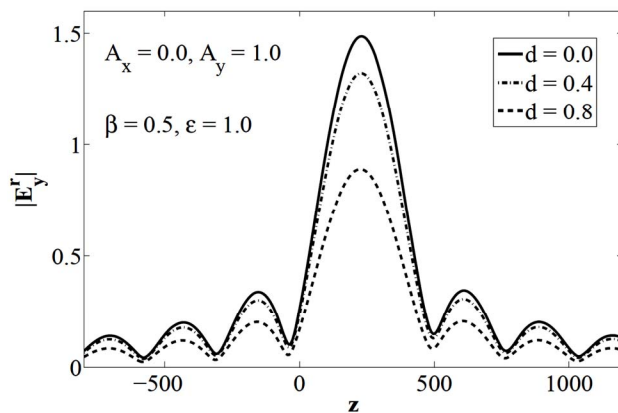


Figure 8. Plot of  $|E_y^r|$ , when the thickness of the coated layer  $d$  is varying. The impedance of chiral medium is equal to that of free space

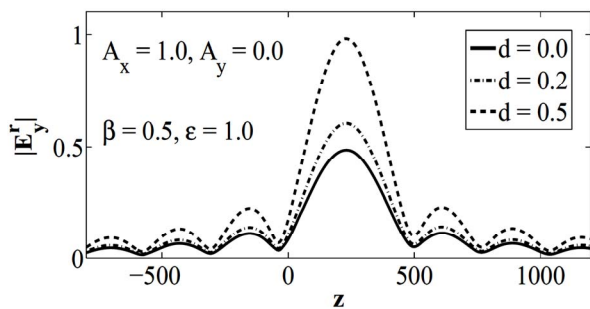


Figure 9. Plot of  $|E_y^r|$ , when the thickness of the coated layer  $d$  is varying. The impedance of chiral medium is equal to that of free space

shows the plot for  $(A_x = 1, A_y = 0)$ . This figure shows that cross polarization effect are zero for  $d = 0$ , but increases with increase in layer thickness  $d$ .

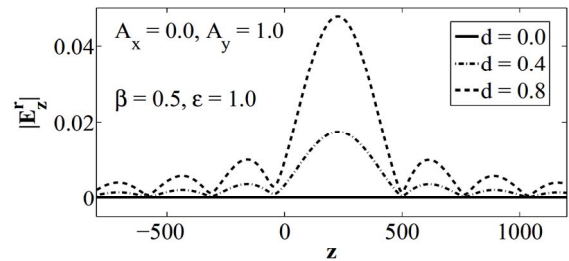


Figure 10. Plot of  $|E_z^r|$ , when the thickness of the coated layer  $d$  is varying. The impedance of chiral medium is equal to that of free space

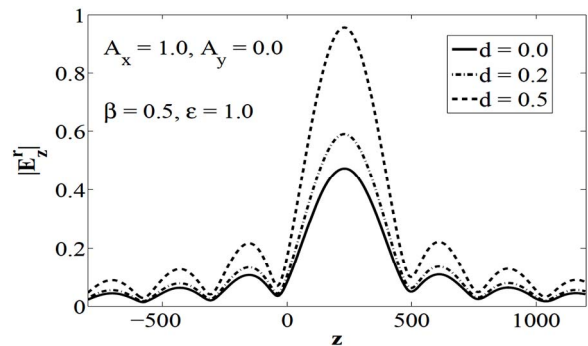


Figure 11. Plot of  $|E_z^r|$ , when the thickness of the coated layer  $d$  is varying. The impedance of chiral medium is equal to that of free space

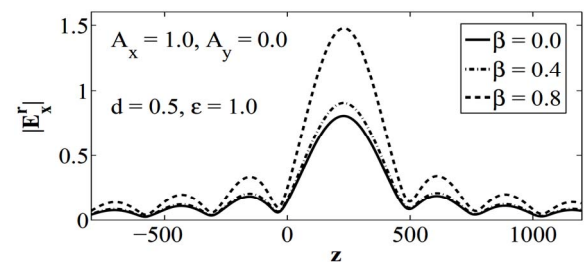


Figure 12. Plot of  $|E_x^r|$  showing the effect of chirality parameter  $\beta$ . The impedance of chiral medium is equal to that of free space

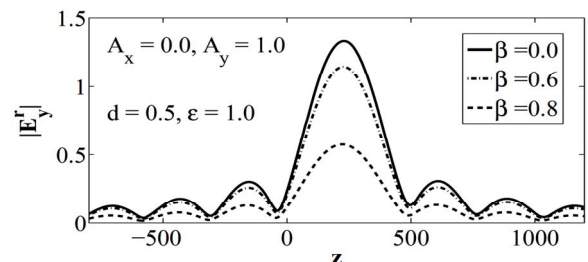


Figure 13. Plot of  $|E_y^r|$  showing the effect of chirality parameter  $\beta$ . The impedance of chiral medium is equal to that of free space

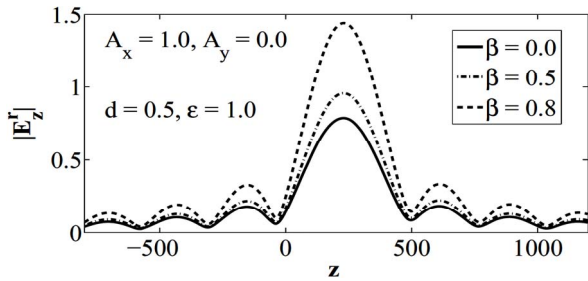


Figure 14. Plot of  $|E_z^r|$  showing the effect of chirality parameter  $\beta$ . The impedance of chiral medium is equal to that of free space

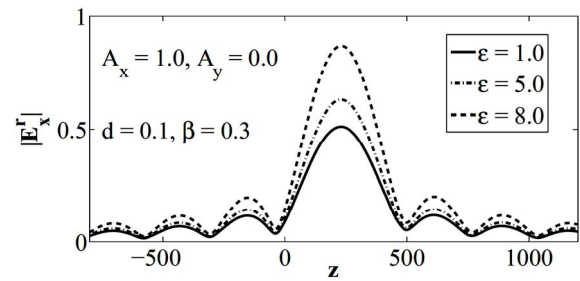


Figure 18. Plot of  $|E_x^r|$  showing the effect of relative permittivity  $\epsilon$  of chiral layer

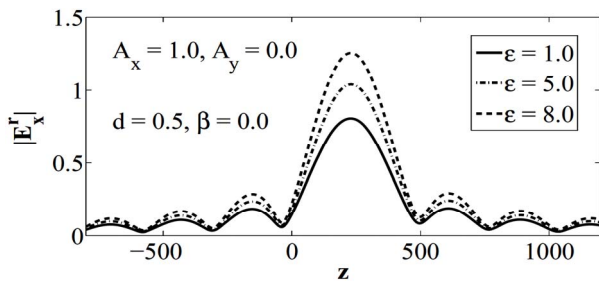


Figure 15. Plot of  $|E_x^r|$  showing the effect of relative permittivity  $\epsilon$  of dielectric layer

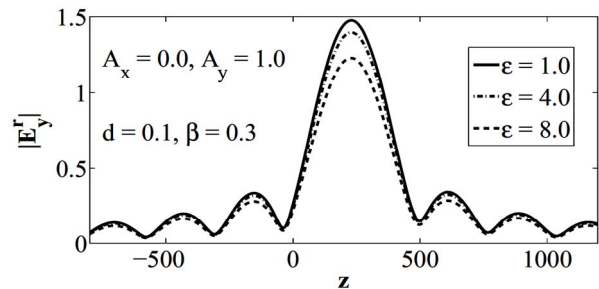


Figure 19. Plot of  $|E_y^r|$  showing the effect of relative permittivity  $\epsilon$  of chiral layer

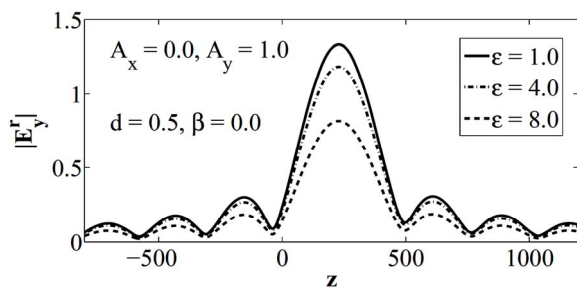


Figure 16. Plot of  $|E_y^r|$  showing the effect of relative permittivity  $\epsilon$  of dielectric layer

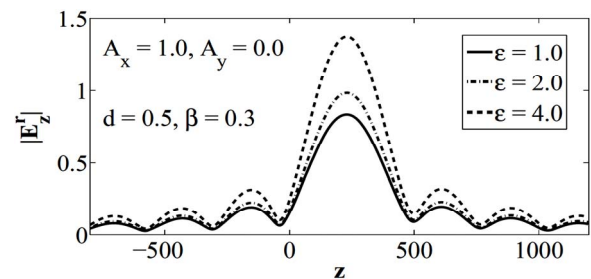


Figure 20. Plot of  $|E_z^r|$  showing the effect of relative permittivity  $\epsilon$  of chiral layer

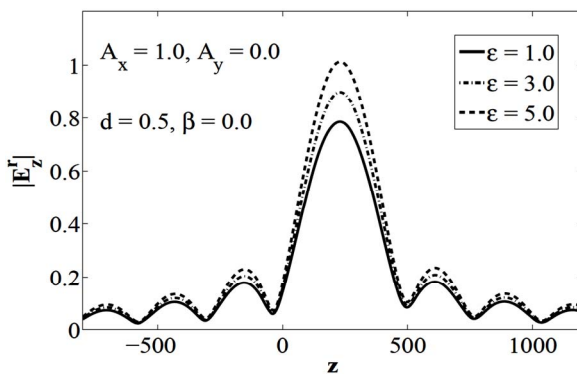


Figure 17. Plot of  $|E_z^r|$  showing the effect of relative permittivity  $\epsilon$  of dielectric layer

Figures 12 and 14 show the effect of chirality parameter  $\beta$  on field components while keeping  $\epsilon = 1$  and  $d = 0.5$ . Figures 12 and 14 show the plots of  $|E_x^r|$  and  $|E_z^r|$  for  $(A_x = 1, A_y = 0)$  respectively. These figures show that field strength increases with increase in chirality parameter  $\beta$ . Figure 13 shows that  $|E_y^r|$  decreases with increase in  $\beta$ . Cross polarization effects have not been shown because they have same trends as discussed above. Figures 15-17 show the effect of  $\epsilon$  while keeping  $d = 0.5$  and  $\beta = 0$ , that is for ordinary dielectric case. Figures 15 and 17 show the plot of  $|E_x^r|$  and  $|E_z^r|$  for polarization  $(A_x = 1, A_y = 0)$  respectively and show the increase in the field strength if

we increase the relative permittivity of dielectric medium coated on the surface of reflector. **Figure 16** shows that  $|E_y^r|$  decreases with increase in  $\epsilon$  for polarization ( $A_x = 0, A_y = 1$ ). **Figures 18-20**, which are for chiral coating, show the same trends as in **Figures 15-17**.

## 5. Conclusions

Focal region fields of a two dimensional Gregorian reflector is analyzed using GO and Maslov's method. Two types of polarization are discussed. The reflected field components are analyzed numerically and the results are given in the focal plane. It is concluded that increase in chirality parameter ( $\beta$ ), increase in thickness ( $d$ ) and relative permittivity ( $\epsilon$ ), results in increase in of  $|E_x^r|$  and  $|E_z^r|$  for ( $A_x = 1, A_y = 0$ ). While  $|E_y^r|$  decreases for ( $A_x = 0, A_y = 1$ ). Cross polarized fields exist when  $k\beta \neq 0$  and increase with increase in value of  $d$ .

## REFERENCES

- [1] Y. A. Kravtsov and Y. I. Orlov, "Caustics, Catastrophes, and Wave Fields," Springer Verlag, Berlin, 1993.
- [2] G. A. Dechamps, "Ray Techniques in Electromagnetics," *Proceedings of IEEE*, 1972, pp. 1022-1035.
- [3] C. H. Chapman and R. Drummond, "Body Wave Seismograms in Inhomogeneous Media Using Maslov Asymptotic Theory," *Bulletin of the Seismological Society of America*, Vol. 72, No. 68, 1982, pp. 277-317.
- [4] V. P. Maslov, "Perturbation Theory and Asymptotic Methods," *Moskov., Gos., University, Moscow*, 1965 (in Russian). (Translated into Japanese by Ouchi *et al.*, Iwanami).
- [5] V. P. Maslov and V. E. Nazaikinski, "Asymptotic of Operator and Pseudo-Differential Equations," Consultants Bureau, New York, 1988.
- [6] A. Ghaffar, Q. A. Naqvi and K. Hongo, "Analysis of the Fields in Three Dimensional Cassegrain System," *Progress in Electromagnetics Research*, Vol. 72, 2007, pp. 215-240.
- [7] A. Hussain, Q. A. Naqvi and K. Hongo, "Radiation Characteristics of the Wood Lens Using Maslov's Method," *Progress in Electromagnetics Research*, Vol. 73, 2007, pp. 107-129.
- [8] Y. Ji and K. Hongo, "Analysis of Electromagnetic Waves Refracted by a Spherical Dielectric Interface Method," *Journal of the Optical Society of America*, Vol. 8, No. 3, 1991, pp. 541-548.
- [9] Y. Ji and K. Hongo, "Field in the Focal Region of a Dielectric Spherical by Maslov's Method," *Optical Society of America*. Vol. 8, No. 11, 1991. pp. 1721-1728.
- [10] K. Hongo, Y. Ji and E. Nakajima, "High Frequency Expression for the Field in the Caustic Region of a Reflector Using Maslov's Method," *Radio Science*, Vol. 21, No. 6, 1986, pp. 911-919.
- [11] K. Hongo and Y. Ji, "High Frequency Expression for the Field in the Caustic Region of a Cylindrical Reflector Using Maslov's Method," *Radio Science*, Vol. 22, No. 3, 1987, pp. 357-366.
- [12] K. Hongo and Y. Ji, "Study of the Field Around the Focal Region of Spherical Reflector Antenna by Maslov's Method," *IEEE Transaction Antennas Propagat*, Vol. 36, No. 5, 1988, pp. 592-598.
- [13] R. W. Ziolkowski and G. A. Deschamps, "Asymptotic Evaluation of High Frequency Field near a Caustic: An Introduction to Maslov's Method," *Radio Science*, Vol. 19, No. 4, 1984, pp. 1001-1025.
- [14] M. Faryad and Q. A. Naqvi, "High Frequency Expression for the Field in the Caustic Region of Cylindrical Reflector Placed in Chiral Medium," *Progress in Electromagnetics Research*, Vol. 76, 2007, pp. 153-182.
- [15] Faryad, M. and Q. A. Naqvi, "High Frequency Expression for the Field in the Caustic Region of a Parabolic Reflector Coated with Isotropic Chiral Medium," *Journal of Electromagnetic Waves and Application*, Vol. 22, 2008, pp. 965-986.
- [16] M. Faryad and Q. A. Naqvi, "Cylindrical Reflector in Chiral Medium Supporting Simultaneously Positive Phase Velocity and Negative Phase Velocity," *Journal of Electromagnetic Waves and Applications*, Vol. 22, No. 2, 2008, pp. 563-572.
- [17] A. Ghaffar, A. Hussain, Q. A. Naqvi and K. Hongo, "Radiation Characteristics of an Inhomogeneous Slab Using Maslov's Method," *Journal of Electromagnetic Waves and Applications*, Vol. 22, No. 2, 2008, pp. 301-312.
- [18] A. Aziz, A. Ghaffar, Q. A. Naqvi and K. Hongo, "Analysis of the Fields in Two Dimensional Gregorian System," *Journal of Electromagnetic Waves and Applications*, Vol. 22, No. 1, 2008, pp. 85-97.
- [19] A. Aziz, Q. A. Naqvi and K. Hongo, "Analysis of the Fields in Two Dimensional Cassegrain System," *Progress in Electromagnetics Research*, Vol. 71, 2007, pp. 227-241.
- [20] A. Ghaffar, A. Rizvi and Q. A. Naqvi, "Field in the Focal Space of Symmetrical Hyperboloidal Focusing Lens," *Progress in Electromagnetics Research*, Vol. 89, 2009, pp. 255-273.
- [21] A. Lakhtakia, "Beltrami Fields in Chiral Media," World Scientific Series in Contemporary Chemical Physics, 1994.
- [22] S. Bassiri, "Electromagnetic Waves in Chiral Media," *Recent Advances in Electromagnetic Theory*, H. N. Kritikos and D. L. Jaggard, Eds., Springer-Verlag, New York, 1990.
- [23] V. Tuz and V. Kazanskiy, "Periodicity Defect Influence on the Electromagnetic Properties of a Sequence with Bi-Isotropic Layers," *Progress in Electromagnetics Research B*, Vol. 7, 2008, pp. 299-307.

# New Consideration of Problems of Gravitational Optics and Dark Matter Based on Crystal Model of Vacuum

Evgeny V. Chensky

Modern Science Institute, SAIBR, Moscow, Russia.  
Email: [echensky@yandex.ru](mailto:echensky@yandex.ru)

Received March 25<sup>th</sup>, 2010; revised July 19<sup>th</sup>, 2010; accepted July 26<sup>th</sup>, 2010.

## ABSTRACT

*In presented paper we try to consider problems of the gravitational optics and dark matter developing from the crystal model for the vacuum. How it is follows from consideration it enables to describe both electromagnetic waves and spectrum of elementary particles from the unified point of view. Two order parameters – a polar vector and an axial vector - had to be introduced as electrical and magnetic polarization, correspondingly, in order to describe dynamic properties of vacuum. Vacuum susceptibility has been determined to be equal to the fine structure constant  $\alpha$ . Unified interaction constant  $g$  for all particles equal to the double charge of Dirac monopole has been found ( $g = e/\alpha$ , where  $e$  charge electron). The fundamental vacuum constants are:  $g$ ,  $\alpha$ , parameters of length  $\xi_e, \xi_n$  and parameters of time  $\tau_e, \tau_n$  for electron and nucleon oscillations, correspondingly. Energy of elementary particles has been expressed in terms of the fundamental vacuum parameters, light velocity being equal to  $c = \xi_e / \tau_e = \xi_n / \tau_n$ . The term mass of particle has been shown to have no independent meaning. Particle energy does have physical sense as wave packet energy related to vacuum excitation. Exact equation for particle movement in the gravitational field has been derived, the equation being applied to any relatively compact object: planet, satellite, electron, proton, photon and neutrino. The situation has been examined according to the cosmological principle when galaxies are distributed around an infinite space. In this case the recession of galaxies is impossible, so the red shift of far galaxies' radiation has to be interpreted as the blue time shift of atomic spectra; it follows that zero-energy, and consequently electron mass are being increased at the time. Since physical vacuum has been existed eternally, vacuum parameters can be either constant, or oscillating with time. It is the time oscillation of the parameters that leads to the growth of electron mass within the last 15 billion years and that is displayed in the red shift; the proton mass being decreased that is displayed in planet radiation.*

**Keywords:** Space Electromagnetism, Electromagnetism and Particles Physics, Universe Evolution Modeling

## 1. Introduction

The science about cosmology has been in rather difficult situation in recent years. On one hand, observations of star dynamics in galaxies and of galaxies in clusters show substantial deviation of rotation velocities from Kepler's law; this proves the existence of additional matter (dark matter) which participates in gravitational interaction [1-3]. On the other hand, more careful examination of the red shift in the nearer space at the distances of  $10^5$ - $10^7$  light years as well as observation of supernova outburst [4,5] show that velocity of the Universe expansion increases with time, and this in turn requires introduction of additional dark energy with anti-gravitational properties.

Thus, a contradiction arises. Practically, in one and the same point it is necessary to introduce both dark matter creating additional gravitational field and dark energy having anti-gravitation. Since there is no doubt about the facts above, their interpretation must be revised.

At the present time there are two mutually exclusive points of view. First, despite very distinctive spatial non-homogeneity of matter, observations show that at the distances of about  $10^9$  light years (cell of homogeneity) matter is distributed in the space quite homogeneously. Besides, the cosmological principle suggests that these homogeneous cells should cover the entire infinite space. Second, the red shift discovered by Hubble, which he interpreted as Doppler's principle related to the galaxies

expansion, made Friedman's model of expanding Universe quite necessary. From Hubble's empirical law that determines dependence of velocity of galaxies on the distance  $v = Hr$ , we can suppose existence of a singularity at a certain time. Since velocity of expansion of the galaxies cannot exceed the light velocity  $c$ , it follows from the relation  $c = HR = HcT_0$ , that there is quite a definite size of the Universe growing with time  $R = cT_0$ , here  $-T_0$  is the singularity offset counted from the present moment; Hubble's constant equal to  $H = 1/T_0$  decreases with time; however, observations show, that the value  $H$ , on the contrary, increases with time.

If we interpret the existence of a singularity as a Big Bang, we have to bear in mind that the explosion is a phase transition from a metastable state into another more stable state accompanied with release of energy. Before the phase transition, this energy is homogeneously distributed around the space. They sometimes say: explosion power is equivalent to e.g. one kilogram of trotyl; it is obvious that two kilograms of trotyl give off right twice as much energy as one kilogram does. Besides, the phase transition does not begin with the singularity but with the nucleation of a new phase whose size exceeds the critical radius. In this case energy is released in accordance with broadening the new phase at the expense of the phase edge motion. Since the average energy density of the entire matter in vacuum is approximately  $0.008 \text{ erg/m}^3$ , this very energy should be released at the phase transition of each cubic meter of vacuum. It is difficult to imagine, however, that electrons and protons could be created out of this homogeneously distributed in space energy, and, besides, in exactly equal quantities. An explosion of a hydrogen bomb in vacuum can serve as a model of a hot Universe. The hydrogen bomb is a local object in a metastable state. There is a mixture of light and heavy nuclei under the temperature of several million degrees at the moment of detonation. According to D'Alambert equation, the electromagnetic pulse and the neutrino pulse will start to disperse with the light velocity. Following electromagnetic pulse relativistic electrons will fly and then light, and heavy nuclei. In a second, the electromagnetic pulse will reach the Moon area and nothing will stay at the point of explosion. Thus, the examined case is also far from the Friedman's model of expanding Universe.

In order to somehow reconcile the model of the infinite matter distribution in space with that of the expanding Universe, Milne offered the following reasoning [6]. If we mentally specify a sphere of a definite size in a matter homogeneously distributed around an infinite space, then external layers of the sphere due to their spherical symmetry have no influence on the sphere dynamics. Therefore, we can ignore the external layers and consider the Universe as a sphere of a definite size that precisely coincides with the Friedman's model. However, this

statement is a mistake. The thing is that with matter being homogeneously distributed about the entire infinite space, the gravitational potential follows the condition of the translational invariance:  $U(\vec{r}) = \text{const}$ . We may consider this constant to be equal to zero, therefore, a gravitational potential only arises at deviation of a matter distribution from an average value. For that reason the equation for the potential can be written as follows:

$$\Delta U(\vec{r}) = 4\pi\gamma(\rho(\vec{r}) - \rho_0). \quad (1)$$

Here  $\rho_0$  is an average density of matter. From equation (1) we can see that it is not necessary to search for dark energy as the density is both the gravitating and the anti-gravitating matter in the form of  $\rho(\vec{r})$  and  $\rho_0$ .

On the other hand, if we mentally specify a sphere of radius  $R$  with the density of matter  $\rho_0$  and ignore the external matter, we come to another equation for the potential:

$$\Delta U(\vec{r}) = 4\pi\gamma \begin{cases} \rho_0, & r < R; \\ 0, & r > R. \end{cases}$$

This equation has the following solutions:

$$U(r) = -2\pi\gamma\rho_0 R^2 \left(1 - \frac{r^2}{3R^2}\right), \quad r < R; \quad (2)$$

$$U(r) = -\frac{4\pi\gamma\rho_0 R^3}{3r}, \quad r > R;$$

Similar expressions can be used for determining gravitational potentials of planets, stars and galaxies in a form of the sum of the potentials of stars with their specific location. However, for the scales comparable with the size of homogeneity cell and bigger, we come to an obviously non-physical result: the potential in any arbitrary point depends on the radius of a sphere which we mentally specify out of the entire infinite space. Thus, any result depending on the mentally specified radius of the sphere, including the radius of the visible part of the Universe, is physically incorrect.

For instance, we can determine the circular orbital velocity  $v_1$  for the Universe of radius  $R$  on the sphere surface from the equality of centripetal and centrifugal forces:

$$R^2 = \frac{\partial U(r)}{\partial r} \Big|_{r=R} = \frac{4\pi\gamma\rho_0 R}{3}; \quad v_1 = R\dot{\varphi} = R\sqrt{\frac{4\pi\gamma\rho_0}{3}}$$

If  $v_1$  is equal to the light velocity  $c$ , we obtain the following expression for the critical matter density in the Universe:

$$\rho_c = \frac{3c^2}{4\pi\gamma R^2} = \frac{3H^2}{4\pi\gamma}.$$

This corresponds to the condition  $R = r_g$  when  $r_g$  is a gravitational radius. Therefore, with the definite choice

for  $R$  we may come to the conclusion that the Universe is a black hole, while, as it follows from the cosmological principle at the scales comparable with the radius of the visible part of the Universe, the gravitational potential has no specific features and its average value is zero.

The same situation takes place when we consider the influence of a pressure on the dynamics of the expanding Universe. For instance, if we take a big vessel with a gas, mentally specify a sphere of radius  $R$  in it, and ignore the gas surrounding the sphere, we can state that the gas will broaden and get cool at the expense of the internal pressure. This may remind the model of the expanding Universe. Remember, however, that the specified sphere is surrounded with the same gas at the same pressure; that is why there will be neither broadening nor cooling. Thus, for the infinite Universe both an average gravitational potential and an average pressure are constant; besides, since the expanding dynamics is influenced by the equal to zero gradients of these variables, there cannot be neither expanding nor compression. An infinite system can only stratify according to the energy density and we really observe this stratification on giant scales from the value less than  $10^{-9}$  erg/cm<sup>3</sup> for an inter-galaxy space to the value over  $10^{39}$  erg/cm<sup>3</sup> for nuclear energy.

Nevertheless, within the frames of the cosmological principle there is a problem, the so called photometric paradox. The thing is that at present time when stars and galaxies radiate light in the entire infinite space, we can introduce an average luminosity  $L$  of a unit volume, provided that the densities of a luminous flux intensity at the distance  $r$  from a single volume is equal to  $j = L/4\pi r^2$ . The integral over the sphere of radius  $R$  gives the total flux intensity equal to  $J = RL$ ; it follows that with  $R$  approaching infinity the flux intensity must approach infinity as well. Practically, however, we see rather a low sky luminosity. This is the photometric paradox.

In fact, by calculating the intensity, we must take into consideration the retardation effects. The flux that comes to a certain point ( $r = 0$ ) at a certain time ( $t = 0$ ) radiates at different moments depending on the distance:

$$J = \int j \left( t = -\frac{r}{c} \right) d\vec{r} = c \int_{-\infty}^0 L(t) dt \quad (3)$$

Expression (3) shows that the flux coming from the deep Universe will be finite if  $L(t)$  at longer  $t$  decreases faster than  $1/t$ .

Besides, we can divide the entire flux observed at any point of the infinite space into two parts: the flux  $J_{vis}$  of a visible part of space  $R = cT_0$ ,  $T_0 \sim 15 \cdot 10^9$  years and the relict flux  $J_{rel}$  radiating from the spots with  $r > R$ :

$$J = J_{vis} + J_{rel} = \sum_{n=1}^N J_n + \int_{-\infty}^{-T_0} L(t') dt'$$

Here summing was carried out over a countable num-

ber of galaxies in the visible part of the Universe. Thus, from the expressions given above it follows that the Universe must be non-stationary, not due to an expansion of galaxies', but at the expense of a variation of physical vacuum parameters. Since the relict radiation corresponds to the temperature  $3^0\text{K}$ , the Universe had such a temperature long ago. The one but not the only feature of a non-stationarity is the red shift of atomic spectra that we can interpret as the blue temporal shift of both characteristic Bohr energy and all atomic energy levels correspondingly, at the expense of variation of physical vacuum parameters. Observations show that the characteristic Bohr frequency depends on time and increases with time. By introducing a frequency of an arbitrary atomic level, we obtain the following expression for the Hubble's constant:

$$\frac{d}{dt} \left( \frac{\omega(t)}{\omega(t=0)} \right) = H(t) \quad (4)$$

Both  $\omega(t)$  and  $H(t)$  are monotonously increasing functions. The latest observations of the flashes of far supernova [4-5] show temporal growth of  $H$ . It is senseless to explain this situation using space-time properties.

Speaking about space-time properties is quite the same as judging about wine quality by the curvature of a bottle surface. Dilettantes are often attracted by the appearance of the vessel, while connoisseurs pay attention to its contents, conservation conditions, and temporal changes. We should regard space like a vessel with the only feature: its volume is infinite. Its internal properties are to be discussed.

## 2. Hidden Parameters of Vacuum

We should proceed from the experimental fact that the energy and the pulse of any elementary particle are:

$$\varepsilon_k = \hbar\omega_k; \vec{p} = \hbar\vec{k} \quad (5)$$

Here  $\omega_k$ -frequency for electron, proton, photon and neutrino, correspondingly, we expressed as follows:

$$\omega_{ek} = \sqrt{\omega_{e0}^2 + c^2 k^2}; \omega_{pk} = \sqrt{\omega_{p0}^2 + c^2 k^2}; \omega_{r,v;k} = ck \quad (6)$$

The unified formula for the energy of any elementary particle points to the existence of the universal interaction for fields related to each particle. Besides, the two oscillation branches with the energy gap observed in the excitation spectrum prove an existence of a certain set of discrete oscillators whose interaction causes normal oscillations with frequencies  $\omega_k$ . In fact, we can represent vacuum as a crystal object of a cubic or hexagonal symmetry with a very small lattice period, much less than  $10^{-26}$  cm. We can estimate the upper limit of a lattice period by the maximum particle energy in cosmic rays equal to  $10^{21}$  eV that corresponds to the wave vector of  $10^{26}$  cm<sup>-1</sup>. The vacuum ground state is the equilibrium

position of all oscillators; these are the points of equilibrium forming crystal lattice related to the absolute coordinate system. Under the deviation of an oscillator from the equilibrium position, a dipole moment arises. For the scales exceeding the lattice period we can introduce a macroscopic order parameter as an electric polarization of vacuum:

$$\vec{P}(\vec{r}) = \frac{4\pi}{\delta V} \sum_i \vec{d}_i .$$

Suppose, there are two branches of normal oscillations of field  $\vec{P}$  that we can call electron and nucleon modes. The Hamiltonian for electron and nucleon modes written in the unified form, is:

$$H = \frac{1}{8\pi} \int \left( \tau_{e,n}^2 \vec{P}^2 + \xi_{e,n}^2 (\nabla \vec{P})^2 + \sigma \vec{P}^2 \right) d\vec{r} \quad (7)$$

For electronic and nucleonic parts, we introduced the parameters of time  $\tau_e, \tau_n$  and length  $\xi_e, \xi_n$  that characterize the kinetic and gradient energy of the fields. Besides, we introduced a dimensionless parameter of an elastic coefficient  $\sigma$  corresponding to the reciprocal susceptibility common to both modes. These are the latent parameters of vacuum and the available experimental data are sufficient to determine them.

By using the minimal action principle for the Lagrange function equal to the difference of the kinetic energy - the first member of expression (7), and the potential energy—the second and the third members of (7), we obtain the equation of motion for six independent normal oscillations  $P_{ex}, P_{ey}, P_{ez}, P_{nx}, P_{ny}, P_{nz}$ :

$$\left( \sigma + \xi_{e,n}^2 \left( \frac{\partial^2}{\partial x^2} + \frac{\partial^2}{\partial y^2} + \frac{\partial^2}{\partial z^2} \right) - \tau_{e,n}^2 \frac{\partial^2}{\partial t^2} \right) P_{e,n,x,z} = 0 \quad (8)$$

By setting up the following solutions:

$$P_{x,y,z} = a_{x,y,z} \exp\left(i(\vec{k}\vec{r} + \omega t)\right), \quad (9)$$

we obtain the spectrum for normal oscillations:

$$\begin{aligned} \omega_{e,n,k} &= \pm \sqrt{\omega_{e,n,0}^2 + c^2 k^2}; \quad \omega_{e,0} = \frac{\sqrt{\sigma}}{\tau_e}; \\ \omega_{n,0} &= \frac{\sqrt{\sigma}}{\tau_n}; \quad c = \frac{\xi_e}{\tau_e} = \frac{\xi_n}{\tau_n} \end{aligned} \quad (10)$$

Therefore, we can represent physical vacuum as some coherent state with the natural frequency standards in the form of homogeneous polarization oscillations about an absolute coordinate system

$$P_{e,n;x,y,z}(\vec{r}, t) = a_{e,n;x,y,z} \exp(i\omega_{e,n,0} t)$$

with the absolute time, homogeneous around the entire space  $t(\vec{r}) \equiv t_{abs}$ .

The situation, however, becomes more complicated, since the electrical vacuum polarization generates the following electric charge:

$$\text{div} \vec{P} = -4\pi \rho_e . \quad (11)$$

Here  $\rho_e$  is the electric charge density, while the polarization is determined by both electron and nucleon modes  $\vec{P} = \vec{P}_e + \vec{P}_n$ . This results in an additional long-range Coulomb interaction between the normal oscillations  $P_{ex}, P_{ey}, P_{ez}, P_{nx}, P_{ny}, P_{nz}$

$$U = \frac{1}{2} \iint \frac{\rho_e(\vec{r}) \rho_e(\vec{r}')}{|\vec{r} - \vec{r}'|} d\vec{r} d\vec{r}' \quad (12)$$

For simplicity, we consider normal oscillations inside the electronic modes. We dimensionlize coordinates and time. We express new variables like this:  $t \Rightarrow t/\tau_e$ ;  $r \Rightarrow r/\xi_e$ ; velocity being in terms of  $c = \xi_e/\tau_e$ . It makes sense to specify a dimensional value for the electric polarization in the terms of the electron charge:

$$\vec{P} \Rightarrow \frac{e}{\xi_e^2} \vec{P} ,$$

after that the electron field action reduces to form:

$$S = \frac{e^2}{8\pi c} \int dt \int d\vec{r} \left\{ \dot{P}_i \dot{P}_i - \frac{\partial P_i}{\partial x_j} \frac{\partial P_i}{\partial x_j} - \sigma P_i P_i - \frac{1}{4\pi} \int \frac{\frac{\partial P_i(\vec{r}, t)}{\partial x_i} \frac{\partial P_j(\vec{r}', t)}{\partial x'_j}}{|\vec{r} - \vec{r}'|} d\vec{r}' \right\} \quad (13)$$

Here  $i$  and  $j$  run over  $x, y, z$  and we carried out summation over repeated indices. By varying action  $S$  over the values  $P_i, \dot{P}_i, \partial P_i / \partial x_j$ , we come to the following system of the integral-differential equations:

$$\left( \frac{\partial^2}{\partial t^2} - \Delta + \sigma \right) P_i(\vec{r}, t) + \frac{1}{4\pi} \int \frac{(x_i - x'_i)}{|\vec{r} - \vec{r}'|^3} \frac{\partial P_j(\vec{r}')}{\partial x'_j} d\vec{r}' = 0 \quad (14)$$

Consider the solutions in the form of plane waves:

$$P_i(\vec{r}, t) = P_i \exp\left(i(\vec{k}\vec{r} + \omega t)\right) \quad (15)$$

For plane waves, Equation (14) reduce to the form:

$$\left( \sigma + k^2 - \omega^2 \right) P_i + \frac{k_i k_j}{k^2} P_j = 0 \quad (16)$$

By making the determinant of the Equation (16) equal to zero, we obtain the oscillation spectrum:

$$\begin{vmatrix} \left(\sigma + k^2 + \frac{k_x^2}{k^2} - \omega^2\right) & \frac{k_x k_y}{k^2} & \frac{k_x k_z}{k^2} \\ \frac{k_x k_y}{k^2} & \left(\sigma + k^2 + \frac{k_y^2}{k^2} - \omega^2\right) & \frac{k_y k_z}{k^2} \\ \frac{k_x k_z}{k^2} & \frac{k_y k_z}{k^2} & \left(\sigma + k^2 + \frac{k_z^2}{k^2} - \omega^2\right) \end{vmatrix} = 0 \tag{17}$$

Equation (17) transforms to

$$(\sigma + k^2 - \omega^2)^2 \cdot (\sigma + 1 + k^2 - \omega^2) = 0 \tag{18}$$

Thus, from (18) we obtain the normal spectrum of the oscillations; from Equation (16), we obtain the form of the oscillations:

$$\begin{aligned} \omega_k &= \pm\sqrt{\sigma + 1 + k^2}; \\ k_y P_x &= k_x P_y; \quad k_z P_x = k_x P_z, \quad k_z P_y = k_y P_z; \\ \omega_k &= \pm\sqrt{\sigma + k^2}; \\ k_x P_x + k_y P_y + k_z P_z &= 0. \end{aligned} \tag{19}$$

Expressions (19) allow the definition of the general properties of the normal oscillations for vacuum fields linked by the long-range Coulomb interaction. The Laplacian operator in Equation (14) requires that the polarization components be eigenfunctions of this operator:

$$\Delta P_i = \beta^2 P_i \tag{20}$$

The result of the Coulomb interaction is that the oscillations of the polarization are divided into two classes: longitudinal  $\vec{P}_1$  with  $rot\vec{P}_1 = 0$  and lateral  $\vec{P}_2$  with  $div\vec{P}_2 = 0$ , according to the Helmholtz theorem  $\vec{P}_1 = \nabla\Phi$ ;  $\vec{P}_2 = rot\vec{A}$ , here  $\Phi$  and  $\vec{A}$  are scalar and vector potentials. Longitudinal oscillations provide a depolarizing electric field  $\vec{E} = -\vec{P}_1$ , which meets the following condition:

$$div\vec{E} = 4\pi\rho_e.$$

For lateral (transverse!) oscillations, the depolarizing field equals to zero. As a result, the frequencies for longitudinal and lateral oscillations are different.

The problem, however, is that for linear homogeneous differential equations we may take into consideration both eigenfunctions and eigenvalues, while the amplitude of the eigenfunctions remains arbitrary. Suppose, an eigenfunction specifies the configuration of the excitation; though the excitation energy and pulse are the integrals of motion, and yet they can have arbitrary meanings. Ne-

vertheless, in practice we can see that energy of any excitation has quite a definite meaning both for light quantum and for any elementary particle. Therefore, within the framework of homogeneous equations it is impossible to realize the origin and the physical meaning of the Planck constant.

For linear systems, the amplitude of oscillations turns out to be quite definite under the external force; then we can express the solution by means of the Green function, which meets the homogeneous equation and has quite definite amplitude. Non-homogeneous equations are necessary for the following reasons. We know from the theory of many-body systems that, if a system consists of discrete particles, the correlation effects substantially decrease the ground state, and local states such as polarons can occur. Therefore, we pass to consideration of the ground state taking into account correlation effects.

From an endless number of particles forming a crystalline vacuum state we examine one particle as a point unit source  $Q_e = \delta(\vec{r})$ , which generates longitudinal electric field defined by equations:

$$div\vec{E}_0 = 4\pi\delta(\vec{r}); \quad rot\vec{E}_0 = 0; \quad \vec{E}_0 = \frac{\vec{r}}{r^3}.$$

Thereafter, we can write the interaction energy of the point source with vacuum fields as follows:

$$U_0 = -\frac{g}{4\pi} \vec{E}_0 \vec{P}. \tag{21}$$

Here  $g$  is the constant of interaction between the point unit field and vacuum fields; it is convenient to express this constant in a normalized form:  $g = g_1 e$ . By varying the Lagrange function over  $\vec{P}$ , we obtain a non-homogeneous equation for polarization:

$$\left(\sigma - \Delta + \frac{\partial^2}{\partial t^2}\right) \vec{P} = g_1 \vec{E}_0(\vec{r}, t); \tag{22}$$

Divergence of the left and the right parts of the Equation (22) results in the expression for the induced charge density, related to the electrical polarization for the case when a source is moving with velocity  $\vec{v}$ :

$$\left( \sigma - \Delta + \frac{\partial^2}{\partial t^2} \right) \rho_e(\vec{r}, t) = -g_1 \delta(\vec{r} - \vec{v}t). \quad (23)$$

It is obvious from (23) that the induced charge density is the Green function for a point source that fulfills the homogeneous equation over the entire space except one point; but due to this point, the function acquires quite definite values over the entire space.

At first, we consider a particular solution of Equation (23). Fourier-transformation over coordinates results in the Fourier-harmonics for the induced charge density in vacuum:

$$\rho_{ek} = -\frac{g_1}{\sigma + k^2 - (\vec{k}\vec{v})^2} \quad (24)$$

Here the corresponding coordinate dependence of the induced charge density for the case, when velocity lies in z-axis, is:

$$\rho(\vec{r}, t) = -\frac{g_1}{(2\pi)^3} \iiint \frac{\exp(i(k_x x + k_y y + k_z(z - vt)))}{\sigma + k_x^2 + k_y^2 + k_z^2(1 - v^2)} dk_x dk_y dk_z$$

Here, it is convenient to proceed to the new integration variables

$$k'_x = k_x; k'_y = k_y; k'_z = k_z \sqrt{1 - v^2}$$

in addition, to a new coordinate system:

$$x' = x; y' = y; z' = \frac{z - vt}{\sqrt{1 - v^2}}$$

After that, the induced charge density expressed in dimensional units transforms to the equation:

$$\rho(\vec{r}, t) = \frac{1}{\sqrt{1 - v^2}} \rho'(r'); \quad \rho'(r') = -\frac{g}{4\pi\xi_e^2} \frac{1}{r'} \exp\left(-\frac{r'\sqrt{\sigma}}{\xi_e}\right), \quad (25)$$

From (25) we can see that the characteristic dimension of the polarization charge is a definite value equal to the correlation radius or the Compton length of electron:  $r_e = \xi_e / \sqrt{\sigma} = c / \omega_{e0}$ . The polarization charge moving relative to the absolute coordinate system, in accordance with the Lorentz transformation, is deformed in such a way that its dimensions decrease along the direction of motion

$$r_{ex} = r_{ey} = r_{c,e}; \quad r_{ez} = r_{c,e} \sqrt{1 - v^2}.$$

Total polarization charge as an integral over the entire space is proportional to the constant of interaction  $g$  and

the vacuum susceptibility  $\sigma^{-1}$ :

$$q = \int \rho(\vec{r}, t) d\vec{r} = -\frac{g}{\sigma} \quad (26)$$

The total polarization charge does not depend on the particle velocity that we can interpret as the law of conservation of charge.

We can find a scalar potential for the motionless source from the expression:

$$\begin{aligned} \Phi(r) &= \sum_k \frac{4\pi}{k^2} \rho_k \exp(ikr) \\ &= 4\pi g \sum_k \frac{\exp(ikr)}{k^2(\sigma + k^2)} \\ &= \frac{g}{\sigma} \frac{1}{r} \left( 1 - \exp\left(-\frac{r}{r_e}\right) \right) \end{aligned} \quad (27)$$

The polarization for the electron is similar to that of the proton within an accuracy of a charge sign:

$$\bar{P}_{e,n}(\vec{r}) = \frac{g}{\sigma} \frac{\vec{r}}{r^3} \left[ 1 - \left( 1 + \frac{r}{r_{c,e,n}} \right) \exp\left(-\frac{r}{r_{c,e,n}}\right) \right]. \quad (28)$$

They only differ in the characteristic wavelength  $r_{c,e}$  and  $r_{c,n}$ . The main feature of the solution for the polarization (28) is an absence of divergence at a point  $r = 0$  that leads to the finite value of the particle energy.

Therefore, we can see that the vacuum polarization results in decrease of the source energy by  $U_0$ , both electronic and nucleonic modes having the same form:

$$U_{0e,n} = -g\Phi_{e,n}(r=0) = -\frac{g^2}{\sigma r_{c,e,n}} \quad (29)$$

Non-homogeneous Equation (23) defines two parameters: the polarization charge  $q$  and the radius of a charge localization  $r_{c,e,n}$ .

In order to determine vacuum parameters, we require that the polarization charge, both for proton and electron, be equal to the electron charge, whereas the particle energy must be equal to the ionization energy of a source out of a potential energy well, which the source creates for itself:

$$q = \frac{g}{\sigma} = e; \quad \hbar\omega_{0,e} = \frac{g^2}{\sigma r_{c,e}}; \quad \hbar\omega_{0,n} = \frac{g^2}{\sigma r_{c,n}}. \quad (30)$$

By adding the definition of the fine structure constant  $\alpha = e^2/\hbar c$  to the latter equations, we obtain the equality  $g_1 = \sigma = \alpha^{-1} \approx 137$ . It follows that the vacuum polarization  $\sigma^{-1}$  equals to the fine structure constant  $\alpha$ , whereas the constant of the interaction of a point source with vacuum fields equals to the Dirac monopole charge  $g = e/\alpha$  [7].

We can define the correlation radius and the fundamental frequency for electronic and nucleonic normal mode as follows:

$$r_{c,e} = \xi_e \sqrt{\alpha}, \quad \omega_{e,0} = \frac{1}{\tau_e \sqrt{\alpha}};$$

$$r_{c,n} = \xi_n \sqrt{\alpha}, \quad \omega_{n,0} = \frac{1}{\tau_n \sqrt{\alpha}}.$$

As a result, the rest energy in form (30) reduces to a quite transparent form:

$$\varepsilon_{e,0} = \hbar \omega_{e,0} = \frac{eg}{r_{c,e}}; \quad \varepsilon_{n,0} = \hbar \omega_{n,0} = \frac{eg}{r_{c,n}} \quad (31)$$

It follows that the point source with the interaction constant  $g$  polarizes vacuum and induces charges with dimension  $r_{c,e}$  for electronic and  $r_{c,n}$  nucleonic modes. The electric field energy for both proton and electron is equal to  $e^2/r_{c,e}$  and to  $e^2/r_{c,n}$ , correspondingly, and it turns out to be 137 times less than the energy related to the electrical polarization. We should notice that the solution for the polarization (28) is formed by three modes of normal vacuum oscillations  $P_x, P_y, P_z$ , each creating a charge equal to  $e/3$ :

$$\frac{1}{4\pi} \int \frac{\partial P_x}{\partial x} d\vec{r} = \frac{1}{4\pi} \int \frac{\partial P_y}{\partial y} d\vec{r} = \frac{1}{4\pi} \int \frac{\partial P_z}{\partial z} d\vec{r} = \frac{e}{3}.$$

Now we consider the structure of the fields in the excited state. The excited state corresponds to the generation of a source at a certain time. Suppose, a point source is generated at time  $t = 0$  under the initial conditions for polarization:

$$\vec{P}(\vec{r}, t)_{t=0} = 0; \quad \frac{\partial \vec{P}(\vec{r}, t)}{\partial t} \Big|_{t=0} = 0.$$

In this case, the general solution of Equation (22) consists of a particular solution (28) and two fundamental solutions of the homogeneous wave equation:

$$\vec{P}(\vec{r}, t) = \vec{P}^{(0)}(\vec{r}) + \vec{P}^{(+)}(\vec{r}) \exp(i\omega_0 t) + \vec{P}^{(-)}(\vec{r}) \exp(-i\omega_0 t) \quad (32)$$

By taking into account initial conditions, we can reduce the solution (32), both for electron and nucleon, to the form:

$$\vec{P}_{e,n}(\vec{r}, t) = 2e \frac{\vec{r}}{r^3} \left[ 1 - \left( 1 + \frac{r}{r_{c,e,n}} \right) \exp\left( -\frac{r}{r_{c,e,n}} \right) \right] \sin^2(\omega_{e,n,0} t) \quad (33)$$

The characteristic feature of the solution above is that the electrical polarization for both electron and proton, covers the entire infinite space and oscillates synchronously with the frequency  $\omega_{e,n,0}$ .

The solution (33), however, contains a substantial disadvantage: such wave packet cannot move in space, it is a typical standing wave. Impossibility of motion is caused by the fact that the phase velocity of different harmonics  $v_f = \omega_k/k$  changes from infinity to the light velocity  $c$ , whereas the group velocity  $v_g = \partial\omega_k/\partial k$  changes from zero to  $c$ .

In a general case, the solution for the polarization for a wave packet moving with velocity  $\vec{v}$  should have a soliton form:

$$\vec{P}(\vec{r}, t) = \vec{P}(\vec{r} - \vec{v}t) f(t) \quad (34)$$

A similar property is natural for the solution of a one-dimensional D'Alambert equation that fulfills the condition of deviation from a state of equilibrium for a flexible infinite string  $u(x, t) = u(x \pm ct)$ . A possibility of motion without changing the form is directly connected to a linear excitation spectrum in k-space  $\omega_k = ck$ . For two- and three-dimensional cases, the solution of the D'Alambert equation substantially differs from the one-dimensional one. An excitation generated in some point starts propagating at velocity  $c$  in the form of concentrated circles for two-dimensional case, and in the form of concentrated spheres for the three-dimensional case. The propagation of radio waves strictly follows the three-dimensional D'Alambert equation, which proceeds from the Maxwell equations. Radio waves, however, are a multiquantum process. Nevertheless, a single quantum, while having wave properties, yet behaves like a particle. The thing is that a light quantum radiated by an excited atom at a distant star can cover million years without spreading dispersion. After colliding with a similar atom on the Earth, the light quantum transfers into a similar state of excitation. Therefore, there must be a solution of a soliton type for a light quantum in the form (34), which gives the origin of ray optics.

Analysis shows that it is impossible to obtain such a spectrum in a three-dimensional isotropic space for one order parameter. Following strictly the terminology, we should consider electromagnetic oscillations as coupled oscillations of a two-component order parameter in the form of an electric and magnetic polarization of vacuum.

Suppose a magnetic polarization with the same Hamiltonian, as that for the electric polarization (7) is possible to appear in vacuum:

$$H = \frac{1}{8\pi} \int \left( \tau_{e,n}^2 \vec{M}^2 + \xi_{e,n}^2 (\nabla \vec{M})^2 + \sigma \vec{M}^2 \right) d\vec{r} \quad (35)$$

We define a magnetic order parameter, as well as an electric polarization, through the sum of the elementary magnetic moments:

$$\vec{M} = \frac{4\pi}{\delta V} \sum \vec{\mu}_i.$$

Practice shows that electric and magnetic dipole mo-

ments create, correspondingly, electric and magnetic fields, similar in configuration:

$$\begin{aligned}\vec{E}(\vec{r}) &= \frac{3(\vec{r}-\vec{r}')(\vec{d}(\vec{r}-\vec{r}'))}{|\vec{r}-\vec{r}'|^5} - \frac{\vec{d}}{|\vec{r}-\vec{r}'|^3}; \\ \vec{H}(\vec{r}) &= \frac{3(\vec{r}-\vec{r}')(\vec{\mu}(\vec{r}-\vec{r}'))}{|\vec{r}-\vec{r}'|^5} - \frac{\vec{\mu}}{|\vec{r}-\vec{r}'|^3}.\end{aligned}\quad (36)$$

It follows that for a similar distribution of the electric and magnetic polarization, electric and magnetic fields will be similar as well. We can reduce expressions (36) to the form:

$$\begin{aligned}\vec{E}(\vec{r}) &= -\nabla\Phi_d(\vec{r}); \quad \Phi_d = \vec{d}\nabla_{r'}\Phi_0(\vec{r}-\vec{r}'); \\ \vec{H}(\vec{r}) &= -\nabla\Phi_\mu(\vec{r}); \quad \Phi_\mu = \vec{\mu}\nabla_{r'}\Phi_0(\vec{r}-\vec{r}'),\end{aligned}\quad (37)$$

Here  $\Phi_0$  is the potential Coulomb function for a unit source  $\Phi_0 = 1/|\vec{r}-\vec{r}'|$ . Under an arbitrary distribution of the electric and magnetic polarization, scalar potentials (37) acquire the form:

$$\begin{aligned}\Phi_p &= \frac{1}{4\pi} \int \vec{P}(\vec{r}')\nabla_{r'}\Phi_0(\vec{r}-\vec{r}')d\vec{r}' \\ &= -\frac{1}{4\pi} \int \frac{div\vec{P}(\vec{r}')}{|\vec{r}-\vec{r}'|}d\vec{r}' \\ &= \int \frac{\rho_e(\vec{r}')}{|\vec{r}-\vec{r}'|}d\vec{r}'; \\ \Phi_M &= \frac{1}{4\pi} \int \vec{M}(\vec{r}')\nabla_{r'}\Phi_0(\vec{r}-\vec{r}')d\vec{r}' \\ &= -\frac{1}{4\pi} \int \frac{div\vec{M}(\vec{r}')}{|\vec{r}-\vec{r}'|}d\vec{r}' \\ &= \int \frac{\rho_\mu(\vec{r}')}{|\vec{r}-\vec{r}'|}d\vec{r}',\end{aligned}\quad (38)$$

It follows that the sources of the electric field are the electric charges defined by the relation  $div\vec{P} = -4\pi\rho_e$ , whereas the sources of the magnetic field are the magnetic charges defined by the relation  $div\vec{M} = -4\pi\rho_\mu$ . As a result, the electric and magnetic fields meet the conditions:

$$div\vec{E} = 4\pi\rho_e; \quad div\vec{H} = 4\pi\rho_\mu.$$

Energy of the electric and magnetic fields turns up to be 137 times less than that of the electric and magnetic polarization, correspondingly. The configurations of the electric and magnetic fields are similar under the similar distribution of the electric and magnetic polarization. For example, if we create a homogeneous electric polarization  $\vec{P}$  in a full-sphere, then it causes generation of the depolarizing electric field inside the sphere  $\vec{E} = -\vec{P}/3$ ;

therefore, the depolarization coefficient for a sphere is equal to 1/3. The situation is the same with a spherical magnet:  $\vec{H} = -\vec{M}/3$ . Generation of the magnetic field also leads to the long-range Coulomb interaction between the normal oscillations:  $M_{ex}, M_{ey}, M_{ez}, M_{nx}, M_{ny}, M_{nz}$ .

We can define the electric current with the expression:

$$4\pi\vec{j}_e = \dot{\vec{P}} + rot\vec{M}.$$

The continuity equation follows from here:

$$div\vec{j}_e + \frac{\partial\rho_e}{\partial t} = 0.$$

Now we show in what way the interaction between the electric and magnetic polarization provides the solution of the soliton type. We add the interaction energy of currents to the Hamiltonians (7) and (35) in the form:

$$U = \frac{\xi_e\tau_e}{4\pi} \int (\dot{\vec{P}} \cdot rot\vec{M} - \dot{\vec{M}} \cdot rot\vec{P})d\vec{r}\quad (39)$$

From there we obtain the combined equations for a plane polarized electromagnetic wave:

$$\begin{aligned}\left(\sigma - \Delta + \frac{\partial^2}{\partial t^2}\right)P_x(\vec{r},t) - 2\frac{\partial}{\partial t}\frac{\partial}{\partial z}M_y(\vec{r},t) &= 0; \\ -2\frac{\partial}{\partial t}\frac{\partial}{\partial z}P_x(\vec{r},t) + \left(\sigma - \Delta + \frac{\partial^2}{\partial t^2}\right)M_y(\vec{r},t) &= 0.\end{aligned}\quad (40)$$

By setting up the solutions in the form:

$$\begin{aligned}P_x(\vec{r},t) &= P_x \exp(i(\vec{k}\vec{r} + \omega t)); \\ M_y(\vec{r},t) &= M_y \exp(i(\vec{k}\vec{r} + \omega t)),\end{aligned}\quad (41)$$

we can obtain the system of equations:

$$\begin{aligned}(\sigma + k^2 - \omega^2)P_x - 2\omega k_z M_y &= 0; \\ -2\omega k_z P_x + (\sigma + k^2 - \omega^2)M_y &= 0.\end{aligned}\quad (42)$$

The compatibility condition for the Equations (42) leads to the equation:

$$\begin{vmatrix} \sigma + k^2 - \omega^2 & -2\omega k_z \\ -2\omega k_z & \sigma + k^2 - \omega^2 \end{vmatrix} = 0,$$

This gives the spectrum of normal oscillations:

$$\omega = \pm k_z \pm \sqrt{\sigma + k_x^2 + k_y^2 + 2k_z^2},$$

After that, the solutions for the electric and magnetic polarization transmitting with the light velocity reduce to the soliton form:

$$\begin{aligned}P_x(\vec{r},t) &= a \cdot \exp(i(k_x x + k_y y + k_z(z \pm t))) \\ &\quad \exp\left(i\left(\pm t \sqrt{\sigma + k_x^2 + k_y^2 + 2k_z^2}\right)\right); \\ M_y(\vec{r},t) &= a \cdot \exp(i(k_x x + k_y y + k_z(z \pm t)))\end{aligned}$$

$$\exp\left(i\left(\pm t\sqrt{\sigma+k_x^2+k_y^2+2k_z^2}\right)\right).$$

We proceed from the supposition that the electron radiates a light quantum; then from a wide range of possible solutions we should choose a solution compatible with the own field of the electron. Since the light quantum propagating along  $z$ -axis has a wave vector  $k_z$ , we can specify a Fourier-harmonic  $k_z$  from the scalar potential (27) which defines the field of the electron. In the cylindrical coordinate system, the Fourier-harmonic for the scalar potential becomes:

$$\begin{aligned}\Phi_{k_z} &= \int_{-\infty}^{\infty} \Phi \exp(-ik_z z) dz \\ &= q\left(K_0(rk_z) - K_0\left(r\sqrt{2\sigma+k_z^2}\right)\right).\end{aligned}$$

Here  $K_0$  is the Macdonald function. We express the electric polarization along the  $x$ -axis as  $P_x = \partial\Phi/\partial x$ . Thus, for a plane-polarized wave compatible with the field of the electron and fulfilling the system of Equation (40), we obtain the solution for the electric polarization:

$$\begin{aligned}P_x &= q\left(k_z K_1(rk_z) - \sqrt{2\sigma+k_z^2} K_1\left(r\sqrt{2\sigma+k_z^2}\right)\right) \\ &\cos\varphi \exp\left(i\left(k_z(z-t) \pm \sqrt{2\sigma+k_z^2} \cdot t\right)\right)\end{aligned}\quad (43)$$

This solution is a quasi-one-dimensional infinite monochromatic wave propagating at the light velocity along the  $z$ -axis and interacting with the similar magnetic polarization  $M_y$ . In the transversal direction, the monochromatic wave (43) is localized with the dimension equal to the wavelength, since the Macdonald function at big values of argument approximately equals:

$$K_1(x) \approx \sqrt{\frac{\pi}{2x}} \exp(-x).$$

This precisely corresponds to the experiment, as it is impossible to localize a light ray more than the light wavelength.

Therefore, from the values, which we consider as fundamental  $e, \hbar, c, m_e, m_p$ , we go over to the set of values, which characterize properties of physical vacuum  $\alpha, g, \xi_e, \xi_p, \tau_e, \tau_p$  under the additional condition:  $\xi_e/\tau_e = \xi_p/\tau_p = c$ . In connection with this, we must change the concepts of mass and matter.

Wave equations can only be applied to the material medium having definite dynamic properties, so the idea of physical vacuum means that the entire infinite space is filled with a definite matter. The particles that we observe – electrons, protons, photons – these are excitations of vacuum in the form of wave packets, which are eigenfunctions of the united system of twelve equations. From

the point of view of wave mechanics, we can characterize a wave packet with energy, momentum, angular momentum and oscillation amplitude; specifically for the electric polarization, we define the amplitude by the electric charge. For a multi-component order parameter, the form or symmetry of oscillations is important. In this connection, the concept of a particle mass does not have independent meaning. Researchers introduced the values of mass and charge, as well as Planck constant for particles, in different periods of time and so far, they have considered these values as independent ones. As we showed above, charge quantization and existence of Planck constant are the consequences of correlation effects related to discreteness of physical vacuum. Now it makes sense to study the concept of mass for a wave packet.

From practice we know that, if we describe the particle oscillation spectrum with the expression:

$$\omega_k = \sqrt{\omega_0^2 + c^2 k^2}$$

then the particle velocity is equal to the group velocity:

$$\vec{v} = \vec{v}_g = \frac{\partial\omega_k}{\partial\vec{k}} = \frac{c^2\vec{k}}{\sqrt{\omega_0^2 + c^2\vec{k}^2}}\quad (44)$$

If we express the wave vector  $\vec{k}$  from (44) through the group velocity, we obtain the value of frequency in the form:

$$\omega_k = \sqrt{\omega_0^2 + c^2 k^2} = \frac{\omega_0}{\sqrt{1 - \frac{v^2}{c^2}}}\quad (45)$$

Multiplying terms of (45) by  $\hbar$ , we come to the relativistic expression for the particle energy:

$$E(v) = \frac{\hbar\omega_0}{\sqrt{1 - \frac{v^2}{c^2}}} = \frac{E_0}{\sqrt{1 - \frac{v^2}{c^2}}} \approx E_0 + \frac{E_0}{2} \frac{v^2}{c^2} = E_0 + \frac{mv^2}{2}\quad (46)$$

The expression for the particle mass  $m = E_0/c^2$  follows from the latter Equation (46), the concept of mass being not necessary if we specify velocity in terms of light velocity.

The examples given below illustrate how to express some known values in terms of vacuum parameters:

De Broglie wavelength:

$$\begin{aligned}\lambda_{\partial,e} &= \frac{\hbar}{m_e v} = \frac{\hbar}{P} = \frac{\hbar}{\hbar k} = \frac{1}{k}; \\ \lambda_{\partial,n} &= \frac{\hbar}{m_n v} = \frac{1}{k}.\end{aligned}$$

Here we have to consider  $k$ , the particle wave vector, as a quantum number independent of vacuum parameters.

Compton wavelength:

$$\lambda_{K,e} = \frac{\hbar}{m_{e,0}c} = \frac{c}{\omega_{0,e}} = r_{c,e} = \xi_e \sqrt{\alpha};$$

$$\lambda_{K,n} = \frac{\hbar}{m_{n,0}c} = \frac{c}{\omega_{0,n}} = r_{c,n} = \xi_n \sqrt{\alpha}$$

Classical radius of electron:

$$r_{0,e} = \frac{e^2}{m_{e,0}c^2} = r_{c,e} \alpha = \xi_e \alpha^{3/2}.$$

Bohr radius:

$$a_B = \frac{\hbar^2}{m_{e,0}e^2} = \frac{r_{c,e}}{\alpha} = \frac{\xi_e}{\sqrt{\alpha}} \quad (47)$$

Bohr energy:

$$E_B = \frac{m_{0,e}e^4}{\hbar^2} = m_{0,e}c^2 \alpha^2 = \frac{eg}{r_{c,e}} \alpha^2 \quad (48)$$

By making Bohr energy equal to photon energy,

$$E_B = \hbar \omega_{\gamma,B} = \hbar c k_{\gamma,B}$$

we obtain  $\gamma$ - quantum wavelength, which corresponds to Bohr energy

$$\lambda_{\gamma,B} = \frac{1}{k_{\gamma,B}} = \frac{\hbar^3 c}{m_{0,e}e^4} = \frac{r_{c,e}}{\alpha^2} = \frac{\xi_e}{\alpha^{3/2}}.$$

We can express Rydberg constant through vacuum parameters:

$$R = \frac{m_{0,e}e^4}{2\hbar^3} = \frac{1}{2} \omega_{0,e} \alpha^2 = \frac{\alpha^{3/2}}{2\tau_e}.$$

It follows from the above expressions that fine structure constant characterizes not only the fine structure of the hydrogen atomic spectrum but the entire lengths hierarchy of the quantum mechanics as well. It is easy to see that characteristic lengths form a geometrical progression:

$$r_{0,e} = \alpha r_{c,e} = \alpha^2 a_B = \alpha^3 \lambda_{\gamma,B}.$$

All the lengths contain neither Planck constant, nor mass, nor charge of electron. In this connection, it makes sense to express the Schrödinger equation through the natural parameters of physical vacuum.

The Hamiltonian for the Schrödinger equation for a hydrogen atom looks like this:

$$H = -\frac{\hbar^2}{2m_{e,0}} \nabla^2 - \frac{e^2}{r}.$$

In this expression, we take the fundamental constants  $\hbar, m_{e,0}, e$ , which specify the characteristic parameters of a hydrogen atom (47-48), as independent; however, as we

demonstrated above, none of these constants ought to be taken as a fundamental one.

We can write the Hamiltonian of the electron in the nuclear field of a hydrogen atom in a different form:

$$H = \hbar \sqrt{\omega_{0,e}^2 + c^2 k^2} - \frac{e^2}{r} \quad (49)$$

The Planck constant expressed through the electron charge reduces (49) to the form

$$H = \frac{e^2 \omega_{0,e}}{\alpha c} \sqrt{1 + \frac{c^2 k^2}{\omega_{0,e}^2}} - \frac{e^2}{r} = \frac{eg}{r_{c,e}} \left( \sqrt{1 + r_{c,e}^2 k^2} - \frac{\alpha r_{c,e}}{r} \right) \quad (50)$$

Here, it is convenient to use the dimensionless length  $r \Rightarrow r/r_{c,e}$ , the dimensionless wave vector  $\vec{k} \Rightarrow \vec{k} \cdot r_{c,e}$  and the dimensionless time  $t \Rightarrow \omega_{0,e} t$ . We express the energy in terms of the electron rest energy  $eg/r_{c,e}$ :

$$H = \sqrt{1 + k^2} - \frac{\alpha}{r} \approx 1 + \frac{1}{2} k^2 - \frac{\alpha}{r} \quad (51)$$

The particle velocity is equal to the group velocity of the wave packet  $\vec{v} = \partial \omega_k / \partial \vec{k} = \vec{k} / \sqrt{1 + k^2} \approx \vec{k}$  and we express it in terms of light velocity. Approximate expressions correspond to the case of a low velocity  $k \approx v \ll 1$ . We can regard the value  $k^2$  in the approximate expression (51) as the eigenvalue of the Laplacian operator; then we may reduce (51) to the equation for the eigenfunction and the eigenvalue:

$$H\psi = \varepsilon\psi; \quad H = -\frac{1}{2} \nabla^2 - \frac{\alpha}{r} \quad (52)$$

From (52) it follows that the Schrödinger equation only contains one dimensionless small parameter  $\alpha$  of a physical vacuum susceptibility. The fundamental function  $\Psi$  of a free electron in Cartesian coordinates is equal to  $\exp(i\vec{k}\vec{r})$ ; we express the eigenvalue by the equality:  $\varepsilon = k^2/2$ .

Now we find out the Bohr quantization conditions for a hydrogen atom. The circular motion of electron around an atomic nucleus is defined by the equality of centrifugal and centripetal forces:

$$r\dot{\varphi}^2 = \frac{\alpha}{r^2}. \quad (53)$$

Bohr assumed a quantization of adiabatic invariants:

$$\oint p_i dq_i = nh$$

For the circular motion, the latter relation reduces to the form:

$$pr = nh$$

Externally, it looks as if a quantum of action existed, that provides quantization of a pulse moment. However,

by taking into consideration the pulse  $p = \hbar k$ , we come to the cyclic boundary conditions for a wave vector:

$$kr = n.$$

It follows that Planck constant has nothing to do with forming the wave function. Since  $k = v = r\dot{\phi}$ , we can add to Equation (53):

$$r^2\dot{\phi} = n$$

From where we can obtain the energy, radius and velocity at the stationary Bohr orbits:

$$\varepsilon_n = -\frac{\alpha^2}{2n^2}; r_n = \frac{n^2}{\alpha}; v_n = \frac{\alpha}{n}.$$

That accurately corresponds to the relations (47,48).

Compton scattering, which we regard as one of the evidences proving existence of quantum of action, proceeds from the laws of conservation of energy and momentum for electron and  $\gamma$ -quantum:

$$\begin{aligned} m_{e,0}c^2 + \hbar\omega_\gamma &= \frac{m_{e,0}c^2}{\sqrt{1-\frac{v^2}{c^2}}} + \hbar\omega'_\gamma; \\ \hbar\vec{k}_\gamma &= \frac{m_{0,e}\vec{v}}{\sqrt{1-\frac{v^2}{c^2}}} + \hbar\vec{k}'_\gamma. \end{aligned} \quad (54)$$

It follows from (54), that we can specify the wave vector of a scattered light by the relation:

$$k'_\gamma = \frac{k_\gamma}{1 + \frac{\hbar k_\gamma}{m_{e,0}c}(1 - \cos\theta)}, \quad (55)$$

Here  $\theta$  is the angle between vectors  $\vec{v}$  and  $\vec{k}'$ ; besides, there is a length parameter  $\tilde{\lambda}_{K,e} = \hbar/m_{e,0}c$  where we take the values  $\hbar, m_{e,0}, c$  as the fundamental ones. However, by taking into consideration the fact, that relations (5) and (6) define the spectrum of a particle, we can reduce combined Equation (54) to the form:

$$\begin{aligned} \omega_{e,0} + ck_\gamma &= \sqrt{\omega_{e,0}^2 + c^2k^2} + ck'_\gamma; \\ \vec{k}_\gamma &= \vec{k} + \vec{k}'_\gamma, \end{aligned}$$

It follows that the scattering characteristic is defined neither by the Planck constant nor by the electron mass, but by the space and frequency resonance for the wave packets; scattering being submitted to the same Formula (55) with the Compton length  $\tilde{\lambda}_{K,e} = c/\omega_{e,0} = r_{c,e} = \xi\sqrt{\alpha}$  equal to the correlation radius.

Once in his days Planck supposed that radiation and absorption of light should proceed by quanta. Later this brilliant supposition was confirmed. After that, scientists

had only to examine the properties of electron responsible for light radiation and absorption in a quantum way. Albert Einstein, however, considered something different. Since we can observe light quanta, then light is quantized due to existence of quantum of action; the question “Why?” being quite inappropriate here since physical mechanism for quantization of action just does not exist. We can only say that these are the properties of space-time. We just substitute one senseless statement by another one. Nevertheless, proceeded from the fact that electron radiates and absorbs light per quanta, a planetary model of electron is suggested by itself. The electron rest energy equals to:  $\varepsilon_{0,e} = \hbar\omega_{0,e} = eg/r_{c,e}$ . We can write  $\gamma$ -quantum energy in a similar way:  $\varepsilon_\gamma = \hbar\omega_\gamma = egk_\gamma$ . Since the photon spin equals to  $\hbar$ , then, by representing it in the form of the orbital moment  $s = pr = \hbar k_\gamma r_\gamma = \hbar$ , we come to quite transparent cyclic conditions for the radius of photon orbit  $k_\gamma r_\gamma = 1$ . After that, the photon energy reduces to the form:  $\varepsilon_\gamma = eg/r_\gamma$ . We can obtain such an energy as follows: use the solution for the electron polarization in the form (28), set it up into Hamiltonian (7) and integrate over space from infinity to the radius  $r_\gamma$ . Therefore, the nature of fields for photon and electron is the same. By radiating photon, an electron takes off some part of its polarization coat, the intrinsic energy of the electron being reduced.

### 3. Gravitational Optics

In the previous part we showed that all particles can be considered as excitations of physical vacuum; they are the solutions of the unified system of equations for coupled oscillations of the multicomponent order parameter  $(\vec{P}, \vec{M})$ . That is why we can be sure to a certain degree that all particles similarly contribute to the gravitational interaction, particle energy being the interaction parameter. Now we write down the standardized form of the Hamiltonian for a particle in the gravitational field caused by a massive body of mass  $m_1$

$$H = \varepsilon(\vec{p}) - \frac{\gamma mm_1}{r} \quad (56)$$

We express the particle mass through energy  $m = \varepsilon(\vec{p})/c^2$ ; after that the Hamiltonian (56) reduces to the form:

$$H = \varepsilon(\vec{p}) \left(1 - \frac{r_g}{r}\right); \quad r_g = \frac{\gamma m_1}{c^2}. \quad (57)$$

Here  $r_g$  is the gravitational radius which scales gravitational potential of a massive body. For an arbitrary potential, the Hamiltonian has the form:

$$H = \varepsilon(\vec{p})(1 - \Phi(\vec{r})).$$

In general case, particle energy is defined by the follo-

wing expression:

$$\varepsilon(\vec{p}) = \sqrt{\varepsilon_0^2 + c^2 \vec{p}^2} \quad (58)$$

In addition, particle velocity equals to

$$\vec{v} = \frac{\partial \varepsilon(\vec{p})}{\partial \vec{p}} \quad (59)$$

From the coordinate system  $(x, y, z, t)$  we proceed to a new time  $t \Rightarrow ct$  and, in Equation (58) – to a new momentum  $c\vec{p} \Rightarrow \vec{p}$ ; then the particle velocity does not depend on the chosen scales of length and time, but becomes a dimensionless value expressed in terms of light velocity:

$$\vec{v} = \frac{\partial \varepsilon(\vec{p})}{\partial \vec{p}} = \frac{\vec{p}}{\sqrt{\varepsilon_0^2 + \vec{p}^2}} \quad (60)$$

The second equation that defines the particle motion in the gravitational field looks like this:

$$\dot{\vec{p}} = -\nabla H = \varepsilon(\vec{p}) \nabla \Phi \quad (61)$$

By taking into account Equation (60), we can rewrite (61) as follows:

$$\frac{d}{dt}(\vec{v}\varepsilon(p)) = \varepsilon(p) \nabla \Phi(\vec{r}) \quad (62)$$

For low velocities we can substitute value  $\varepsilon(p)$  by an approximate expression  $\varepsilon_0$ ; after that Equation (62) reduces to that of Newton's mechanics:

$$\ddot{\vec{r}} = \nabla \Phi(\vec{r}).$$

Based upon this equation, Albert Einstein affirmed that the inertial mass and the gravitating mass are equivalent. This statement, however, is incorrect. An accurate equation of motion (62) is transformed to:

$$\ddot{\vec{r}} = \nabla \Phi(\vec{r}) - \vec{v}(\vec{v} \nabla \Phi(\vec{r})) \quad (63)$$

It follows, that particle inertia depends on the direction of motion. It is interesting to note that the intrinsic (internal) energetic properties of a particle are lost in the equation of motion (63). This means that we can apply the obtained equation to any relatively compact object. It can be a planet, a satellite, an electron, a proton, a photon, a neutrino—all the same.

Bearing in mind (60), we reduce (61) as follows:

$$\frac{\vec{p}\dot{\vec{p}}}{\varepsilon_0^2 + p^2} = \vec{v} \cdot \nabla \Phi(\vec{r}),$$

From the latter equation we obtain the integral of motion in two different forms:

$$\begin{aligned} \varepsilon(p) \exp(-\Phi) &= const; \\ (1-v^2) \exp(2\Phi) &= const. \end{aligned} \quad (64)$$

Now we examine the motion in the Coulomb potential with the Hamiltonian (57). In a centrally symmetrical field motion develops in a plane crossing the centre of a massive body; therefore, we can re-write Equation (63) for the plane  $(x, y)$ :

$$\ddot{x} = -\frac{r_g}{r^3}(x - \dot{x}(x\dot{x} + y\dot{y})); \quad (65)$$

$$\ddot{y} = -\frac{r_g}{r^3}(y - \dot{y}(x\dot{x} + y\dot{y})).$$

In the polar coordinate system Equation (65) becomes

$$\ddot{r} - r\dot{\varphi}^2 = \frac{r_g}{r^2}(1 - \dot{r}^2); \quad (66)$$

$$r\ddot{\varphi} + 2\dot{r}\dot{\varphi} = \frac{r_g}{r}\dot{\varphi}.$$

The second equation in (66) can be integrated easily; after that we obtain the integral of motion corresponding to the angular momentum conservation law:

$$r^2\dot{\varphi} \exp\left(\frac{r_g}{r}\right) = const. \quad (67)$$

At the beginning, we consider a circular motion:  $\ddot{r} = \dot{r} = 0$ . Then, the first equation of (66) leads to

$$r\dot{\varphi}^2 = \frac{r_g}{r^2}; \dot{\varphi} = \frac{r_g^{1/2}}{r^{3/2}}, \quad (68)$$

This exactly coincides with the results of Kepler's problem, the first space velocity on the orbit of radius  $r$  being equal to

$$v_1 = r\dot{\varphi} = \sqrt{\frac{r_g}{r}} \quad (69)$$

Consequently, the first space velocity attains to the light velocity at  $r = r_g$ .

Further, we consider an arbitrary motion relative to a heavy centre. Let us assume that at time  $t = 0$ , a particle has coordinates  $(r = r_0, \varphi = 0)$ , complete velocity  $v_0$  and azimuth velocity  $v_{\varphi 0} = r_0\dot{\varphi}_0$ . From the integrals of motion (64, 67) it follows:

$$1 - v^2 = 1 - \dot{r}^2 - r^2\dot{\varphi}^2 = (1 - v_0^2) \exp\left(2\left(\frac{r_g}{r_0} - \frac{r_g}{r}\right)\right); \quad (70)$$

$$r^2\dot{\varphi} = r_0^2\dot{\varphi}_0 \exp\left(\frac{r_g}{r_0} - \frac{r_g}{r}\right).$$

From the system of Equation (70) we obtain the equation that combines  $\varphi$  and  $r$ :

$$d\varphi = \frac{v_{\varphi 0} dr}{r \sqrt{\left(\frac{r}{r_0}\right)^2 \left( \exp\left(2\left(\frac{r_g}{r} - \frac{r_g}{r_0}\right)\right) - 1 + v_0^2 \right) - v_{\varphi 0}^2}} \quad (71)$$

Now proceed to a new variable  $\rho = r/r_0$  and new parameters of the problem:

$$\beta = r_g/r_0; v_{\varphi 0} = \sqrt{\beta(1+\delta)}. \quad (72)$$

We examine the situation when the radial velocity at the starting point is zero. It follows that  $v_0 = v_{\varphi 0}$ ; after this, Equation (71) acquires the form

$$d\varphi = \frac{\sqrt{\beta(1+\delta)}d\rho}{\rho\sqrt{\rho^2 \left[ \exp\left(2\beta\left(\frac{1}{\rho}-1\right)\right) - 1 + \beta(1+\delta) \right] - \beta(1+\delta)}} \quad (73)$$

Here, the parameter  $\delta$  defines a deviation from the circular motion in an orbit. We apply the Equation (73) to the Solar system. The gravitational radius of the Sun equals to 1.5 km. The radius of the terrestrial orbit is  $1.5 \cdot 10^8$  km, the radius of Mercury orbit is  $0.5 \cdot 10^8$  km, the radius of the solar sphere is  $6.96 \cdot 10^5$  km. The parameter  $\beta$  in (73) is equal to  $\beta_E = 10^{-8}$  for the Earth planet; to  $\beta_M = 3 \cdot 10^{-8}$  for the Mercury; and to  $\beta_S = 2,1 \cdot 10^{-6}$  for the Sun surface. It follows that the circular orbital velocity of the Earth is  $v_{\varphi E} = \sqrt{\beta_E} = 10^{-4}$ . In dimensional terms the circular velocity of the Earth equals to  $10^{-4}c = 30$  km/cek. The Mercury moves in an elliptic orbit according to (73), where the value  $\beta \ll 1$ . Second order expansion in series of the exponent (73) leads to the equation

$$\varphi = \int_1^{\rho} \frac{d\rho\sqrt{1+\delta}}{\rho\sqrt{-(1-\delta-2\beta)\rho^2 + 2(1-2\beta)\rho - (1+\delta-2\beta)}}, \quad (74)$$

It enables to obtain the orbit path

$$\rho = \frac{1+\delta-2\beta}{1-2\beta+\delta \cos\left(\varphi\sqrt{\frac{1+\delta-2\beta}{1+\delta}}\right)} \quad (75)$$

We can find the complete revolution of the path from the condition:

$$\varphi\sqrt{\frac{1+\delta-2\beta}{1+\delta}} = 2\pi$$

Consequently, the angle gain over one revolution of the path is

$$\varphi \approx 2\pi\left(1 + \frac{\beta}{1+\delta}\right).$$

The century displacement of the Mercury perigee means that while the Earth makes 100 revolutions around the Sun, the Mercury makes the number of revolutions

equal to  $100(\beta_M/\beta_E)^{3/2}$ . From here we obtain

$$\Delta\varphi = 100 \frac{2\pi\beta_M}{1+\delta_M} \left(\frac{\beta_M}{\beta_E}\right)^{3/2} = 21'' \quad (76)$$

The value  $\delta_M = 0,2$  is the eccentricity of the Mercury elliptic orbit.

From (75) we can obtain the condition when an elliptic orbit transforms into a parabolic path:

$$1 - 2\beta - \delta = 0.$$

It follows that the second space velocity is a little less than that of Kepler's problem and is equal to

$$v_2 = v_{\varphi 0} = \sqrt{\beta(1+\delta)} = \sqrt{2\beta(1-\beta)} = v_1\sqrt{2(1-v_1^2)} \quad (77)$$

Further, we consider the motion of a photon or a neutrino in a gravitational field. In this case, for the equation of motion (71), it is necessary to assume  $v_0 = v_{\varphi 0} = 1$ . Then, Equation (71) leads to

$$\varphi = \int_1^{\rho} \frac{d\rho}{\rho\sqrt{\rho^2 \exp\left(2\beta\left(\frac{1}{\rho}-1\right)\right) - 1}} \quad (78)$$

In order to calculate the complete angle of displacement  $\varphi_B$  for a light beam passing a gravitating mass, we move to a new variable  $\xi = 1/\rho$  and, as a result, we obtain:

$$\varphi_B = \int_0^1 \frac{2d\xi}{\sqrt{\exp(2\beta(\xi-1)) - \xi^2}} \quad (79)$$

Integral (79) is divergent at  $\beta \rightarrow 1$ . It proceeds from the fact that at the gravitational radius a photon has a stationary orbit. For  $\beta \ll 1$ ,

$$\varphi_B \approx \pi + 2 \arcsin \beta \quad (80)$$

it follows that the deviation of a light beam moving, for example, along the Sun surface is  $0.86''$ . The only stationary orbit for a photon is  $r = r_g$  that corresponds to the parameter  $\beta = 1$ . The slightest deviation from unit makes a photon either leave for infinity, or fall down to the centre. **Figure 1** illustrates a photon getting off a stationary orbit.

Now we study a radial motion which we can determine from the integrals of motion (68). Under the given input conditions of the coordinate and velocity directed along the radius, and by using the integrals of motion (68), we obtain the energy of a photon moving away from the centre:

$$\varepsilon(p) = p = p_0 \exp\left(-\beta\left(1 - \frac{1}{\rho}\right)\right) \quad (81)$$

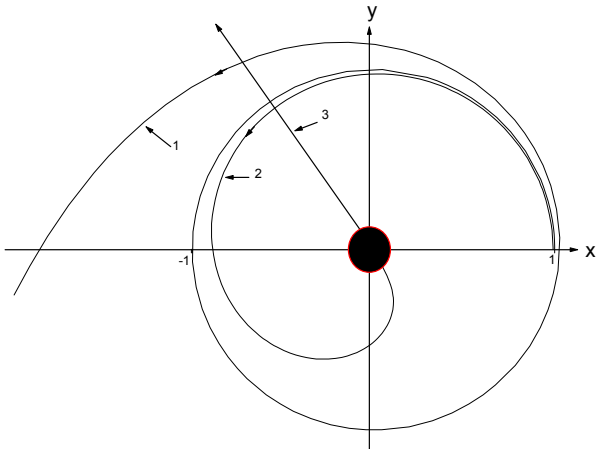


**Figure 1.** The paths of a photon at different initial conditions. Curve 1 exhibits the photon leaving for infinity at the input condition  $\beta = 0.9999$ . Curve 2 shows the photon falling down to the centre at  $\beta = 1.01$ . Arrow 3 displays the photon radially leaving for infinity from under the gravitational radius

It follows that the photon crosses freely the gravitational radius and at the infinity the photon energy equals to:

$$p = p_0 \exp(-\beta) = p_0 \exp\left(-\frac{r_g}{r_0}\right) \quad (82)$$

The radial velocity of the photon remains constant;

$$v_x = \frac{p_x}{p}; v_y = \frac{p_y}{p}; v^2 = v_x^2 + v_y^2 = \frac{p_x^2 + p_y^2}{p^2} = 1.$$

The velocity of particles with non-zero mass is defined by the equation:

$$(1 - v^2) \exp\left(2\frac{r_g}{r}\right) = (1 - v_0^2) \exp\left(2\frac{r_g}{r_0}\right) \quad (83)$$

From (83) we can define the second space velocity:

$$v_0^2 = v_2^2 = 1 - \exp(-2\beta), \quad (84)$$

it follows from (84) that at the initial velocity  $v_0 > v_2$ , any particle crosses freely the gravitational radius and leaves for infinity. Note that the first space velocity  $v_1$  equals to  $\sqrt{\beta}$ . A circular orbit is steady under the condition that  $v_2 > v_1$  from the equation

$$\beta = 1 - \exp(-2\beta)$$

we define the boundary of stability for circular orbits  $\beta = \beta_c \approx 0.796812$ . Circular orbits are only stable to small disturbances under the condition  $\beta < \beta_c$ . This situation is described by the equation of motion (73) where we can consider the value of  $\delta$  as a disturbance

of a circular orbit. It follows from (73) that for  $\beta < \beta_c$  any small value  $\delta > 0$  makes a particle leave for infinity along the path similar to that shown on **Figure 1** (curve 1). Under the disturbance  $\delta < 0$ , a particle falls down to the centre and as well leaves for infinity along the curve similar to 2, 3 on **Figure 1**.

Since all bodies in the Solar system obey the same equation of motion (66), we can measure time in terms of any periodical process that occurs in the Solar system; for example, in terms of revolution of the Earth around the Sun. Further, since we can calculate the periods of revolution for any bodies beforehand, time in the entire Solar system runs similarly. Moreover, we extend the time over the entire visible part of the Universe; and we are quite right when we measure time in billions of years, whereas we measure distance in billions of light years.

Therefore, following Newton, we can repeat that a particle moves uniformly and straight until no force is applied. Following Galilee, we can say that under the same initial conditions in the gravitational field all particles move along the same paths. For example, under the same initial conditions an ultra relativistic proton moves in the same path as a photon does. However, Einstein's statement that time runs differently in each lift does not have any physical meaning, since every electron covers the entire infinite space (33) and simultaneously interacts with all particles in the Universe.

#### 4. Problems of Dark Matte

In the previous section we introduced the concept that it is the total particle energy  $\varepsilon(\vec{p})$  which plays the key part in the gravitational interaction, but not the rest mass, as it is usually considered. This fact substantially changes the estimations of the matter quantity participating in the gravitational interaction. For example, the protons whose energy achieves  $10^{21}$  eV in cosmic rays create a gravitational potential  $10^{12}$  times higher than that for protons on the Earth whose energy is  $10^9$  eV. The situation is similar for neutrino. The mean energy of neutrino emitted by neutron beta decay is about  $10^6$  eV; whereas zero energy of neutrino, which we usually take into account for gravitational interaction, is estimated by value of 10 eV. Consequently, neutrino contributes into the gravitational interaction  $10^5$  times more. Photons having zero mass are not considered as carriers of the gravitational interaction at all. Deviation from the straight motion for a photon is caused by the Einstein deflection effect. This point of view contradicts elementary physics. The thing is that, if two bodies exist at positions  $\vec{r}_1$  and  $\vec{r}_2$ , and interact according to the law  $U(\vec{r}_1 - \vec{r}_2)$ , then their momenta  $\vec{p}_1$  and  $\vec{p}_2$  follow the equations

$$\dot{\vec{p}}_1 = -\nabla_1 U(\vec{r}_1 - \vec{r}_2); \quad \dot{\vec{p}}_2 = -\nabla_2 U(\vec{r}_1 - \vec{r}_2) \quad (85)$$

Since

$$\nabla_n U(\vec{r}_1 - \vec{r}_2) = -\nabla_{r_2} U(\vec{r}_1 - \vec{r}_2), \quad (86)$$

then, as a consequence of (85,86), follows the law of total momentum conservation:

$$\frac{d}{dt}(\vec{p}_1 + \vec{p}_2) = 0; \quad \vec{p}_1 + \vec{p}_2 = \text{const.} \quad (87)$$

Thus, the distortion of the trajectory for a photon passing e.g. the Sun shows(demonstrates) the variation of its momentum; it follows from the law of the total momentum conservation that the momentum of the Sun changes by the same amount. We can make an obvious conclusion: if a photon is attracted to a massive body, then the massive body is attracted to the photon to the same extent. Therefore, photons, like any other particles, participate in the gravitational interaction, interaction intensity being proportional to the proper intrinsic energy of the particle:  $\varepsilon = \hbar\omega = p$ .

The azimuth velocity of stars in galaxies is about 100-200 km/sec. That is why, the dark matter elements belonging to a certain galaxy at first sight may seem to have the same velocities. Hence, all relativistic particles, such as photons, neutrino, and cosmic rays, are beyond our consideration; as a result, practically none of the observed particles can create an additional gravitational field. In this connection an idea arises that there are heavy cold particles contributing only to the gravitational interaction; they are called dark matter.

However, a possible alternative point of view exists. First, we examine a simple example. A charged ion of a hydrogen atom creates a Coulomb potential where localized states for an electron are formed. Filling up one of the localized states makes the hydrogen atom electrically neutral, as the nuclear field is completely screened by an electron. On the other hand, if we insert a proton into a metal where there is a sea of free electrons, the localized state does not occur, but this time the nuclear field is screened by free electrons. The trajectory of each electron is distorted near the nucleus so much, that, as a result, electron density increases exactly to the same extent and it screens the nuclear field completely. A positive charge interacts with all free electrons of metal in a Coulomb way and attracts them.

Any heavy body attracts all free particles of a cosmic space by the gravitational interaction in a Coulomb way as well. Nevertheless, there is a significant difference between these two processes. Free electrons of metal are attracted to a positive charge, begin repulsive from each other, as a consequence, the electrical field of the positive charge is screened by electrons. The situation is quite opposite with the gravitational interaction. A massive body attracts particles from the surrounding space. Due to this attraction the total gravitational potential increases, thereby increasing the particle attraction even

more. A positive feedback or antiscreening arises that can lead to the system instability. As an illustration, we examine the both situations: screening of an electrical field by free electrons in metal and antiscreening of a gravitational field by free particles (any) in cosmic space.

An external charge with harmonics  $\rho_{ext}(k)$  placed into a metal creates a real charge  $\rho_i(k)$  defined as a sum of external and induced charges:

$$\rho_i(k) = \rho_{ext}(k) + \rho_{res}(k) \quad (88)$$

We can express the induced charge through the polarizability of electrons in metal  $\rho_{res}(k) = -\chi(k)\rho_i(k)$ .

Here  $\chi(k) = k_{TF}^2/k^2$ ;  $k_{TF}$  is a characteristic wave vector calculated using a Thomas – Fermi approximation [8]. As a result, we obtain

$$\rho_i(k) = \frac{\rho_{ext}(k)}{1 + \chi(k)} = \frac{k^2}{k_{TF}^2 + k^2} \rho_{ext}(k); \quad (89)$$

$$k_{TF}^2 = \frac{4k_F}{\pi a_B},$$

Here  $k_F$  is a Fermi momentum in metal. It follows from (89) that a Coulomb potential of a point charge  $q$ , for example, is transformed into a screened potential:

$$\Phi_{ext} = \frac{q}{r}; \quad \Phi_i = \frac{q}{r} \exp(-k_{TF}r).$$

Now we consider a situation rather close to the gravitational interaction. Suppose, the entire space is filled up with neutral particles that have some homogeneous density  $\rho_0$  and interact according to the law of gravitation. If any density fluctuation  $\rho_{ext}(k)$  occurs in the space, then, owing to the gravitational interaction, all other particles begin to adjust to this density; there-after we can re-write the real density in the form:

$$\rho_i(k) = \rho_{ext}(k) + \rho_{res}(k) = \rho_{ext}(k) + \chi_\gamma(k)\rho_i(k) \quad (90)$$

On the analogy of a free electrons susceptibility, we imagine a gravitational susceptibility  $\chi_\gamma(k)$  like this:  $\chi_\gamma = k_0^2/k^2$ . Here  $k_0$  depends on the value of  $\rho_0$  and on the distribution function of the particle velocity. Afterwards, the real density acquires the form:

$$\rho_i(k) = \frac{k^2}{k^2 - k_0^2} \rho_{ext}(k)$$

This causes gravitational instability of the system relative to the long-wave density fluctuations. As fluctuations develop, slow particles, which compose a small part of an average density, are pulled out of the surrounding space and transformed into clusters of matter in form of stars and galaxies. Fast relativistic particles remain free and continue to participate in creating an additional grav-

itational field. We denote clusters of a cool matter in form of stars and galaxies having finite motion as  $\rho_{cold}(k)$ . The remainder relativistic particles in form of cosmic rays, photons and neutrino create additional non-homogeneous matter density due to the trajectory distortion  $\rho_{rel}(k) = \chi_{rel}(k)\rho_i(k)$ . Here  $\chi_{rel}(k)$  is the gravitational polarizability of the relativistic particles. Thus, the total density is equal to

$$\rho_i(k) = \frac{\rho_{cold}(k)}{1 - \chi_{rel}(k)}.$$

Being on Earth, we have no possibility to scan the distribution of a total energy over the entire space. However, judging from the fact that the azimuth velocity of stars moving away from the centre of galaxy remains nearly constant, the total gravitational potential must have the form:

$$\Phi_i(r) = \eta \ln\left(\frac{r}{R_c}\right),$$

Here  $\eta$  is a dimensionless parameter,  $R_c$ — a gravitational size of a space belonging to a certain galaxy. Provided that the centrifugal and centripetal forces are equal

$$r\dot{\phi}^2 = \frac{\partial\Phi_i(r)}{\partial r} = \frac{\eta}{r}$$

we come to the expression for the circular velocity:

$$v = r\dot{\phi} = \sqrt{\eta}.$$

At the star velocity being approximately equal to 200 km/sec we obtain the value  $\eta = 8 \cdot 10^{-7}$ . From the expression for the potential and with the aid of the Poisson equation we obtain the space distribution density of matter:

$$\Delta\Phi = \frac{\eta}{r^2} = \frac{4\pi\gamma}{c^2}\rho_i(r);$$

$$\rho_i(r) = \frac{c^2}{4\pi\gamma} \frac{\eta}{r^2}.$$

The space integral of density provides a value of mass inside a sphere of radius  $R$ :

$$M_i = \frac{\eta c^2 R}{\gamma} = \frac{v^2 R}{\gamma}.$$

For our Galaxy having the size of about  $R = 5 \cdot 10^4$  light years and velocity of  $v = 200$  km/sec we obtain  $M_i = 10^{45}$  gr. Mass of cool matter is estimated by value  $M_{cold} = 4 \cdot 10^{44}$  gr, therefore, mass of a relativistic matter is comparable with that of the cool one  $M_{rel} \approx M_{cold}$ . Thus, as a result of the trajectory distortion for relativistic particles, an additional nonhomogeneous distribution of rela-

tivistic matter occurs and, consequently, an additional gravitational potential as well. That is why, there is no need to search for a mystical dark matter; relativistic energy is quite sufficient to create an additional gravitational field. Moreover, emission of radiation by stars and galaxies as well as supernova outburst lead to the constant growth of relativistic energy in space. So, observations of the azimuth stellar motion both in galaxies and galaxies in clusters point to the existence of an additional gravitational field. Since azimuth and radial motion follows from the general equation of motion, for example in form (63), the radial motion is submitted to the same additional gravitational attraction; for this reason, there is no dark energy to create antigravitation [9,10]. Thus, if red shift is related to recession of galaxies, then a contradiction arises, because galaxies have to scatter with acceleration but, judging from the azimuth motion, this is impossible.

It is more natural to consider atomic spectra of far stellar radiation to be time dependent as a consequence of time dependence of physical vacuum parameters. Since atomic levels are proportional to Bohr energy, and Bohr energy, in turn, is proportional to the rest energy of electron ( $\varepsilon_B = \alpha^2 \varepsilon_{0e}$ ) we can affirm that the electron mass increases with time; this means that vacuum parameters for the electron oscillation branch  $\tau_e(t)$  and  $\xi_e(t)$  decrease with time. The Hubble constant can be defined from the following expression:

$$\begin{aligned} H(t) &= \frac{d}{dt} \left( \frac{m_{e0}(t)}{m_{e0}(t=0)} \right) \\ &= \frac{d}{dt} \left( \frac{\tau_e(t=0)}{\tau_e(t)} \right) \\ &= \frac{d}{dt} \left( \frac{\omega_{0e}(t)}{\omega_{0e}(t=0)} \right). \end{aligned} \quad (91)$$

The red shift indicates that the Hubble constant is a monotonically growing time function and at the present moment it equals to  $2.5 \cdot 10^{-18} \text{ cek}^{-2}$ .

Nowadays the Universe is in a metastable state, energy emission transitions occurring in two opposite directions. On one hand, nucleosynthesis of light nuclei—takes place, which is the source of stellar energy. On the other hand, nuclear disintegration of heavy nuclei (natural radioactivity) – occurs, as well with energy emission. From today's point of view, nuclear fusion looks quite natural as there is a binding energy between nuclei; moreover, the binding energy on one nucleus increases with the growth of atomic number up to iron. Creation of heavier elements turns out to be less gainful; in this connection it is a surprise that heavy elements, up to uranium, exist on

Earth. Nuclei of uranium are in metastable state. If we launched a piece of uranium towards the Sun, the uranium nuclei, under neutron bombardment, would decompose into lighter fragments. This means that uranium cannot occur on Sun. Deposits of uranium on Earth, however, prove that the Earth is an earlier formation than the Sun. Chemical composition of the Earth principally differs from that of the Sun. Sun consists of 75% hydrogen, 24% helium and a negligibly small amount of heavier elements, whereas Earth consists of 32% iron, 30% oxygen and a noticeable amount of heavier elements up to uranium. Heavy elements existing on Earth, as well as the red shift, point out to nonstationarity of physical vacuum parameters. Heavy elements could only occur on Earth when they were energetically gainful; variations of physical vacuum parameters led to the transition of heavy nuclei into a metastable state. A further evidence of nonstationarity of physical vacuum parameters is that not only stars, but also planets emit energy; moreover, volcanic activity, similar to that on the Earth, is still being observed on Jupiter satellites. It is known that the Jupiter emits twice as much energy as it receives from the Sun. We can express the Jupiter energy emission via the Hubble constant. From the law of conservation of energy it follows:

$$\frac{d}{dt}(M_J c^2) + L_J = 0. \quad (92)$$

Here  $M_J c^2$  is Jupiter energy of  $1.8 \cdot 10^{31}$  erg, and  $L_J$  is the integral emission flux of  $6.5 \cdot 10^{25}$  erg/sec. By dividing both parts of (92) into Jupiter energy, and considering that the Jupiter only consists of hydrogen, we can reduce (92) to form

$$\frac{d \varepsilon_{0e}/dt + d \varepsilon_{0n}/dt}{\varepsilon_{0e} + \varepsilon_{0n}} + l_J = 0. \quad (93)$$

Here  $l_J$  is specific luminosity of the Jupiter equal to  $3.6 \cdot 10^{-26} s \sigma^{-1}$ . Taking into consideration the definition of the Hubble constant (91), we can rewrite Equation (93) as follows:

$$\frac{d \varepsilon_{0n}/dt}{\varepsilon_{0n}} = -\frac{\varepsilon_{0e}}{\varepsilon_{0n}} H(t) - l_J, \quad (94)$$

All values at the right part of (94) are known, therefore,

$$\frac{d \varepsilon_{0n}}{dt} \approx -\frac{d \varepsilon_{0e}}{dt}.$$

So, the red shift shows that the rest energy of the electron is growing with time, whereas emission of radiation by planets indicates that the rest energy of the proton is decreasing; the total change of the energy for the electron and proton is so great, that it leads to planet heating and emission of radiation.

Since physical vacuum has existed eternally, the values, which characterize the vacuum, can only be of two types: either time independent constants, or oscillating functions. The fundamental values are general for both electron and nuclear modes  $g, \alpha, c = \xi_e/\tau_e = \xi_n/\tau_n$  seem to be thought as constant values; however, we have to consider as time dependent the values, which are characteristic either for an electron mode only by  $\xi_e, \tau_e$ , or for a nuclear one—by  $\xi_n, \tau_n$ . At the present moment electron and nuclear frequencies are moving towards each other.

Finally, we pay attention to one more mechanism of a gravitational instability. Not coincidentally, there has been some cause for concern so far, that microscopic black holes are possible to occur under the experimental research with Large Hadron Collider in CERN. The thing is that the gravitational attraction between particles grows with increasing particle energy, whereas, the electrical repulsion remains constant due to the law of conservation of charge. In this connection we examine two protons which are speeded up to a certain energy in an accelerator. We write down the Hamiltonian for two protons, taking into account an electrical and gravitational interaction:

$$H = \varepsilon_1 + \varepsilon_2 + \frac{e^2}{|\vec{r}_1 - \vec{r}_2|} - \frac{\gamma m_1 m_2}{|\vec{r}_1 - \vec{r}_2|}.$$

Since masses of the particles are proportional to their energy  $m_1 = \varepsilon_1/c^2$ ,  $m_2 = \varepsilon_2/c^2$ , then, under the following condition

$$\frac{\gamma \varepsilon_1 \varepsilon_2}{c^4} > e^2$$

the gravitational attraction turns out to exceed the electrical repulsion. Consequently, the gravitational collapse may occur when the particle energy amounts to

$$\varepsilon > \varepsilon_c = \frac{ec^2}{\sqrt{\gamma}} = 10^{27} \text{ eV}.$$

Maximum particle energy in cosmic rays reaches  $10^{21}$  eV. The value of energy expected at the accelerator in CERN is  $7 \cdot 10^{15}$  eV that is eleven orders less than the critical value. That is why the microscopic black holes are impossible to appear in the accelerator. From the expression for the critical energy, we can define the specific wave vector and the corresponding de Broglie wave length:

$$\varepsilon_c = \hbar k_c = \frac{c \hbar}{\lambda_c} = \frac{ec^2}{\gamma^{1/2}}$$

It follows:

$$\lambda_c = \frac{e \sqrt{\gamma}}{\alpha c^2} = \sqrt{\frac{\gamma \hbar}{\alpha c^3}} = 1.88 \cdot 10^{-32} \text{ cm}$$

Planck introduced the specific length by reason of dimension:

$$r_{pl} = \sqrt{\frac{r\hbar}{c^3}}.$$

It is easy to see that the specific length  $\lambda_c$  can be expressed via Planck length as follows:

$$\lambda_c = \frac{r_{pl}}{\sqrt{\alpha}}$$

Thus, the considerations above allow attaching a physical sense to the Planck length, which defines the most probable value for the lattice constant of physical vacuum; here  $k_c$  specifies the edge of the Brillouin zone in  $k$ -space, and  $\varepsilon_c$  – the width of the allowed energy region.

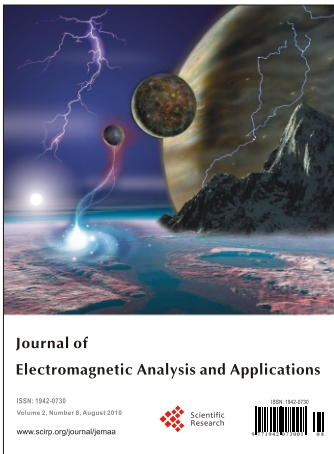
## 5. Conclusions

In presented paper we try to consider problems of the gravitational optics and dark matter developing from the crystal model for the vacuum. Thus, our model for vacuum is represented as a material medium in which dynamical properties of the crystal specify the spectrum of elementary particles. How it is follows from consideration it enables to describe both electromagnetic waves and spectrum of elementary particles from the unified point of view. We have obtained the combined equations for a multicomponent order parameter in the form of the electric and magnetic vacuum polarization, which defines the spectrum and symmetry of normal oscillations in the form of elementary particles. We have restored the fundamental parameters of physical vacuum, such as: a susceptibility for the electric and magnetic polarization (equal to the constant of fine structure), parameters of length and time for the electron and nuclear branches of the oscillations, correspondingly. We have shown that the charge quantization is directly connected to discreteness of vacuum consisting of particles with the interaction constant equal to the double charge of a Dirac monopole. Elementary particles are excitations of vacuum in a form of wave packets of a soliton type. We have obtained an exact equation of motion for a particle in a gravitational field. Energy defines both gravitational interaction and particle inertia, inertia being of an anisotropic value; that is why the statement, that the inertial and gravitational masses are equivalent, is not correct. We have examined the situation when galaxies are distributed over the entire infinite space according to the cosmological principle. In this case recession of galaxies is impossible; therefore,

the red shift of radiation emitted by far galaxies must be interpreted as the blue time shift of atomic spectra. As a consequence, it follows that both rest energy and mass of electron are increasing now. Since physical vacuum exists eternally, vacuum parameters can be either constant or oscillating with time. These are time oscillations of  $\xi_e(t), \xi_n(t)$  and  $\tau_e(t), \tau_n(t)$  which have caused electron mass growth within recent 15 milliard years, inducing red shift; on the contrary, proton mass decreases, responsible for emission of radiation by planets.

## REFERENCES

- [1] F. Zwicky, "Die Rotverschiebung von extragalaktischen Nebeln," *Helvetica Physica Acta*, Vol. 6, 1933, pp. 110-127.
- [2] K. C. Freeman, "On the Disk of Spiral and So Galaxies," *Astrophysical Journal*, Vol. 160, 1970, pp. 811-830.
- [3] J. A. Tyson, F. Valdes, J. F. Jarvis, and A. P. Mills, Jr., "Galaxy Mass Distribution from Gravitational Light Deflection," *Astrophysical Journal*, Vol. 281, 1984, pp. L59-L62.
- [4] A. G. Riess, A. V. Filippenko, P. Challis, A. Clocchiatti, A. Diercks, P. M. Garnavich, R. L. Gilliland, C. J. Hogan, J. Saurabh, R. P. Kirshner, B. Leibundgut, M. M. Phillips, D. Reiss, B. P. Schmidt, R. A. Schommer, R. C. Smith, J. Spyromilio, C. Stubbs, N. B. Suntzeff and J. Tonry, "Observational Evidence from Supernovae for an Accelerating Universe and a Cosmological Constant," *Astrophysical Journal*, Vol. 116, No. 3, 1998, pp. 1009-1038.
- [5] S. Perlmutter, G. Aldering, G. Goldhaber, R. A. Knop, P. Nugent, P. G. Castro, S. Deustua, S. Fabro, A. Goobar, Groom, I. M. Hook, A. G. Kim, M. Y. Kim, J. D. E. C. Lee, N. J. Nunes, R. Pain, C. R. Pennypacker and R. Quimby, "Measurements of  $\{\Omega\}$  and  $\{\Lambda\}$  from 42 High-Redshift Supernovae," *Astrophysical Journal*, Vol. 517, No. 2, 1999, pp. 565-586.
- [6] E. Q. Milne, "A Newtonian Expanding Universe," *Quarterly Journal of Mathematics*, Vol. 5, No. 1, 1934, pp. 64-72.
- [7] P. A. M. Dirac, "Quantised Singularities in the Electromagnetic Field," *Proceedings of the Royal Society of London A*, Vol. 133, No. 821, 1931, pp. 60-72.
- [8] D. Pines, "Elementary Excitations in Solid," W.A. Benjamin, New-York, 1963.
- [9] A. D. Chernin, "Dark Energy And Universal Antigravitation," *Physics-Uspekhi*, Vol. 51, No. 3, 2008, pp. 253-282.
- [10] V. N. Lukash and V. A. Rubakov, "Dark Energy: Myths and Reality," *Physics-Uspekhi*, Vol. 51, 2008, pp. 283-290.



# Journal of Electromagnetic Analysis and Applications

ISSN: 1942-0730 (Print), 1942-0749 (Online)  
[www.scirp.org/journal/jemaa](http://www.scirp.org/journal/jemaa)

Journal of Electromagnetic Analysis and Applications (JEMAA) is a professional journal in the field of electromagnetic analysis, testing and application. The goal of this journal is to provide an international platform for engineers and academicians all over the world to promote, share, and discuss various new issues and developments in the field of electromagnetic. This journal is edited to encourage deeper understanding and greater effectiveness in theory analysis, testing, numerical calculation and engineering application that relevant electromagnetic fields.

## Editors-in-Chief

Prof. James L. Drewniak  
Prof. Yuanzhang Sun

Electrical Engineering and Materials Science and Engineering, Missouri-Rolla, USA  
School of Electrical Engineering, Wuhan University, China

## Subject Coverage

JEMAA publishes four categories of original technical reports: papers, communications, reviews, and discussions. Papers are well-documented final reports of research projects. Communications are shorter and contain noteworthy items of technical interest or ideas required rapid publication. Reviews are synoptic papers on a subject of general interest, with ample literature references, and written for readers with widely varying background. Discussions on published reports, with author rebuttals, form the fourth category of JEMAA publications. Topics of interest include, but are not limited to:

- Electromagnetic Numerical Analysis
- Multiphysics Coupled Problems
- Electromagnetic Inverse Problems
- Electromagnetic Structure Optimization
- Test Electromagnetic Analysis Method
- Workshop Benchmark Problems
- Electromagnetic Devices
- Electromagnetic Compatibility
- Electromagnetic Nondestructive Testing
- Electromagnetic Material Modelling

## Notes for Intending Authors

Submitted papers should not be previously published nor be currently under consideration for publication elsewhere. Paper submission will be handled electronically through the website. All papers will be peer reviewed. For more details about the submissions, please access the website.

## Website and E-Mail

<http://www.scirp.org/journal/jemaa>

[jemaa@scirp.org](mailto:jemaa@scirp.org)

## TABLE OF CONTENTS

**Volume 2 Number 8**

**August 2010**

**A New Formulation of Electrodynamics**

A. I. Arbab, F. A. Yassein..... 457

**A Preliminary Ray Tracing Approach to Computational Electromagnetics for Reverberation Chambers**

F. Nauwelaerts, D. V. Troyen, G. A. E. Vandenbosch..... 462

**Voltage Control in Smart Grids: An Approach Based on Sensitivity Theory**

M. Brenna, E. D. Berardinis, F. Foiadelli, G. Sapienza, D. Zaninelli..... 467

**Impact of Wind Farms of DFIG Type on Power System Transient Stability**

L. B. Shi, S. Q. Dai, L. Z. Yao, Y. X. Ni, M. Bazargan..... 475

**Induction of Oxidative Stress in Male Rats Subchronically Exposed to Electromagnetic Fields at Non-Thermal Intensities**

A. Achudume, B. Onibere, F. Aina, P. Tchokossa..... 482

**Focal Region Field of a Two Dimensional Gregorian System Coated with Isotropic Chiral Medium**

T. Rahim, J. Mughal, M. Hussnain..... 488

**New Consideration of Problems of Gravitational Optics and Dark Matter Based on Crystal Model of Vacuum**

E. V. Chensky..... 495